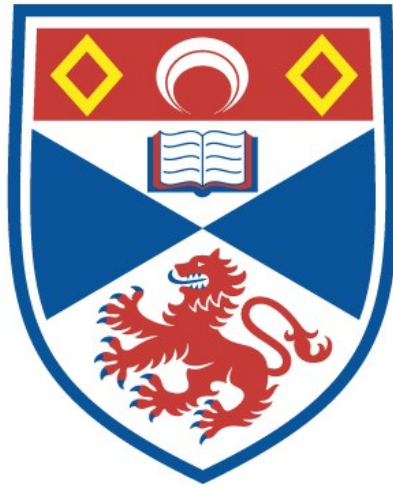


University of St Andrews



Full metadata for this thesis is available in
St Andrews Research Repository
at:

<http://research-repository.st-andrews.ac.uk/>

This thesis is protected by original copyright



Structures and ionic conductivity in crystalline polymer electrolytes

A Thesis presented for the degree of
Doctor of Philosophy
in the Faculty of Science of the University of St. Andrews
by Zlatka Stoeva, B.Sc.

September 2001

School of Chemistry
St. Andrews



TL
D995

DECLARATION

I, Zlatka Stoeva, hereby certify that this thesis, which is approximately 35,000 words in length, has been written by me, that it is the record of work carried out by me and that it has not been submitted in any previous application for a higher degree.

Date: 17/12/01

Signature of candidate:

I was admitted as a research student in September 1997 and as a candidate for the degree of Doctor of Philosophy in August 1998; the higher study for which this is a record was carried out in the University of St.Andrews between 1997 and 2001.

Date: 17/12/2001

Signature of candidate:

I hereby certify that the candidate has fulfilled the conditions of the Resolution and Regulations appropriate for the degree of Doctor of Philosophy in the University of St.Andrews and that the candidate is qualified to submit this thesis in application for that degree.

Date:

17/12/2001

Signature of supervisor

LIBRARY DECLARATION

In submitting this thesis to the University of St.Andrews I understand that I am giving permission for it to be made available for use in accordance with the regulations of the University Library for the time being in force, subject to any copyright vested in the work not being affected thereby. I also understand that the title and abstract will be published, and that a copy of the work may be made and supplied to any *bona fide* library or research worker.

Date: 17/12/2001

Signature of candidate:

To my Dad

ACKNOWLEDGEMENTS

I would like to thank my supervisor Prof.P.G.Bruce for his guidance, encouragement and support, and for the opportunity to work on this challenging and exciting project.

Thanks must go to the members of Prof.Bruce's group, and in particular to Dr.Y.Andreev for teaching me crystallography over the last few years.

Special thanks go to Dr.D.Tunstall for his help and patience with my first steps in NMR spectroscopy.

I would like to thank my friends in St.Andrews for giving me a hand through the dark days and for sharing my happiness through the good times.

I would like to thank my Mum and brother for their love, for putting up with me and for teaching me many valuable lessons in my life.

Many thanks go to my friends in Bulgaria who proved that there are no time and distance limits for the true friendship.

Very big Thanks go to my daughter for her love and support and especially for her criticism in moments of my laziness and for reminding me that I have to write up this thesis after all.

Finally I would like to acknowledge the financial support from CVCP and the University of St.Andrews.

ABSTRACT

The crystal structures and properties of stoichiometric polymer electrolytes of composition 6:1 (ether oxygens:cation) have been studied. The attention is focussed on the crystalline complexes $\text{PEO}_6\text{:LiXF}_6$ ($X = \text{P, As, Sb}$) and the amorphous complex $\text{PEO}_6\text{:LiSbF}_6$. Crystalline complexes of various molecular weights (ranging from 1,000 to 100,000) have been investigated. The variation of the molecular weight does not effect the crystal structures, however, the thermal and conducting properties show strong dependence on the molecular weight.

The crystal structures of the complexes $\text{PEO}_6\text{:LiXF}_6$ ($X = \text{P, Sb}$) have been studied using powder X-ray and neutron diffraction data. The structures of these complexes consist of double non-helical polymer chains which interlock to form cylindrical tunnels. The lithium ions are located within these tunnels and are not co-ordinated to the anions. In this aspect the 6:1 complexes are distinctive compared to other known stoichiometric complexes (e.g. 3:1 or 1:1 compositions). The 6:1 structure provides permanent pathways which may permit ion transport.

Conductivity studies demonstrate that the crystalline 6:1 phases may exhibit higher ionic conductivity than the analogous amorphous systems above their glass transition temperature. Highest conductivities are observed in the highly crystalline, low molecular weight polymer electrolytes. At room temperature, these materials reach ionic conductivity about one order of magnitude higher than the analogous amorphous phase. However, high molecular weight crystalline electrolytes of reduced crystallite dimensions show inferior conducting properties.

NMR linewidth and spin-lattice relaxation time studies indicate that ionic conductivity in the highly conducting crystalline complexes is dominated by lithium ion motion. The anions are not involved in long range translational motion. The combination of NMR and conductivity results suggests that the cation transport number equals 1 ($t_+ = 1$). In contrast, both ions are found to be mobile in the amorphous complex $\text{PEO}_6\text{:LiSbF}_6$.

The exact mechanism of ion conduction in the crystalline 6:1 polymer electrolytes is not known but it probably involves lithium ion hopping between neighbouring lattice sites within the one dimensional tunnels in the structure.

CONTENTS

Chapter 1

Introduction

1.1 Aims of the present work	1
1.2 Main problems and directions in the area of polymer electrolytes	3
1.3 Mechanism of ionic conduction in polymer electrolytes: present theories and models	5
1.4 Advances in the structural studies of polymer electrolytes	8
1.5 References	10

Chapter 2

Methods for preparation

2.1. General considerations	13
<i>Solvent casting</i>	14
<i>Hot pressing</i>	14
<i>Preparation in capillaries</i>	15
<i>Preparation of powder samples</i>	15
2.2. Results and discussion	16
2.2.1. $\text{PEO}_6\text{:LiPF}_6$	17
2.2.2. $\text{PEO}_n\text{:LiAsF}_6$ complexes	18
2.2.3. $\text{PEO}_n\text{:LiSbF}_6$ complexes	20
<i>Stoichiometric crystalline complexes</i>	20
<i>Amorphous complex $\text{PEO}_6\text{:LiSbF}_6$</i>	22
2.2.4. Influence of the molecular weight of the polymer	23
2.3. Conclusions	25
2.4. References	25

Chapter 3

Thermal properties

3.1. Differential Scanning Calorimetry (DSC)	26
3.1.1. General considerations	26
3.1.2. Experimental results and discussion	27
$PEO_6:LiPF_6$	28
$PEO_6:LiAsF_6$	30
$PEO_6:LiSbF_6$ (crystalline complex)	32
$PEO_6:LiSbF_6$ (amorphous complex)	34
3.2. Variable-temperature XRD diffraction	34
3.2.1. Results and discussion	35
$PEO_6:LiAsF_6$	35
$PEO_6:LiSbF_6$ complexes	36
3.3. Conclusions	38
3.4. References	39

Chapter 4

Crystal structure studies

4.1. Structure refinement with powder diffraction data	41
4.1.1. Theoretical background	41
4.1.1a. The basis of the Rietveld refinement	42
4.1.1b. Restraints and constraints in the Rietveld refinement	45
4.1.1c. Structural studies using neutron time-of-flight data	46
<i>The complimentary relationship between X-ray and neutron data</i>	46
<i>Time-of-flight neutron diffraction techniques</i>	47
4.1.2. Results and discussion	48
4.1.2a. Experimental details	48
4.1.2b. Structure refinement of $PEO_6:LiPF_6$ and $PEO_6:LiSbF_6$ using neutron time-of-flight data	49
<i>Rietveld refinement</i>	49
<i>Discussion of the crystal structures</i>	53

4.2. Powder X-ray diffraction applied for studies of the physical properties (particle sizes) of the crystalline complexes	56
4.2.1. Effect of crystal size on the powder pattern – particle size measurements	56
4.2.2. Estimation of crystallite size – experimental results	58
4.3. Conclusions	61
4.4. References	62

Chapter 5

Conductivity studies

5.1. General considerations	64
5.2. Alternating current measurements with blocking electrodes	66
5.2.1. Experimental details	67
5.2.2. Analysis of complex impedance plots and equivalent circuits	68
5.2.3. Analysis of conductivity data	73
5.2.3a. Temperature dependence of total ionic conductivity	73
5.2.3b. Ionic conductivity and its relation to the degree of crystallinity and molecular weight	79
5.3. Conductivity studies using non-blocking electrodes	81
5.3.1. A.c. measurements with non-blocking electrodes	81
<i>Experimental details</i>	82
<i>Results and discussion</i>	82
5.3.2. Direct current measurements	86
<i>Crystalline PEG₆:LiSbF₆</i>	87
<i>Amorphous PEO₆:LiSbF₆</i>	90
5.4. Conclusions	91
5.5. References	92

Chapter 6

NMR studies

6.1. Theoretical background	94
6.1.1. Magnetic interactions in the solid state	94
<i>Zeeman interactions</i>	95
<i>Dipolar interactions</i>	96

<i>Chemical shift interactions</i>	96
<i>Spin-spin coupling interactions</i>	97
<i>Quadrupolar interactions</i>	97
6.1.2. Techniques for line narrowing in solids	98
<i>Magic angle spinning</i>	98
<i>Dipolar decoupling</i>	99
<i>Other techniques</i>	99
6.1.3. Free induction decay measurements	100
6.1.4. Relaxation times	101
<i>Spin-spin relaxation time</i>	101
<i>Spin-lattice relaxation time</i>	101
<i>Spin-lattice relaxation time in the rotating frame</i>	102
6.1.5. The application of solid state NMR for study of ionic motions	102
6.1.6. Quadrupole effects in the solid state and relevant NMR techniques	106
6.2. ^7Li NMR studies	109
6.2.1. Experimental details	109
6.2.2. ^7Li NMR studies of crystalline 6:1 complexes	111
6.2.2a. General considerations	111
6.2.2b. ^7Li studies of crystalline 6:1 complexes of $M_w = 1,000$	112
<i>Analysis of line shape and its temperature dependence</i>	112
<i>Contributions to the ^7Li linewidth (MAS and proton decoupling experiments)</i>	115
<i>Spin-lattice relaxation time (T_1) measurements</i>	118
<i>Model for Li ion motion based on the NMR data</i>	123
6.2.3. ^7Li studies of the amorphous complex $\text{PEO}_6:\text{LiSbF}_6$	124
<i>Analysis of line shape and its temperature dependence</i>	124
<i>Contributions to the ^7Li line</i>	126
<i>Spin-lattice relaxation time (T_1) measurements</i>	128
6.2.4. Conclusions from the ^7Li NMR studies	130
6.3. NMR studies of the anion structure and dynamics	133
6.3.1. Experimental considerations	133
^{75}As and ^{121}Sb NMR	133
^{31}P NMR	135

6.3.2. ^{31}P studies of the crystalline complex $\text{PEG}_6\cdot\text{LiPF}_6$	136
<i>Variable temperature linewidth measurements with static samples</i>	136
<i>High-resolution MAS and proton decoupling experiments</i>	136
<i>Spin-lattice relaxation time measurements</i>	138
6.3.3. ^{75}As and ^{121}Sb studies of crystalline 6:1 complexes	138
<i>Temperature dependence of the linewidth</i>	138
<i>Spin-lattice relaxation time measurements</i>	142
6.3.4. ^{121}Sb studies of the amorphous complex $\text{PEO}_6\cdot\text{LiSbF}_6$	142
<i>Analysis of lineshape and its temperature dependence</i>	142
<i>Spin-lattice relaxation time measurements</i>	144
6.3.5. Conclusions from the NMR studies of the anion structure and dynamics	145
6.4. NMR studies of chain mobility	147
6.4.1. ^1H and ^{13}C NMR as a probe of the polymer structure and dynamics in polymer electrolytes	147
6.4.2. Results and discussion	147
<i>General considerations</i>	147
<i>^1H linewidth studies of the amorphous complex $\text{PEO}_6\cdot\text{LiSbF}_6$</i>	149
6.5. References	151

Chapter 7

Conclusions: mechanism of ionic conduction in stoichiometric polymer electrolytes

7.1. Summary of the experimental evidence for ion transport in stoichiometric polymer electrolytes	154
<i>Levels of ionic conductivity</i>	155
<i>Transport numbers</i>	157
7.2. Ion transport in the crystalline complexes of composition 6:1	158
7.3 Further work and optimising the ionic conductivity	160
7.4. References	160

Appendix I	162
Appendix II	167
Appendix III	169
Appendix IV	171

ABBREVIATIONS

PEO	polyethylene oxide ($M_w = 100,000$)
PEG	polyethylene glycol dimethyl ether ($M_w = 1,000$ and $2,000$)
M_w	weight averaged molecular mass
M_n	number averaged molecular mass
XRD	X-ray diffraction
VT – XRD	Variable – temperature X-ray diffraction
DSC	differential scanning calorimetry
T_g	glass transition temperature
TOF	time-of-flight (neutron diffraction data)
MAS	Magic angle spinning

CHAPTER 1

INTRODUCTION

1.1. Aims of the present work

Solid polymer electrolytes consist of a salt dissolved in coordinating high-molecular weight polymers. They can exhibit ionic conductivities approaching those of many liquid electrolytes. The combination of solid but flexible material with high conductivity makes these electrolytes attractive for use in all-solid-state electrochemical devices such as lithium batteries, electrochromic displays, smart windows, etc.

Polyethylene oxide (PEO) $-\text{[CH}_2\text{-CH}_2\text{-O]}_n-$ is the most studied solvating polymer. PEO based electrolytes may form both crystalline and amorphous phases. Crystalline complexes can be obtained at certain discrete compositions. Amorphous phases are formed over a wide range of compositions and temperatures, in some cases, the compositions at which crystalline phases also exist.

A great deal has been accomplished both experimentally and conceptually since the discovery of these materials. Most of the studies concentrated on the amorphous or dilute polymer electrolyte systems since they were found to support high ionic conductivity [1, 2, 3, 4, 5, 6]. The crystalline polymer – salt complexes received much less attention mainly because they were not considered to exhibit ionic conductivity. Major advances have been made in establishing the structures of these crystalline polymer electrolytes [7, 8]. This was not matched however by adequate studies of the properties of these materials and a number of important issues involving the dynamics and conductivity behaviour of these systems have yet to receive experimental and theoretical consideration.

The purpose of the present work is to carry out a study of the properties of the stoichiometric crystalline polymer – salt complexes and to establish how these properties are related to the crystal structures. The attention is focussed on the crystalline stoichiometric complexes $\text{PEO}_6:\text{LiXF}_6$ ($X = \text{P, As, Sb}$) for several reasons. First, the crystal structures of these complexes are radically different from the previously known structures of 4:1, 3:1 or 1:1 crystalline complexes [7, 8]. The structure of the complexes 6:1 suggests that Li ion transport is possible along one-dimensional tunnels formed by the polymer chains. In addition, the salts LiXF_6 ($X = \text{P, As}$) are widely used electrolyte salts in lithium batteries and therefore the study of their complexes may lead to new technological developments. Third, it was found in the course of the present work that amorphous complexes of the same composition (6:1) could be obtained. Therefore the properties of crystalline and amorphous phases of the same composition could be directly compared.

Variety of techniques and methods have been employed and the results are discussed in the separate chapters of this work. The overall results are presented in Chapter 7, with some suggestions for the mechanism of ionic conduction found in these materials.

The present introductory chapter reviews briefly the current problems in the area of polymer electrolytes. The present theories and models for ionic conduction, and the structural studies are discussed. The survey suggests the necessity for new experimental and theoretical approaches in the search for novel technologically important materials.

1.2. Main problems and directions in the area of polymer electrolytes

After the discovery of ionic conductivity in alkali metal salt complexes of PEO [9], polymer electrolytes have been proposed for batteries since they combine the advantages of solid state materials with the ease of processing inherent to polymers. In particular, lithium based batteries have high energy densities (of the order of 480Wh kg^{-1}) and this makes them attractive for industrial development. The high energy density of the lithium battery is mainly due to the following properties: first, lithium is the lightest element that can safely be handled in electrochemical processes and second, it exhibits the highest oxidation potential of any element.

Lithium batteries based on solid polymer electrolyte technologies have been proposed for a variety of applications such as electric vehicle, start-light-ignition and portable electronic and personal communications [2, 10, 11, 12]. Although each application has very specific sets of performance requirements, there are performance parameters that are common to all lithium polymer electrolyte battery technologies and these are:

- high cationic mobility
- wide electrochemical stability window
- improved safety.

The mobility of the cations in polymer electrolytes is a crucial factor for the operation of the electrochemical devices. Low cationic transference numbers, particularly in combination with low overall electrolyte conductivity, can adversely affect cell performance.

The transference numbers for lithium-based polymer electrolytes range from 0.06 to 0.3 [12] and this shows that the lithium ions are the minority charge carriers.

Despite the low cationic mobility, polymer electrolytes offer some advantages over the liquid systems in terms of electrochemical stability and safety, and interfacial properties.

Most of the research and development in the polymer electrolyte area have been focussed on improvement of the ambient temperature conductivity. The improvements were mainly achieved by the addition of large quantities of liquid plasticisers to a host polymer leading to the formation of gel-polymer electrolyte systems. In this class of electrolytes, the ionic conductivity is due to the mobility of the ionic species in the liquid phase. The plasticised polymer electrolytes exhibit higher ionic mobility and higher concentration of charge carriers thus allowing higher energy density. However, the electrochemical stability of the plasticised polymers is insufficient and their mechanical properties are inferior when compared with pure polymer electrolyte systems.

The other major direction for improving the conducting properties of polymer electrolytes is the design and preparation of highly amorphous materials with low T_g . This trend is based on the principle that ion transport in polymer electrolytes is closely related to the polymer segmental motion which is prominent above T_g and becomes more rapid as the temperature is raised. Therefore, host polymers with low softening temperatures were designed, with the aim to achieve high ionic conductivities at ambient temperatures. Despite efforts in this area, however, the maximum conductivity of amorphous polymer electrolytes remains around $10^{-4} \text{ S cm}^{-1}$ at room temperature.

It has been demonstrated recently that the levels of ionic conductivity may be enhanced by aligning, or organising the polymer chains. More organised materials can be achieved by forming liquid crystalline polymer electrolytes [13]. It has been shown that the conductivities of these electrolytes at 40°C are $\frac{1}{2}$ order of magnitude higher than can be obtained from the PEO:LiN(SO₂CF₃)₂ system.

Another approach for the preparation of organised polymer systems is stretching the polymer. It has been demonstrated [14] that the ionic conductivity in PEO:LiI can be enhanced on stretching the polymer. Such stretching is found to align the chains resulting in an increase in conductivity exceeding $\frac{1}{2}$ order of magnitude in the direction of stretch.

It is clear from the above discussion that no polymer electrolyte system has been found as yet, which provides high ionic conductivity ($>10^{-3} \text{ S cm}^{-1}$), lithium transference number >0.9 and good mechanical properties at ambient temperature. Other issues such as electrochemical stability vs. high voltage cathode materials and lithium anodes, and manufacturability have yet to be demonstrated.

1.3. Mechanism of ionic conduction in polymer electrolytes:

present theories and models

The earliest suggestions for describing the ionic transport in these materials were based on hopping models taken from crystalline solid electrolytes. Armand first suggested [3] that the metal ions move *via* a hopping motion in the structurally fixed pathway of the PEO helix. It was experimentally demonstrated later that these models were incorrect, and that ion conduction occurs in the amorphous phase above T_g . In the amorphous polymer electrolytes, ions move in dynamic environment in contrast to the crystalline ion conductors. However, polymer electrolytes are also different from liquid electrolytes since conduction in polymer electrolytes is not dependent on the macroviscosity but instead on the microviscosity of the polymer.

The theoretical models based on the Vogel-Tamman-Fulcher (VTF) and William-Lander-Ferry (WLF) [15] relations, or upon the free-volume [16] or configurational entropy models [17, 18] can describe the temperature dependence of several of the transport properties (conductivity, viscosity, diffusivity) quite well over a broad temperature range. Since these models are static macroscopic treatments, the mechanistic details, actual rates and mechanism of transport are not easily deduced. All of these models are based on thermodynamic arguments and they do not deal effectively with frequency – dependent measurements such as spectroscopy or dielectric relaxation.

The dynamic bond percolation theory (*dbpt*) [5, 19] is the only microscopic, kinetic description of polymer electrolytes. It has some definite strengths, such as:

- useful distinction between ionic motion and polymer motion
- straightforward comparison with the quasithermodynamic theories
- kinetic approach which allows computation of frequency-dependent properties
- parameterisation in terms of small number of parameters
- direct connection with the very well explored field of static percolation theory, etc.

On the other hand, there are several drawbacks which include the use of a lattice model to describe an amorphous elastomer, use of a hopping model for the anions (for which the hopping model assumption that the time between jumps far exceeds the time to execute one jump might not be correct), and finally, there is no sufficient information on precisely how to correlate the parameters in this model to the properties of the specific system under study.

It is true for all of the above models that the discussion of the transport properties and mechanism is concentrated on the homogeneous elastomeric phase only, and not on the partially crystalline materials. The only exception is the *dbpt* model which assumes that the

conductance in the crystalline regions may be neglected and then their effect on the conductivity appears in the following three ways:

- the crystalline regions will block conduction, so that a static percolation problem (conducting amorphous regions plus insulating crystalline ones) must be solved;

- the crystalline regions will anchor one end of the polymer chains protruding into the amorphous region. Thus the chain mobility is reduced and the renewal rate is decreased. As a result, the diffusion into the amorphous regions is reduced;

- there is a temperature-dependent balance between the ionic concentration in amorphous and crystalline regions, so that the carrier number in the Nernst – Einstein relation becomes temperature – dependent.

For many polymer electrolyte systems, however, the situation is much more complicated and such a treatment of the conductivity in these systems is open to doubt. It has been experimentally demonstrated [e.g. 6, 20] that the observed conductivity in many polymer electrolytes is a complicated result of many differing processes. The ionic motion within the continuous elastomeric phase is complicated by such effects as crystallite formation and melting, varying concentrations as crystallites form, interfacial transport of ionic species, ion – pair formation, etc. In the highly crystalline polymer electrolyte systems these effects can be very strong and their role in the transport processes cannot be neglected.

It is clear from the discussion so far that very little is known in terms of the transport processes in the crystalline stoichiometric polymer electrolytes. These materials are assumed to be insulating and therefore no attempts have been made to examine the transport processes in these concentrated polymer – salt systems.

1.4. Advances in the structural studies of polymer electrolytes

The structures of polymer electrolytes are very complex and therefore it is difficult to understand and interpret many of the bulk properties and, in particular, the ion transport phenomena. Ion transport in polymer electrolytes is closely related to structural aspects such as ion-polymer and ion-ion coordination. These structural issues have been addressed through spectroscopic and crystallographic studies.

Infrared and Raman spectroscopy have been used to study ion-polymer and ion-ion interactions in both crystalline and amorphous complexes over a wide concentration and temperature range [21-27]. These studies rely on monitoring changes in the vibrational modes of anions such as CF_3SO_3^- , ClO_4^- , AsF_6^- , etc. as their immediate environment changes. Also, vibrational spectra for polymer electrolytes include low-frequency modes characteristic of the cation vibrating in its polymer/anion environment, and vibrational frequencies characteristic of the polymer. The spectroscopic studies give evidence for the presence of ion aggregates (pairs, triples, or larger clusters) in many polymer electrolytes. It has been shown [25] that with changing salt concentration in the range 30:1 to 5:1 in PEO based systems, there is a displacement of the equilibrium between contact ion pairs, triples and possibly larger clusters. The spectroscopic data also indicate that ion triples replace ion pairs as the salt concentration increases and that ion aggregation increases with increasing temperature. Vibrational spectroscopic studies of stoichiometric polymer electrolytes [24] have shown that the local structure of the crystalline phase and the corresponding melt is very similar. The differences arise only from a loss of long range order that is related to a loss of register between adjacent PEO chains and some disordering of the helical torsion angles.

Extended X-ray absorption fine structure (EXAFS) studies are particularly well suited for systems containing multi-valent cations. EXAFS studies also give evidence for the existence of ion pairing [25, 28].

Crystallographic studies can provide the most detailed information on the structure of the crystalline polymer electrolytes. Many polymer electrolytes can be prepared as crystalline complexes and these are well suited for powder X-ray or neutron diffraction studies.

Major advances have been recently made in establishing the crystal structures of the stoichiometric polymer-salt complexes using powder diffraction data [8, 29-37]. The crystal structure determination of these materials is a challenging crystallographic problem due to their complexity and high degree of structural flexibility. Much of the progress in this field involves *ab initio* structure determination, i.e. structure determination without any prior model for the structure [8, 32, 34, 37]. In several cases, crystal structures have been solved by means of the simulated annealing procedure [8, 34, 37] which is capable of solving the structures of complex and flexible molecules.

The structural studies demonstrate that, depending on the composition, the crystalline polymer-salt complexes can form very different structures in terms of polymer chain conformation, ion-ion and ion-polymer coordination.

In the polymer-salt complexes of composition 3:1 and 4:1 containing alkali metal ions ranging from Li^+ to Rb^+ , the PEO chain adopts a helical conformation with cations located inside the helix despite a doubling in the cation radius from Li^+ to Rb^+ [30-34, 36]. The cations in these complexes are coordinated to the ether oxygens in the polymer chain and to the anions; the anions provide in this way additional coordinating groups to complete the cation coordination. Normally each anion donates coordinating groups for two cations thus acting as a bridge between the cations and forming a continuous anion chain along the PEO - cation coordination set. Each polymer chain is associated with a dedicated set of cations and anions. There are no significant interactions between neighbouring chains and each chain is essentially an isolated coordination complex.

In the stoichiometric complexes of composition 1:1 [35, 37], the PEO chain adopts a stretched zigzag conformation which is unable to wrap the cations. Each cation is coordinated

to only one polymer chain. The cations form zigzag rows running parallel to the PEO chains. The anions are directly coordinated to the cations; each anion cross-links by simultaneously coordinating cations that are coordinated to neighbouring PEO chains.

For the crystalline complexes of composition 6:1 [8], the crystal structure is distinctive when compared with the structures of 3:1 (4:1) and 1:1 complexes. The polymer in this case forms double non-helical chains which interlock to form a cylinder. The Li^+ ions reside within these cylinders and they are not coordinated to the anions.

1.5. References

1. P.G.Bruce, *Solid State Electrochemistry*, Cambridge University Press, 1995
2. F.M.Gray, *Polymer Electrolytes*, RSC materials monographs, The Royal Society of Chemistry, Cambridge, 1997
3. M.B Armand, in *Fast Ion Transport in Solids*, North-Holland, New York, 1979
4. J.M.Parker, P.V.Wright and C.C.Lee, *Polymer*, **22**, 1305 (1981)
5. M.A.Ratner, in *Polymer Electrolyte Reviews*, Ed. By J.R.MacCallum and C.A.Vincent, Elsevier Applied Science Publishers, 1989
6. C.Berthier, W.Gorecki, M.Minier, M.A.Armand, J.M.Chabango and P.Rigaud, *Solid State Ionics*, **11**, 91 (1983)
7. P.G.Bruce, *Phil.Trans.R.Soc.London A*, **354**, 415 (1996)
8. G.MacGlashan, Y.Andreev and P.G.Bruce, *Nature*, **398**, 792 (1999)
9. D.E.Fenton, J.M.Parker and P.V.Wright, *Polymer*, **14**, 589 (1973)
10. F.M.Gray, *Solid polymer Electrolytes: Fundamentals and technological applications*, VCH Publishers Inc., 1991
11. W.H.Meyer, *Adv.Mater.*, **10**, No.6, 439 (1998)

12. D.Fauteux, A.Massucco, M.McLin, M.van Buren and J.Shi, *Electrochim.Acta*, **40**, No.13-14, 2185 (1995)
13. P.V.Wright, Y.Zheng, D.Bhatt, T.Richardson and G.Ungar, *Polym.Int.*, **47**, 34 (1998)
14. D.Golodnitsky and E.Peled, *Electrochim.Acta*, **45**, 1431 (2000)
15. M.L.Williams, R.F.Landel and J.D.Ferry, *J.Amer. Chem.Soc.*, **77**, 3701 (1955)
16. M.H.Cohen and D.Turnbull, *J.Chem.Phys.*, **31**, 1164 (1959)
17. J.H.Gibbs and E.A.di Marzio, *J.Chem.Phys.*, **28**, 373 (1958)
18. G.Adams and J.H.Gibbs, *J.Chem.Phys.*, **43**, 139 (1965)
19. M.A.Ratner and A.Nitzan, *Faraday Disc.Chem.Soc.*, **88**, 19 (1989)
20. W.Gorecki, R.Andreani, C.Berthier, M.Armand, M.Mali, J.Ros and D.Brinkmann, *Solid State Ionics*, **18/19**, 295 (1986)
21. B.L.Papke, M.A.Ratner and D.F.Shriver, *J.Electrochem.Soc.*, **129**, 1434 (1982)
22. D.Tetters and R.Frech, *Solid State Ionics*, **18/19**, 271 (1986)
23. M.Kakihana, S.Sanchez and L.M.Torell, *J.Chem.Phys.*, **92**, 6271 (1990)
24. R.Frech, S.Chintapalli, P.G.Bruce and C.A.Vincent, *J.Chem.Soc., Chem.Comm.*, 157 (1997)
25. L.M.Torell and S.Schantz, in *Polymer Electrolyte Reviews*, Vol.2, Ed.J.R.MacCallum and C.A.Vincent, Elsevier Applied Science Publishers, 1989
26. W.Huang, R.Frech and R.Wheeler, *J.Phys.Chem.*, **98**, 100 (1994)
27. R.Frech and W.Huang, *Macromolecules*, **28**, 1246 (1995)
28. R.J.Latham, R.G.Linford and W.S.Schlindwein, *Faraday Discuss.Chem.Soc.*, **88**, 103 (1989)
29. P.G.Bruce, *Electrochim.acta*, **40**, 2077 (1995)
30. P.Lightfoot, M.A.Mehta and P.G.Bruce, *Science*, **262**, 883 (1993)
31. P.Lightfoot, M.A.Mehta and P.G.Bruce, *J.Mater.Chem.*, **2(4)**, 379 (1992)
32. P.Lightfoot, J.L.Nowinski and P.G.Bruce, *J.Amer.Chem.Soc.*, **116**, 7469 (1994)
33. Y.Chatani and S.Okamura, *Polymer*, **28**, 1815 (1987)
34. Y.G.Andreev, P.Lightfoot and P.G.Bruce, *Chem.Comm.*, 2169 (1996)

- 35. Y.Chatani, Y.Fujii, T.Takayanagi and A.Honma, *Polymer*, **331**, 2238 (1990)
- 36. J.B.Thomson, P.Lightfoot and P.G.Bruce, *Solid State Ionics*, **85**, 203 (1996)
- 37. Y.Andreev, G.MacGlashan and P.G.Bruce, *Phys.Review B*, **55**, No18, 12011

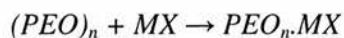
CHAPTER 2

METHODS FOR PREPARATION

2.1. GENERAL CONSIDERATIONS

This chapter describes the procedures for the preparation of the polymer – salt complexes and the experimental results obtained for the samples PEO_n : $LiXF_6$ ($X = P, As, Sb$).

The formation of the complex can be represented by the following reaction:



where MX is the salt and n gives the relative stoichiometry of the polymer repeating unit to the salt.

Physical characteristics as melting temperature, glass transition temperature, viscosity, relaxation times, etc. show that a new compound is formed rather than a simple physical mixture.

There are several methods for the preparation of stoichiometric polymer-salt complexes. The choice of method depends on the properties of the complex under investigation, its thermal

stability and the use of the complex (i.e. whether the material is needed in the form of thin film, or powder). Due to air- and water-sensitivity of most systems, polymer-salt complexes must be prepared in inert atmosphere (Ar-filled glove-boxes).

Solvent casting

This is the most common method for preparing thin polymer electrolyte films. The procedure consists in dissolving stoichiometric amounts of the polymer and the salt in a solvent that dissolves both salt and polymer (e.g. acetonitrile or methanol), or a co-solvent. The resulting solutions are cast on inert supports and the solvent is allowed to evaporate slowly at room temperature. The films are then dried under dynamic vacuum to remove the residual solvent. Infrared spectroscopy can be used to confirm that there is no residual solvent in the samples.

In general, the solvent casting method can be used for the preparation of any polymer-salt complex. Very often, this is the only possible method for the preparation of complexes in which the cations of the salt are not mobile and hence their diffusion directly into the polymer is very limited. The solvent casting method is particularly useful for the preparation of thermally unstable complexes which often cannot be prepared by any other method. By suitable choice of solvent and annealing regime, films of very good quality can be obtained.

Hot pressing

This is a straightforward method for preparing relatively thick polymer electrolyte films (100 μ m – 1mm). At first the polymer and the salt are ground at liquid nitrogen temperature. This ensures that the polymer is below T_g so that it is a glass and can be successfully ground. The resulting powder is pressed between two stainless steel disks to form a polymer electrolyte disk. A pressure of 2-5.10³kg/cm² is applied for 30sec and the assembly is then heated for 3-4 hours in absence of applied pressure to promote reaction between the polymer and the salt. The

temperature of heating is chosen according to the thermal properties of the specific complex (usually temperature as high as the melting point of the complex is needed, or at least temperature above the melting point of the polymer). Upon cooling to 60-80°C, a pressure of 1.5 – 2.10³kg/cm² is applied and the sample is allowed to cool slowly to room temperature. The major disadvantage is that thermally unstable complexes cannot be obtained by this method.

Preparation in capillaries

This method is applied mainly in the structural studies of polymer-salt complexes, in particular where diffraction data in transmission mode from a capillary sample give more reliable intensities than from flat samples. Stoichiometric amounts of the polymer and the salt are ground at liquid nitrogen temperature for 30min and the resulting powder is sealed in 0.5 - 0.7mm Lindemann glass capillaries. The samples are then heated for several hours usually at temperature close to the melting point of the complex in order to promote reaction between the polymer and the salt. To achieve better crystallinity, the samples are then annealed at lower temperature for 2 – 4 days. This method is very useful for preparing samples for X-ray diffraction studies but its application is limited in the case of thermally unstable complexes.

Preparation of powder samples

This method is similar to that for preparation in capillary except for the scale of the quantities. Since large quantities are used, it is of considerable importance to ensure that the polymer and the salt are thoroughly mixed. Therefore, stoichiometric amounts of the polymer and the salt are ground at liquid nitrogen temperature for long time intervals (~60min) to obtain uniform mixture, and the resulting powder (2 - 5g) is then sealed in glass vial (in Ar atmosphere) and heated at appropriate temperature to obtain the polymer-salt complex. The method is very suitable for preparing relatively big amounts of powder samples that are necessary for NMR

experiments, neutron diffraction studies, etc. Again, the major drawback is that the method cannot be applied for the preparation of thermally unstable complexes.

2.2. RESULTS AND DISCUSSION

The polymer – salt complexes were prepared using polyethylene oxide of various molecular weight (100,000, 2,000 and 1,000). In this work, the high-molecular weight polymer ($M_w = 100,000$) is referred to as polyethylene oxide (PEO); the low-molecular weight polymers (polyethylene glycol dimethyl ethers of $M_w = 2,000$ and 1,000) which are below the entanglement limit for PEO of 3,200 are referred to as polyethylene glycol (PEG). The polymers used in the present work were polydisperse ($M_n/M_w = 1.08$). The X-ray diffraction patterns of all polymers were the same irrespective of the molecular weight.

The high molecular weight polymer ($M_w = 100,000$) was dried at 45-50°C under dynamic vacuum for 3 – 4 days to remove any residual water. The polymers of lower molecular weight (polyethylene glycol dimethyl ethers 2,000 and 1,000) were dried under dynamic vacuum at room temperature for 3-4 days. All manipulations were performed in an Ar-filled dry glove box. The X-ray diffraction data were collected on Stoe Stadi/P diffractometer in transmission mode, operating with Cu-K α_1 radiation and fitted with a Ge monochromator. The data were collected using a small angle (6° in 2θ) linear position sensitive detector in steps of 0.02° in 2θ .

2.2.1. PEO₆:LiPF₆

LiPF₆ is a salt widely used in lithium batteries. Diluted LiPF₆ polymer electrolytes, based on PEO have been studied [1, 2] but there are no systematic studies on the stoichiometric complexes of the system PEO_n:LiPF₆.

In this work, the complex PEG₆:LiPF₆ has been prepared and the X-ray diffraction pattern is shown in fig 2.1. There are no reflections associated with pure salt or polymer. The examination of peak positions suggests that the complex PEG₆:LiPF₆ is isostructural with PEO₆:LiAsF₆ [3].

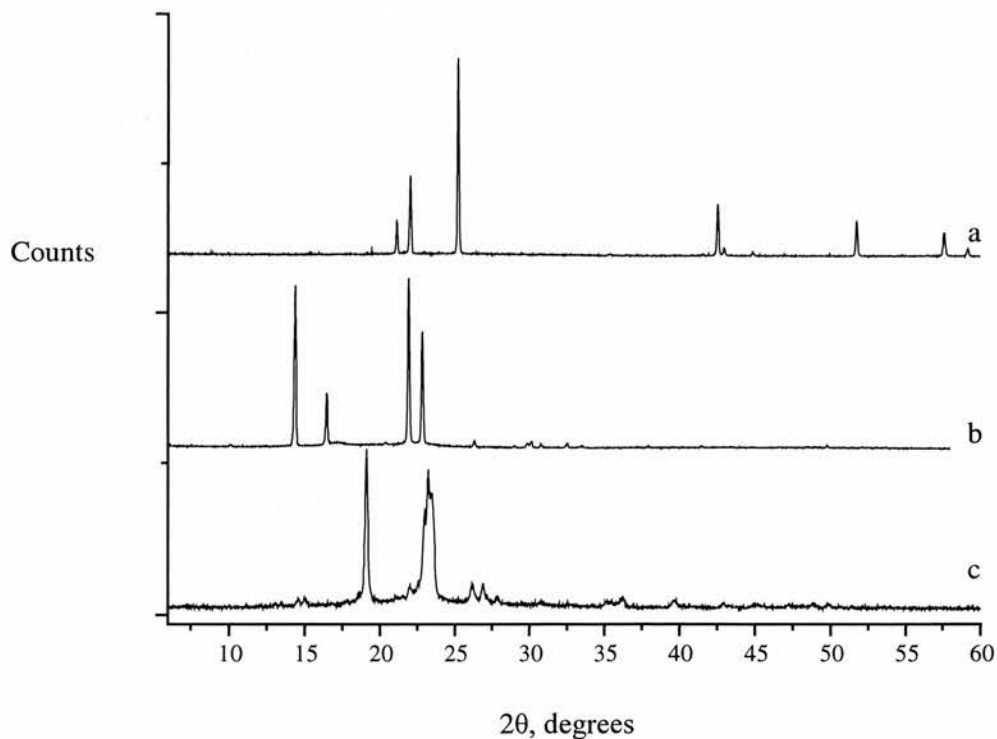


Fig. 2.1. X-ray diffraction patterns of: a) LiPF₆, b) PEG₆:LiPF₆ ($M_w = 1,000$), c) PEG ($M_w = 1,000$)

The complex $\text{PEO}_6\text{:LiPF}_6$ could be prepared by the solvent casting method only. Occasionally, the complex could be prepared in capillaries but no reproducible results were obtained. The complexes of LiPF_6 were thermally unstable and difficult to handle owing to sensitivity to air, moisture and light.

2.2.2. $\text{PEO}_n\text{:LiAsF}_6$ complexes

Robitaille and Fauteux [4] reported the phase diagram of the system $\text{PEO}_n\text{:LiAsF}_6$; they found that two stoichiometric complexes, $\text{PEO}_3\text{:LiAsF}_6$ and $\text{PEO}_6\text{:LiAsF}_6$, are formed.

The 6:1 system was of particular interest in the present work since this was the first 6:1 complex the crystal structure of which had been determined [3]. The complex 6:1 was prepared by several methods (fig.2.2) and the X-ray diffraction patterns were essentially the same irrespective of the method of preparation. They compared very well with the histogram reported in [4].

Two effects can be seen in a more detailed examination of the X-ray diffraction data. First, there is evidence of preferred orientation (difference in the relative intensities of the peaks). It was found that this was not related in a simple way to the preparation method since different degrees of preferred orientation effects were observed in samples obtained by one and the same method. Second, there is evidence of hkl dependent peak broadening (difference in peak width at half-height for the peaks at ~ 16.5 and 22° in 2θ). This indicates that the crystallites are coherent on different length scales in different crystallographic directions.

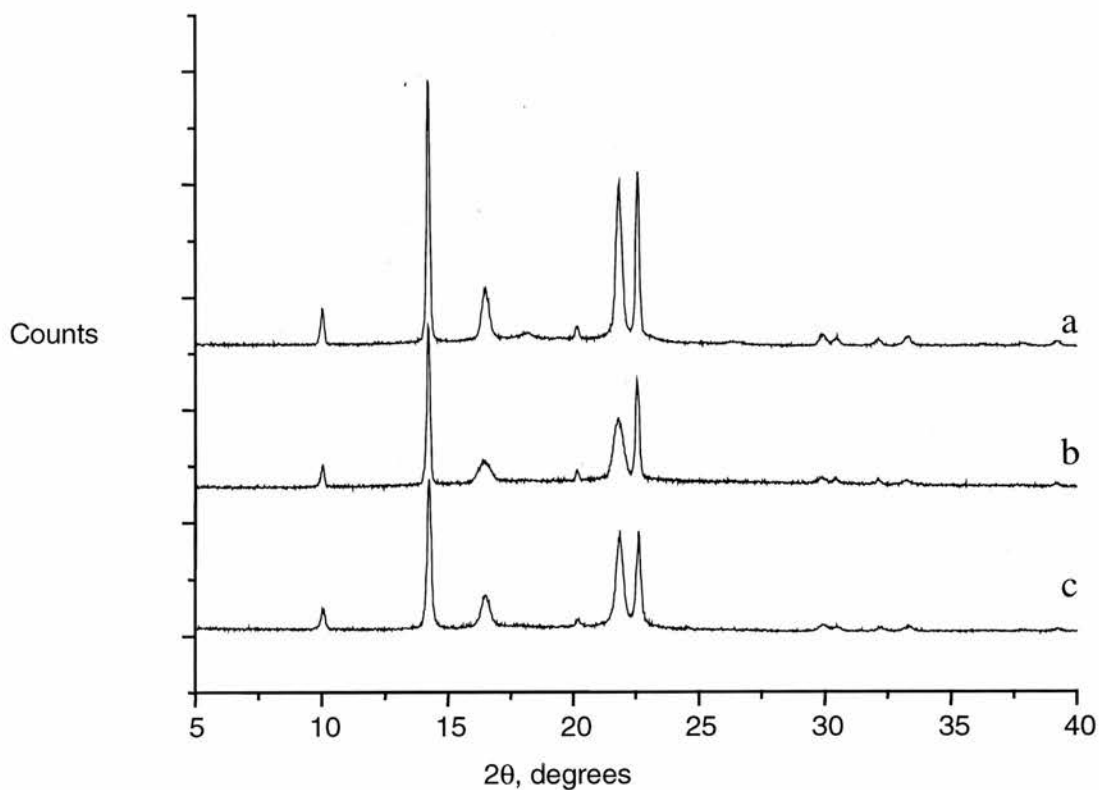


Fig.2.2. X-ray diffraction patterns of the complex $\text{PEO}_6\text{:LiAsF}_6$ prepared by different methods: a) powder sample, b) capillary, c) hot pressing

The preparation of the 3:1 complex was not so straightforward; this complex was very unstable when exposed to air, water or heat. Solvent casting, followed by very careful annealing, was the only possible method for the preparation of the complex. The X-ray diffraction pattern (fig.2.3) was in good agreement with the histogram reported in [4]. The peak-to-background ratio for this complex, however, was poor and there was a broad background “hump” between 10 and 25° in 2θ. This indicated the presence of significant fraction of amorphous material.

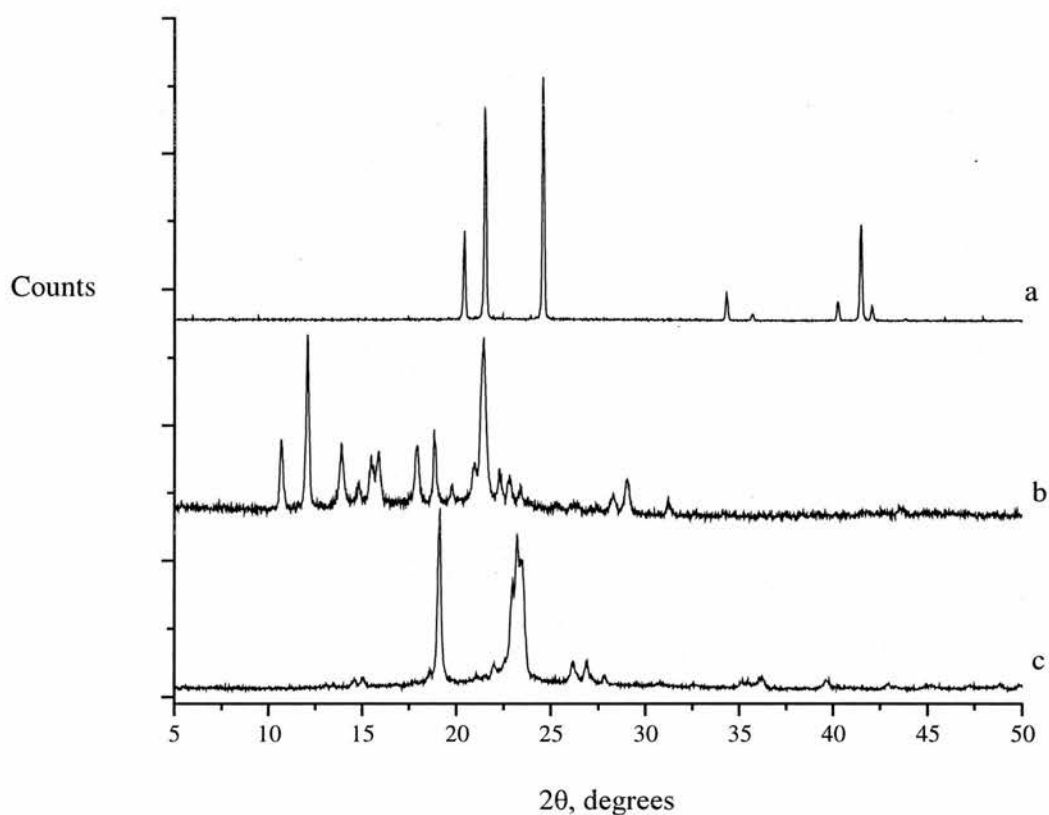


Fig.2.3. X-ray diffraction patterns of: a) LiAsF_6 , b) $\text{PEO}_3:\text{LiAsF}_6$, c) PEO

2.2.3. $\text{PEO}_n:\text{LiSbF}_6$ complexes

Stoichiometric crystalline complexes

The system $\text{PEO}_n:\text{LiSbF}_6$ is a new polymer electrolyte system. There are no literature data on the existence of stoichiometric complexes, or other studies of this system. It can be expected, by analogy with the system $\text{PEO}_n:\text{LiAsF}_6$ that stoichiometric complexes 3:1 and 6:1 are formed.

The experimental results indicate (fig.2.4) that only one stoichiometric complex is formed, $\text{PEO}_6:\text{LiSbF}_6$. The X-ray diffraction pattern of the complex $\text{PEO}_6:\text{LiSbF}_6$ is very similar to the pattern of $\text{PEO}_6:\text{LiAsF}_6$ (fig.2.2). This suggests that the two complexes are iso-structural.

In general, the kinetics of crystallisation for the complex 6:1 was much slower than in the case of $\text{PEO}_6:\text{LiAsF}_6$. Perhaps this is attributable to the bigger size of the anion SbF_6^- . The complex $\text{PEO}_6:\text{LiSbF}_6$ could be prepared in glass capillaries, or as a powder sample, but in these cases the crystallinity was very poor. As expected, the preparation by the solvent casting method produced samples of better crystallinity due to the faster rate of complex formation in solution.

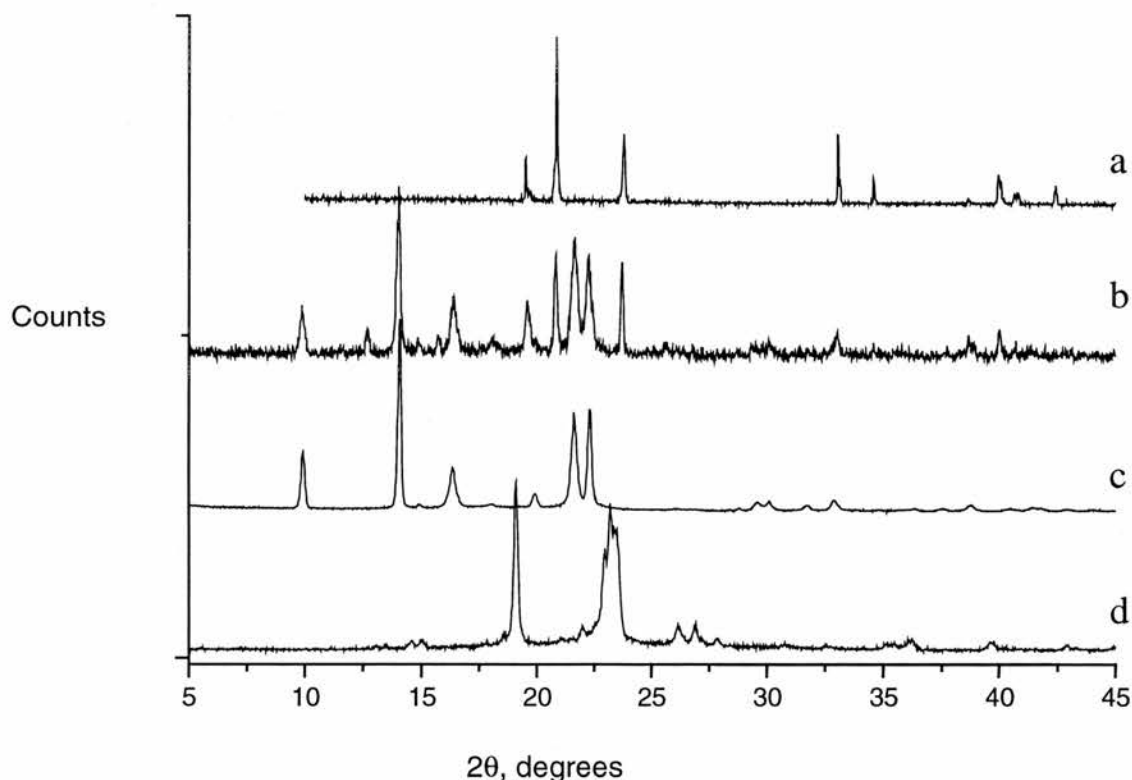


Fig.2.4. X-ray diffraction patterns of: a) LiSbF_6 ; b) $\text{PEO}_3:\text{LiSbF}_6$; c) $\text{PEO}_6:\text{LiSbF}_6$; d) PEO

The complex of composition 3:1 appears to be a mixture of pure salt and stoichiometric 6:1 complex. The absence of stoichiometric 3:1 complex may be a consequence of the bigger size of the anion SbF_6^- (29% increase in anion size compared to AsF_6^-) which can not be accommodated in the typical structure of a 3:1 complex. However, careful inspection of the data in fig.2.4 shows that there are at least two small peaks which are not associated with 6:1 complex or pure salt (at 13° and 16° in 2θ). It is not clear whether these peaks are due to some impurities, or to the formation of a second stoichiometric complex.

Amorphous complex $\text{PEO}_6\text{:LiSbF}_6$

The complex $\text{PEO}_6\text{:LiSbF}_6$ could be obtained as either crystalline or amorphous material depending on the method of preparation. Attempts were made to prepare amorphous $\text{PEO}_6\text{:LiPF}_6$ and $\text{PEO}_6\text{:LiAsF}_6$ by quenching but these were not successful. Amorphous $\text{PEO}_6\text{:LiSbF}_6$ could be obtained by the hot pressing method. The X-ray diffraction pattern of the amorphous sample (fig.2.5) consisted of high amorphous background and no peaks for pure salt or pure crystalline PEO were observed. This confirmed that the salt had dissolved in the polymer, forming a completely disordered compound. The amorphous complex $\text{PEO}_6\text{:LiSbF}_6$ was metastable and it started to transform to crystalline $\text{PEO}_6\text{:LiSbF}_6$ after 1-2 days of storage.

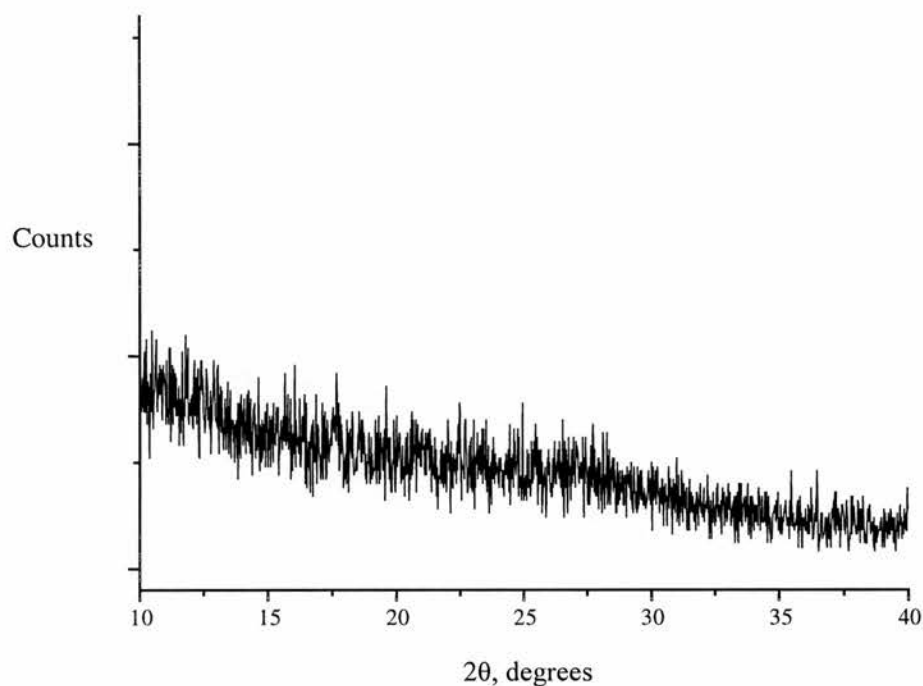


Fig.2.5. XRD pattern of the amorphous complex PEO₆:LiSbF₆

2.2.4. Influence of molecular weight of the polymer

The influence of molecular weight on the degree of crystallinity was examined for the systems PEO₆:LiPF₆ and PEO₆:LiSbF₆. It was found that the degree of crystallinity could be changed significantly as shown in fig.2.6 for the complex PEO₆:LiPF₆. The same results were obtained for the complex PEO₆:LiSbF₆.

When polymer of low molecular weight ($M_w = 2,000$ or $1,000$) is used, the crystallinity improves in two ways. First, the peak-to-background ratio is increased and this indicates that the

fraction of amorphous material is significantly reduced (the intensities shown in fig.2.6 are normalised). Second, the peak width (full-width at half maximum) in the X-ray diffraction patterns decreases, suggesting that the crystallite size is optimized and larger crystallites are obtained. Also, the hkl dependent peak broadening in the high molecular weight complexes is no longer observed in the low molecular weight analogues.

It should be noted that these results were observed systematically for many samples. The peak positions in the X-ray diffraction patterns were the same irrespective of the molecular weight of the polymer in the range $M_w = 1,000 \div 100,000$. The relative intensities varied due to

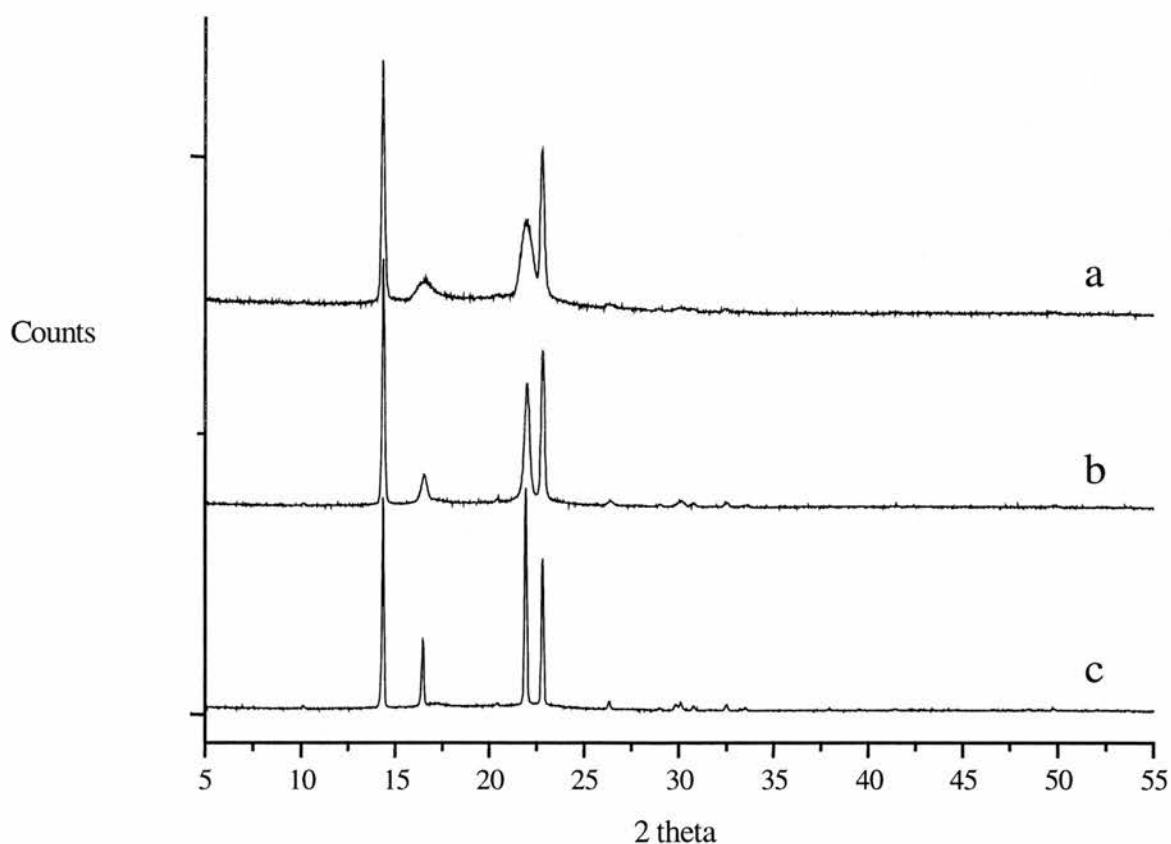


Fig.2.6. X-ray diffraction patterns of the complex $PEO_6:LiPF_6$ prepared with polymer of different molecular weight: a) $M_w = 100,000$; b) $M_w = 2,000$; c) $M_w = 1,000$

preferred orientation effects. The results confirmed that the crystal structure of the stoichiometric 6:1 complexes was preserved when the molecular weight of the polymer was varied in the above mentioned range.

2.3. Conclusions

There is a variety of methods for the preparation of the stoichiometric crystalline complexes $\text{PEO}_6\text{:LiXF}_6$ ($X = \text{P, As, Sb}$). This allows one to optimise the preparation procedure for each specific complex in order to obtain samples of very good quality. The X-ray diffraction data demonstrate that while the method of preparation does not influence the crystal structure of the complexes, the microstructure and texture can be effected significantly. The degree of crystallinity can be improved by the choice of suitable conditions for the preparation.

2.4. References

1. C.Vincent, *Electrochim.Acta*, **40**, No13-14, 2035 (1995)
2. S.Arumagam, J.Shi, D.Tunstall and C.A.Vincent, *J.Phys.C*, **5**, 153 (1993)
3. G.MacGlashan, Y.Andreev and P.G.Bruce, *Nature*, **398**, 792 (1999)
4. C.D.Robitaille and D.Fauteux, *J.Electrochem.Soc.*, **133**, No2, 315 (1986)

CHAPTER 3

THERMAL PROPERTIES

3.1. DIFFERENTIAL SCANNING CALORIMETRY (DSC)

3.1.1. General considerations

The thermal properties of polymer electrolytes are very important for the application of these materials. Knowledge of the thermal properties is necessary when performing various experiments and measurements. The thermal behaviour of the crystalline PEO – salt complexes depends, in general, on the overall EO:salt molar ratio, the PEO molecular weight, the method of preparation and the thermal history [1].

The commonly applied method for studying the thermal properties of polymer electrolytes is DSC. In DSC, the equipment is designed to allow a quantitative measure of the enthalpy changes that occur in a sample as a function of either temperature or time. In the

“power compensated” DSC which has been employed in the present work, the heat evolved or absorbed by the sample is compensated for by using an electrical heater located under the sample, to maintain the sample at the programmed cell temperature. The electrical work done to maintain dynamic equilibrium should be a true measure of the heat flow.

The DSC technique has been designed for use with small samples in the range 0.5 to 20 mg. The sample response is affected by both instrumental factors and sample characteristics. Variables include sample holder material, size and geometry, heating rate, furnace atmosphere and flow rate. Sample effects include those of particle size, weight, heat capacity, thermal conductivity, volatility and distribution in the sample pan [2, 3, 4, 5].

Applications of DSC to monomer and polymer systems involve determination of the following physical properties: temperatures and heats of melting, crystallisation and other first-order transitions such as evaporation, sublimation and solid-solid transitions, temperatures and changes of specific heat at glass transitions, kinetics of the above phenomena.

Applications to physical phenomena include: determination of phase diagrams of polymer systems, determination of glass transitions, determination of fractional crystallinity and identification of crystalline phases present, molecular weight dependence of polymer systems, salting-out effects of inorganic salts in polymer electrolytes, etc. [4, 5].

3.1.2. Experimental results and discussion

DSC experiments were performed on Perkin-Elmer DSC-7 at a programmed heating rate of 10°C/min. Test measurements were also carried out at heating rates of 5°C/min and 20°C/min but no differences in the results were observed. Temperature intervals for DSC analysis were chosen according to the properties of the sample under investigation. Samples were typically 2 – 5mg in weight and these were sealed under Ar atmosphere in aluminium DSC pans.

DSC measurements of this complex indicate that there is strong dependence between the thermal properties of the samples and the molecular weight of the polymer used for the preparation. DSC scans for complexes of different molecular weight are shown in fig.3.1. No peaks for melting of pure (uncomplexed) crystalline polymer are observed.

The onset of melting is observed at different temperatures depending on the molecular weight of the samples. The samples prepared with low-molecular weight polymer melt at lower temperature compared to the samples prepared with high-molecular weight polymer.

The endothermic features observed in the DSC traces for the complexes of $M_w = 100,000$ and $2,000$ consist of two (or more) overlapping peaks which is an indication of more complex thermal events but not only melting. It can be suggested that decomposition or salt precipitation occur along with melting of the crystalline complex.

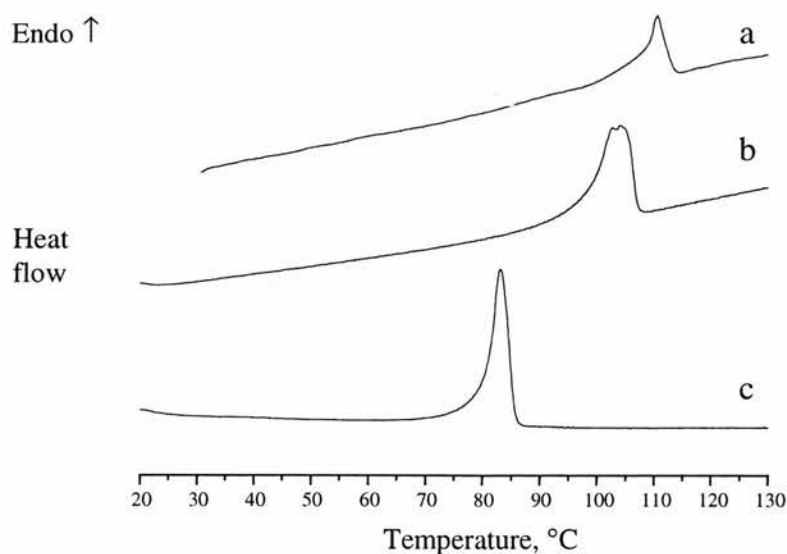


Fig.3.1. DSC measurements of the complexes PEO₆:LiPF₆ of different molecular weight: a) $M_w = 100,000$; b) $M_w = 2,000$; c) $M_w = 1,000$. All traces are on heating.

The samples of different molecular weight have different thermal properties on the cooling cycles of the DSC scans. No thermal event is observed on cooling for the complexes of $M_w = 100,000$ and $2,000$. This may be due to slow rate of recrystallisation, in which case the melting of the crystalline complexes occurs as an irreversible process in the DSC time scale. It is also possible that the endothermic events recorded on the first heating cycles of these complexes are due to simultaneous melting and salt precipitation, or decomposition of the samples. In the latter case, no thermal event will occur on cooling of the samples. Further studies and preparations by different methods have confirmed that these complexes decompose on heating with changing the appearance and colour of the samples.

One exothermic peak on cooling is observed for the complex of $M_w = 1,000$ (fig.3.2.) and this peak can be attributed to a re-crystallisation process of the crystalline 6:1 complex. The temperature of recrystallisation is lower than the melting temperature. It should be noted that it is common to observe such a hysteresis in the DSC analysis [2]. Hysteresis depends not only on the nature of the material and the structural changes involved (e.g. transitions which involve breaking of strong bonds exhibit much hysteresis) but also on the experimental conditions such as the heating and cooling rates. If the cooling rate is sufficiently fast, the transition can be suppressed completely and the transition is then effectively irreversible under these particular experimental conditions.

It can be seen in fig.3.2 that the peak for the recrystallisation process is broader than the corresponding peak for melting. This may indicate a slow rate of recrystallisation.

It is interesting to note that a single endothermic peak for melting, and exothermic peak for recrystallisation have been observed only for the complex of $M_w = 1,000$. This can be due to better heat dissipation in the low molecular weight complex so that decomposition does not occur in the time scale of the DSC experiment.

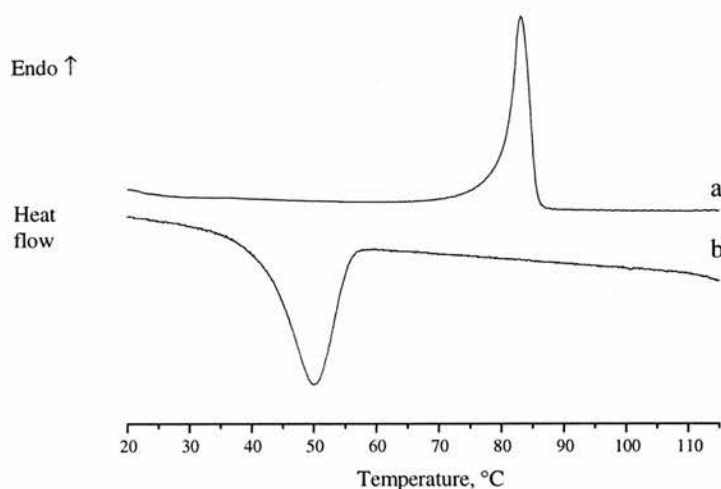


*Fig.3.2. DSC traces for the complex $PEG_6:LiPF_6$ of $M_w = 1,000$:
a) heating, b) cooling*

$PEO_6:LiAsF_6$

The DSC traces for the complexes of molecular weight $M_w = 100,000$, $2,000$ and $1,000$ are shown in fig.3.3. The results are different for the complexes of different molecular weight. Also, the results are different from those obtained for the complexes $PEO_6:LiPF_6$. The endothermic event observed on heating of the high molecular weight complex ($M_w = 100,000$) probably reflects a melting process. This view is reinforced by the DSC results obtained on cooling of the complex (discussed later). In the case of the low molecular weight complexes ($M_w = 2,000$ and $1,000$), two well resolved endothermic events are observed. The relevant phase transitions appear to be similar to these observed for the complex $PEO_6:LiSbF_6$ (discussed later in more detail).

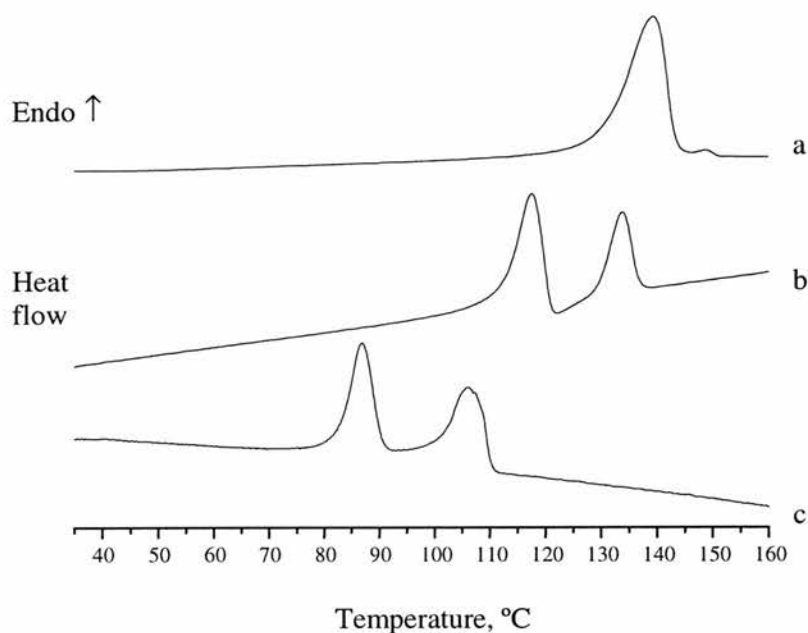


Fig.3.3. DSC measurements for the complexes $PEO_6:LiAsF_6$ of different molecular weight: a) $M_w = 100,000$, b) $M_w = 2,000$, c) $M_w = 1,000$. All traces are on heating.

In contrast to the system $PEO_6:LiPF_6$, recrystallisation process is observed only in the case of the high molecular weight complex (fig.3.4). Two features can be seen in the traces in fig.3.4. First, the temperature of recrystallisation is lower than the melting temperature and second, the area of the peak on recrystallisation was smaller than the peak area on melting. These results can be explained with slow kinetics of re-crystallisation as already discussed for the complex $PEG_6:LiPF_6$ ($M_w = 1,000$).

It is interesting to note that the high molecular weight complex $PEO_6:LiAsF_6$ ($M_w = 100,000$) shows better thermal stability than the complex $PEO_6:LiPF_6$ of the same molecular weight. This can be attributed to the poor thermal stability of the salt $LiPF_6$ which also appears to influence the stability of the polymer-salt complex.

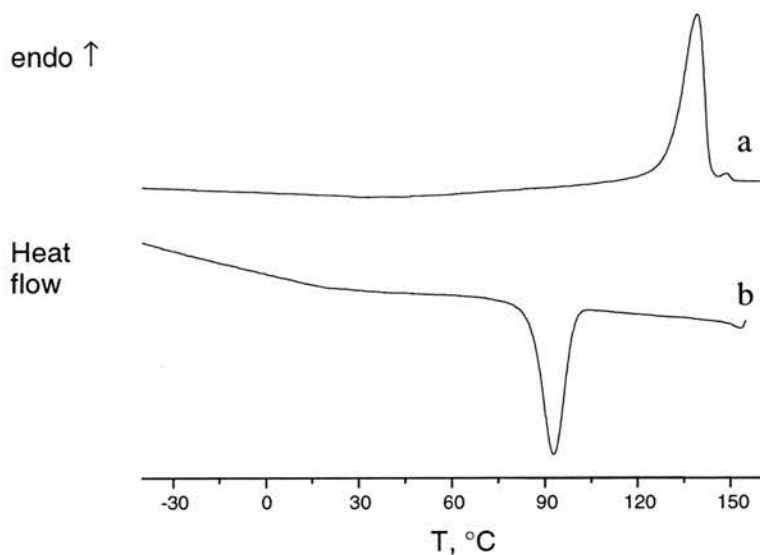


Fig.3.4. DSC traces for the complex $PEO_6:LiAsF_6$ ($M_w = 100,000$)
a) heating, b) cooling

$PEO_6:LiSbF_6$ (crystalline complex)

Similarly to the other 6:1 complexes, the thermal behaviour of the complex $PEO_6:LiSbF_6$ was dependent on the molecular weight of the polymer (fig.3.5.). In the case of the high molecular weight complex ($M_w = 100,000$), the endothermic peak on heating probably corresponds to two overlapping processes. Also, a small endothermic peak is observed at $\sim 55^\circ\text{C}$ that can be attributed to melting of crystalline PEO. The presence of small fraction of pure polymer has been confirmed in all samples of molecular weight 100,000 and this can be related to the very slow kinetics of crystallisation of this complex.

Two well defined endothermic peaks can be seen in the DSC traces for the low molecular weight complexes ($M_w = 1,000$ and $2,000$). No traces of pure crystalline polymer have been found in these compounds.

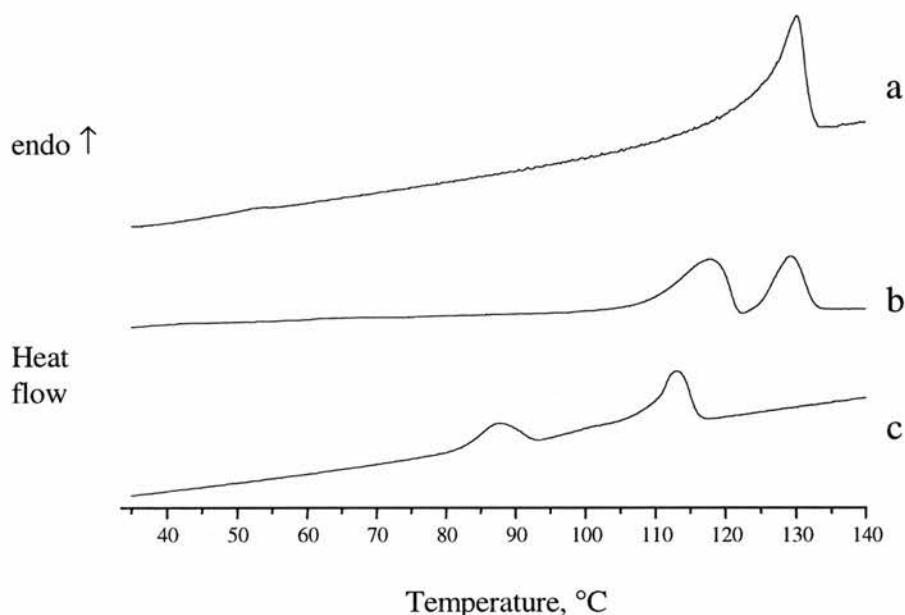


Fig.3.5. DSC measurements of the complex $\text{PEO}_6\text{:LiSbF}_6$ of different molecular weight: a) $M_w = 100,000$, b) $M_w = 2,000$, c) $M_w = 1,000$. All traces are on heating.

Some differences between the complexes of different molecular weight are observed on the cooling processes. The DSC scans on cooling for the complex of $M_w = 100,000$ do not show any thermal event which may be due to very slow rate of re-crystallisation, or the formation of amorphous complex.

For the complexes of $M_w = 2,000$ and $1,000$, one exothermal peak is observed on cooling, and one endothermic peak on the second heating cycle. Taking into account the variable-temperature XRD study of these complexes (discussed later in this chapter), it is suggested that the first peak on the first heating cycle is related to transformation of the complex to another high-temperature phase which has not been identified. The second peak on the first heating cycle is probably related to the melting of this high-temperature phase. All other thermal events observed on the cooling and subsequent heating processes are most

probably due to phase transitions involving this high-temperature phase. Further work on the complexes $\text{PEO}_6\text{:LiSbF}_6$ has confirmed that the phase transition to the high-temperature phase is an irreversible process.

$\text{PEO}_6\text{:LiSbF}_6$ (amorphous complex)

The DSC analysis of this complex did not detect any thermal events in the temperature range from -65°C to 140°C . The glass transition characteristic of the amorphous polymer-salt complexes was not observed. The glass transition for the complex $\text{PEO}_6\text{:LiSbF}_6$ could be expected to occur in the interval from -30°C to -20°C by analogy with other similar systems (e.g. -23°C for $\text{PEO}_8\text{:LiBF}_4$ [6], -27°C for $\text{PEO}_6\text{:LiTFSI}$ [7]).

Since the DSC relies on detecting the heat transfer between two phases (amorphous and glass state), the lack of any thermal event in the DSC traces could be accounted for by a very low heat of glass transition for the complex $\text{PEO}_6\text{:LiSbF}_6$ which could not be measured by this technique. In addition, the minimum quantity of heat that can be observed in any event depends also on the rate of heat evolution during it [4]. A glass transition temperature of around 240K was found for this complex using ^1H NMR spin-spin relaxation studies (discussed in Chapter 6).

3.2. VARIABLE TEMPERATURE X-RAY DIFFRACTION

Variable-temperature X-ray diffraction (VT XRD) is a technique capable of following the appearance or disappearance of crystalline phases as a function of temperature. The nature of the processes involved can be directly revealed. In this work, VT XRD studies were carried out on a Stoe Stadi/P diffractometer operating with $\text{Cu K}\alpha$ radiation and position-sensitive detector. For variable temperature data collection, the system was equipped with a graphite furnace with an X-ray transparent window. The sample was placed in a capillary which was

heated within the furnace. Each powder diffraction pattern was collected over a 4-5-hour-interval and the total time for each variable temperature experiment did not exceed 20 – 24 hours.

3.2.1. Results and discussion

PEO₆:LiAsF₆

VT XRD studies have been carried out for the complex of $M_w = 100,000$ (fig.3.6.). There is a slight shift of peak positions to lower 2θ values on heating. This is most probably attributable to thermal expansion since no discontinuity in the variation of the lattice parameters is observed. Above the melting point ($\sim 140^\circ\text{C}$), a featureless amorphous diffraction pattern is observed (not shown in fig.3.6). The structure is slightly changed at elevated temperatures - one additional peak appears at $\sim 15.5^\circ$ in 2θ and the strongest peaks at $\sim 14^\circ$ and $21 - 23^\circ$ in 2θ change in intensity. Also, the peak at $\sim 22^\circ$ in 2θ is broadened at the higher temperatures. Since this peak consists of several overlapping reflections, it is not clear whether this broadening is related to crystallite size effects, or it results from the variations of the lattice parameters with temperature. As a whole, the powder diffraction patterns are not radically different and the structural changes may be due to continuously increasing disorder of the anions AsF_6^- .

Similar results were reported for the complex $\text{PEO}_6:\text{Ca}(\text{CF}_3\text{SO}_3)_2$ [8] in which case it was suggested that a phase transition between two different polymorphic forms had occurred. The authors in [8] did not comment in detail on the nature of the structural change but it was suggested that the phase transition is associated with rotation of the triflate groups between two sites.

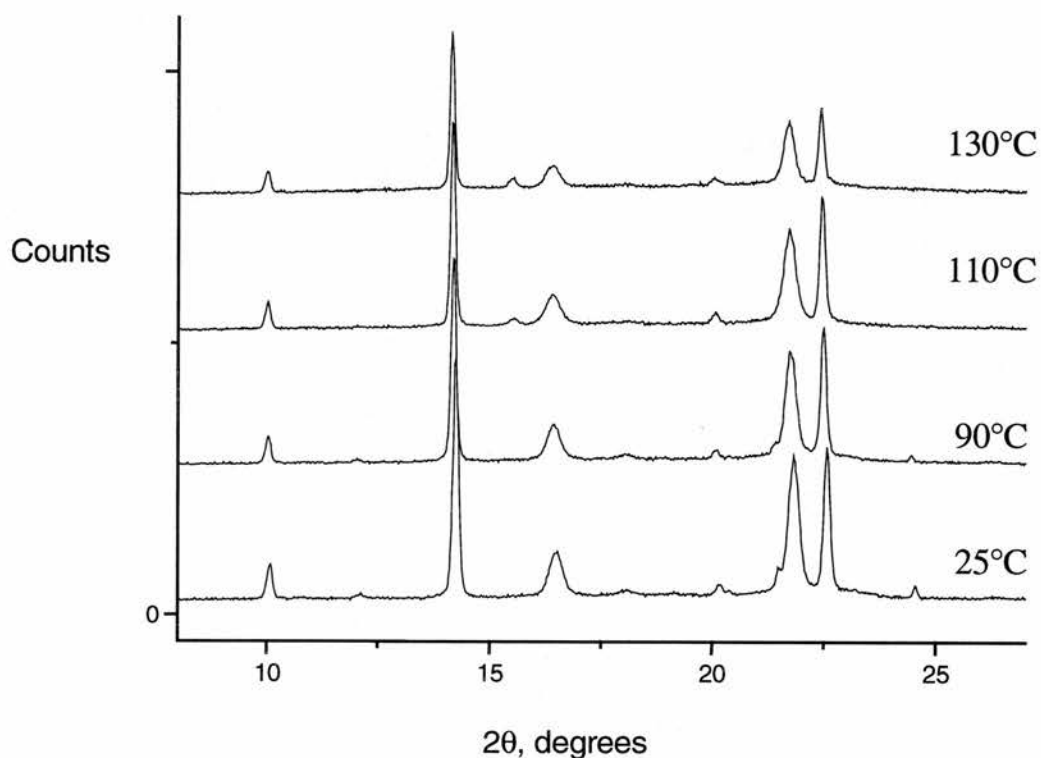


Fig.3.6. X-ray diffraction patterns of the complex $PEO_6:LiAsF_6$ at different temperatures

$PEO_6:LiSbF_6$ complexes

VT XRD experiments were performed on the following samples:

- crystalline complex $PEG_6:LiSbF_6$ (PEG of molecular weight 2,000)
- crystalline complex $PEO_6:LiSbF_6$ (PEO of molecular weight 100,000)
- amorphous complex $PEO_6:LiSbF_6$ (PEO of molecular weight 100,000).

The X-ray diffraction patterns for the complex $PEG_6:LiSbF_6$ ($M_w = 2,000$) at different temperatures (fig.3.7) give no evidence for structural changes up to $\approx 105^\circ\text{C}$. Above 105°C ,

the complex transforms to a new phase but this high-temperature phase has not been identified. The peaks in the diffraction pattern can not be attributed to the salt (LiSbF_6), LiF , or other simple inorganic compounds that might be obtained as decomposition products. This suggests that the nature of the high-temperature phase is more complicated.

In the case of the crystalline complex $\text{PEO}_6\text{:LiSbF}_6$ of molecular weight 100,000, no structural changes are observed up to the melting point, $\approx 120^\circ\text{C}$, above which a featureless amorphous pattern is obtained.

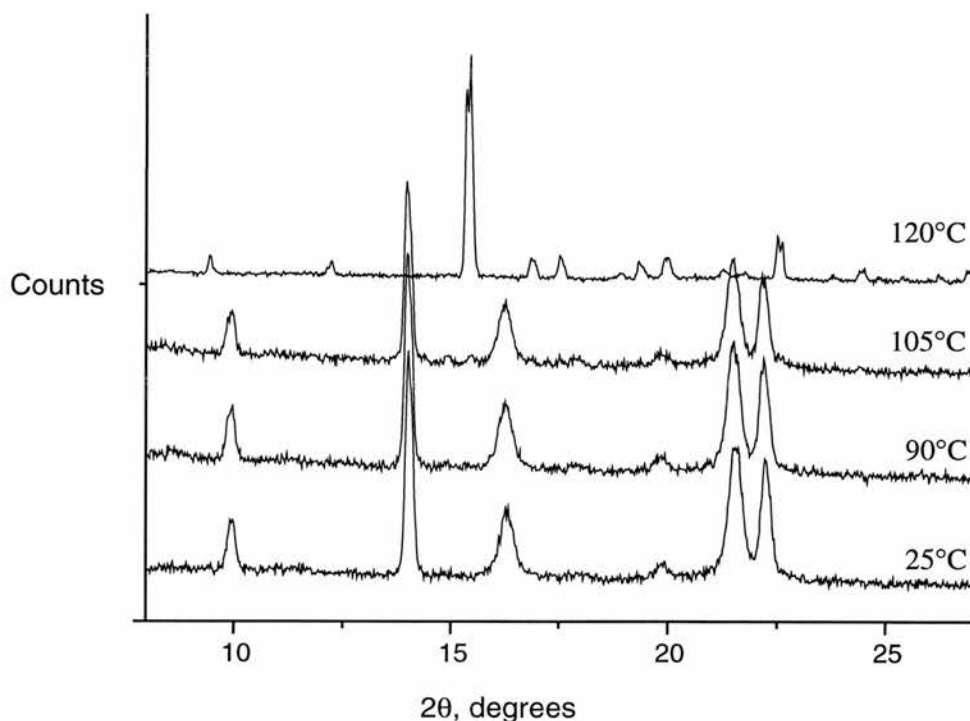


Fig3.7. X-ray diffraction patterns of the complex $\text{PEG}_6\text{:LiSbF}_6$ ($M_w = 2,000$) at different temperatures

These results are different from the experimental data for the complex $\text{PEO}_6\text{:LiAsF}_6$ ($M_w = 100,000$) for which some slight changes in the crystal structure are seen on heating. It should be noted, however, that the quality of the X-ray data collected for the LiSbF_6 – based

complexes may not be sufficiently good and it is possible that these subtle changes can not be detected due to the poor signal-to-noise ratio.

An important result is that the thermal stability is inferior for the complex based on low molecular weight polymer. This complex appears to be more reactive than the corresponding complex based on high molecular weight polymer.

Variable-temperature XRD data for the amorphous complex $\text{PEO}_6\text{:LiSbF}_6$ indicate that there is no change in the degree of amorphisity up to 120-130°C. This result confirms that the amorphous complex $\text{PEO}_6\text{:LiSbF}_6$ is thermally stable and does not transform to a crystalline phase on heating in the temperature range 25-130°C within 20-24 hours.

3.3. CONCLUSIONS

- Thermal stability

The experimental data indicate that the stoichiometric complexes $\text{PEO}_6\text{:LiXF}_6$ ($X = \text{P, As, Sb}$) are thermally stable over limited temperature intervals. Thermal decomposition is a common phenomenon with these compounds. No definite trends have been observed in terms of the thermal stability of the complexes. In general, the low molecular weight complexes show inferior stability. For the high molecular weight complexes, the thermal properties depend mainly on the salt.

To summarise, care must be taken to ensure that the properties of the polymer-salt complexes are studied in suitable temperature ranges in order to avoid thermal decomposition. The nature of the decomposition processes with these compounds has not been studied in details.

- Influence of molecular weight of the polymer

The thermal properties of the stoichiometric complexes $\text{PEO}_6\text{:LiXF}_6$ ($X = \text{P, As, Sb}$) depend strongly on the molecular weight of the polymer used in the preparation. In general, the use of low-molecular weight polymers results in inferior thermal stability of the samples and lower temperatures of phase transitions.

- The application of DSC and XRD

It should be born in mind that DSC is a non-equilibrium dynamic technique and therefore cannot approach the precision and accuracy of the classical calorimetric techniques. Although DSC is a fast and convenient method, the DSC scans are not always true representation of the thermal behaviour of the system under study because of the specific time scale and sample size. In the present work, strong time dependence of the properties has been found for some complexes. When a systematic study of the properties is attempted, it is advisable to use VT - XRD. Although this technique is more time consuming and requires specific equipment, it can provide more reliable and detailed information on the thermal properties of the samples and the nature of the phase transformation processes.

3.4. REFERENCES

1. P.V.Wright, in *Polymer Electrolyte Reviews*, Ed. by J.R.MacCallum and C.A.Vincent, Elsevier Applied Science, 1989
2. A.West, *Solid State Chemistry and its Applications*, J. Wiley&Sons Ltd., 1984
3. Z.Szafran, *Microscale Inorganic Chemistry*, J.Wiley&Sons, 1991
4. R.G.Linford, *Electrochemical Science and Technology of Polymers*, Elsevier Science Publishers, 1990

5. P.E.Slade and L.T.Jenkins, *Techniques and Methods of Polymer Evaluation*, Marcel Dekker Inc., New York, 1970
6. G.Chiodelli, P.Ferloni, A.Magistris and M.Sanesi, *Solid State Ionics*, **28-30**, 1009 (1988)
7. W.Gorecki, M.Jeannin, E.Belorizky, C.Roux and M.Armand, *J.Phys.:Condens.Matter*, **7** 6823 (1995)
8. M.A.Mehta, P.Lightfoot and P.G.Bruce, *Chem.Mater.*, **5**, 1338 (1993)

CHAPTER 4

CRYSTAL STRUCTURE STUDIES

4.1. STRUCTURE REFINEMENT WITH POWDER DIFFRACTION DATA

4.1.1. Theoretical background

X-ray diffraction is one of the most important techniques for structural characterisation of crystalline solids. Single-crystal X-ray diffraction is now used routinely for crystal structure determination. Many crystalline solids, however, cannot be prepared as single crystals of sufficient size and quality and then the structural information has to be extracted from powder diffraction data [1-4].

Crystal structure determination from powder diffraction data can be divided into three stages:

1. determination of lattice parameters and assignment of crystal symmetry and space group;
2. structure solution which involves determination of initial structural model;
3. structure refinement which involves refinement of model obtained in the structure solution stage, against the experimental diffraction data.

The present work has been involved mainly with refinement of crystal structures and therefore only the refinement stage of the structure solution process is discussed here.

Structure refinement is usually carried out using the Rietveld refinement technique [5]. The structure refinement stage requires a starting model which is already a sufficiently good representation of the true structure.

4.1.1a. The basis of the Rietveld refinement

The powder diffraction data include a numerical intensity value y_{io} which is recorded at each of the steps i . Since a starting model is available, the intensity y_{io} observed at the i th step may be compared with the corresponding intensity y_{ic} calculated via the model. Then the model can be refined by minimising by a least-squares process the sum of weighted residuals S_y :

$$S_y = \sum w_i (y_{io} - y_{ic})^2 \quad (4.1)$$

where w_i is a weight given by $w_i = 1/y_{io}$ (i.e. w_i is the inverse deviance of y_{io} in the case of Poisson statistics). The summation is over all data points.

The calculated intensity y_{ic} is a sum of the contributions from each K -th Bragg reflection and from the background:

$$y_{ic} = s \sum L_K |F_K|^2 G(2\theta_i - 2\theta_K) R_K A + y_{ib} \quad (4.2)$$

where s is the scale factor,

L_K contains the Lorentz, polarisation and multiplicity factors,

$2\theta_k$ is the peak position,

G is the reflection profile function,

R_K is the preferred orientation function,

A is the absorption factor,

F_K is the structure factor,

y_{ib} is the background intensity at the i th step.

The summation is over all the Bragg peaks contributing to y_{ic} .

The gradient least-squares minimisation procedure used in the Rietveld refinement may be outlined as follows.

The condition of minimum of the S_y function of M parameters P_k is represented by a set of M equations:

$$f_k = \partial S_y / \partial P_k = -2 \sum w_i (y_{io} - y_{ic}) (\partial y_{ic} / \partial y_{pk}) = 0, \quad k = 1, \dots, M \quad (4.3)$$

In the neighbourhood of the root (this is the reason why the gradient least-square process can be used only for refinement), each of the f_k functions can be expanded into Taylor series

$$f_k = (P + \Delta P) = f_k(P) + \sum (\partial f_k / \partial p_j) \Delta p_j + \bar{o}(\Delta P^2) \quad (4.4)$$

where the summation is over $j = 1, \dots, M$ and the last term in the right hand side of eq.(4.4) can be neglected. P is a vector given by the matrix

$$P = \begin{pmatrix} P_1 \\ \vdots \\ P_k \\ \vdots \\ P_M \end{pmatrix}$$

and ΔP is a similar vector of parameter increments.

Using (4.3) and (4.4) the following set of equations can be obtained:

$$\sum (\partial f_k / \partial p_j) \Delta p_j = -f_k(P) \quad (4.5)$$

where the summation is over $j = 1, \dots, M$.

The above set of equations can be solved for ΔP_j and a new vector P obtained through $P_{old} + \Delta P_j$. The procedure is reiterated until the minimum of S_y is found.

The parameters to adjust in the Rietveld refinement include unit cell constants, atomic positional and displacement parameters, and peak shape parameters defining the function G (eq.4.2). The list of refinable parameters in the course of the present work is given in table 4.1.

For each phase	Global
atomic coordinates, lattice parameters, isotropic displacement parameters, scale factor, peak width and asymmetry parameters, preferred orientation	instrumental profile, profile asymmetry, background,

Table 4.1. Refinable parameters in Rietveld refinement

The Rietveld refinement process will adjust the refineable parameters until the residual S_y is minimised in some sense. Two of the often used numerical criteria of fit are:

$$1) \quad \text{the weighted profile } R_{wp} = [\sum w_i (y_{io} - y_{ic})^2 / \sum w_i y_{io}^2]^{1/2} \quad (4.6)$$

$$2) \quad \text{the goodness of fit } GofF = \sum w_i (y_{io} - y_{ic})^2 / (N - P), \quad (4.7)$$

where N is the number of profile points and P is the number of refined parameters.

4.1.1b. Restraints and constraints in the Rietveld refinement

Powder diffraction data are a one-dimensional projection of three-dimensional diffraction data and hence they suffer from an inherent loss of information. One way to compensate for this loss is to incorporate additional observations or subsidiary relationships into the least-squares refinement process. These can be included as constraints (rigorous or hard constraints) or as restraints (soft or slack constraints). Constraints are imposed rigorously and the relationship specified must be exactly fulfilled. Examples of constraints are the symmetry constraints placed on atoms in special positions, or group constraints (e.g. rigid body model, where the distances and angles between atoms within a group are fixed and only the orientation of the group as a whole is refined).

Restraints are relationships which are imposed approximately and the degree of approximation is given by a finite weight. They are treated in the same way as a diffraction observation and thus the quantity minimised in the refinement is:

$$S_{yR} = S_y + c_w S_R \quad (4.8)$$

where S_y is defined as specified in eq.4.1. S_R can be represented as

$$S_R = \sum w(R_0 - R_c(x))^2 \quad (4.9)$$

where R_0 can be an expected distance, or angle, or other stereochemical quantity for which an expected value can be obtained, $R_c(x)$ is its value calculated from the atomic positions or other structural variables, and w is the inverse of the variance of the pseudo-observation.

c_w in eq.4.8 is a common weight factor which can be used to vary the contribution or influence of the restraints in the refinement process. In general, c_w is set high at the beginning of a

refinement when the structure is incomplete or approximately correct. It can be reduced as the refinement progresses until the restraints can be removed completely.

If used carefully, soft constraints can enhance the refinement considerably, especially in the case of complex structures. It is important that the final structural model fits both the geometric and X-ray (or neutron) data satisfactorily.

4.1.1c. Structural studies using neutron time-of-flight data

The complimentary relationship between X-ray and neutron data

The main difference between the X-ray and neutron data arises in the atomic scattering factor f which in turns is related to the structure factor F_K . X-rays are scattered almost only by the electrons, thus the region from which they are scattered is of the order of 10^5 larger than the typical size of nuclei from which the neutrons are scattered. As a result the X-ray scattering factor falls off dramatically over the range of $(\sin\theta)/\lambda$ in which observations can be made with the commonly used wavelengths in the range $0.5 - 2.5 \text{ \AA}$. The neutron scattering factors, however, do not fall off significantly over this range of observations, i.e. they are effectively constants. Nuclear scattering decreases mainly due to static and thermal displacements. Thus reflections at higher values of $\sin\theta/\lambda$ can be collected giving atomic positions and thermal parameters with better accuracy than with X-rays.

For neutrons, it is customary to use the scattering lengths b instead of f . The b values are different from the X-ray f in the following ways:

- a) there is no regular progression with the atomic number

- b) the b values can be positive, negative (i.e. phases can be shifted 180° on scattering), or complex numbers;
- c) all b values lie between $+1.5$ and -1.0 (in units of 10^{-12}cm)
- d) isotopes of the same element can have different b values. An important examples are ^1H and ^2D which have b values -0.38 and $+0.65$ ($\times 10^{-12}\text{cm}$) respectively.

Time-of-flight neutron diffraction techniques

In the time-of-flight neutron diffraction technique, neutrons are produced either by a pulsed reactor, or at accelerator spallation sources. High-energy protons in short pulses at the appropriate pulse frequency, strike a target such as uranium or tungsten releasing several tens of neutrons per proton. The pulsed neutron flux is present for a very short time (the burst lasts around $0.4\mu\text{s}$). High energy neutrons are slowed down to thermal energies by appropriate moderators. The width of the pulse leaving the moderator is roughly proportional to the wavelength, so that the fractional wavelength resolution is nearly constant.

For a pulsed neutron beam, the discrimination among neutrons with different wavelengths may be accomplished by their time of arrival at the detector (time of flight). In a time-of-flight diffractometer, detectors are located at fixed scattering angles and the diffraction pattern is recorded as a function of time delay from the start of a neutron burst at the source. The repetition frequency of the source in combination with the neutron flight path dictates the range of neutron wavelengths seen by the diffractometer, which in turns dictates the range of d -spacings accessible by a particular detector. The data for each detector are separately time encoded and these individual detector data are then combined into a single histogram by computing the flight times for each detector that corresponds to the same d -spacing and then combining the appropriate (constant d -spacing) time channels.

An individual detector will give diffraction peak widths that are essentially proportional to the reflection d -spacing. The resolution will vary from detector to detector as a function of the scattering angle. Because of the time structure of the neutron pulse from the source, the diffraction profiles are highly asymmetric.

4.1.2. RESULTS AND DISCUSSION

4.1.2a. Experimental details

X-ray powder diffraction data for structure refinement were collected on Stoe STADI/P diffractometer at room temperature in the range $5 < 2\theta < 60$, in 0.02° in 2θ steps, the entire runs lasting ~ 15 hours.

The neutron diffraction patterns were collected in 24h in the range of d -spacings from 1 to 10\AA on OSIRIS powder diffractometer at the ISIS pulsed spallation source, Rutherford Appleton Laboratory. $\text{PEO}_6\text{:LiPF}_6$ was prepared by the solvent casting method using fully deuterated PEO of molecular weight 28,400. $\text{PEO}_6\text{:LiSbF}_6$ was prepared by the same method using fully deuterated PEO of molecular weight 2,000. Each sample was placed in an air-tight cylindrical vanadium sample holder. In this Chapter, all complexes are referred to as normal (hydrogenated) complexes, although deuterated polymers have been used for the preparation in all cases of structure refinement with neutron diffraction data.

As discussed in Chapter 2, the use of polymers of different molecular weight does not influence the crystal structures, and the same crystalline complexes are obtained for a range of

molecular weights from 1,000 to 100,000. However, the degree of crystallinity is higher at the low molecular weight complexes and therefore the latter are used in the structural studies.

Since the samples have been prepared with fully deuterated polymers, the atoms in the polymer chain have significant contribution to the neutron diffraction pattern due to the larger scattering length of ^2D compared to ^1H . It should be noted that normal hydrogenated polymer will produce enormous incoherent background in the diffraction pattern. Therefore it is important to use polymer samples in which the hydrogen atoms are completely substituted by deuterium.

Structure refinements were based on the Rietveld method [5] using the GSAS program package [6].

4.1.2b. Structure refinement of $\text{PEO}_6\text{:LiPF}_6$ and $\text{PEO}_6\text{:LiSbF}_6$ using neutron TOF data

Rietveld refinement

Careful inspection of the data shows that the neutron diffraction patterns of the complexes $\text{PEO}_6\text{:LiPF}_6$ and $\text{PEO}_6\text{:LiSbF}_6$ (fig.4.1) are very similar to that of $\text{PEO}_6\text{:LiAsF}_6$ [7] in terms of peak positions. This suggests that the complexes are isostructural and therefore the crystal structure of the complex $\text{PEO}_6\text{:LiAsF}_6$ can be used as a starting model for Rietveld refinement of the complexes $\text{PEO}_6\text{:LiPF}_6$ and $\text{PEO}_6\text{:LiSbF}_6$.

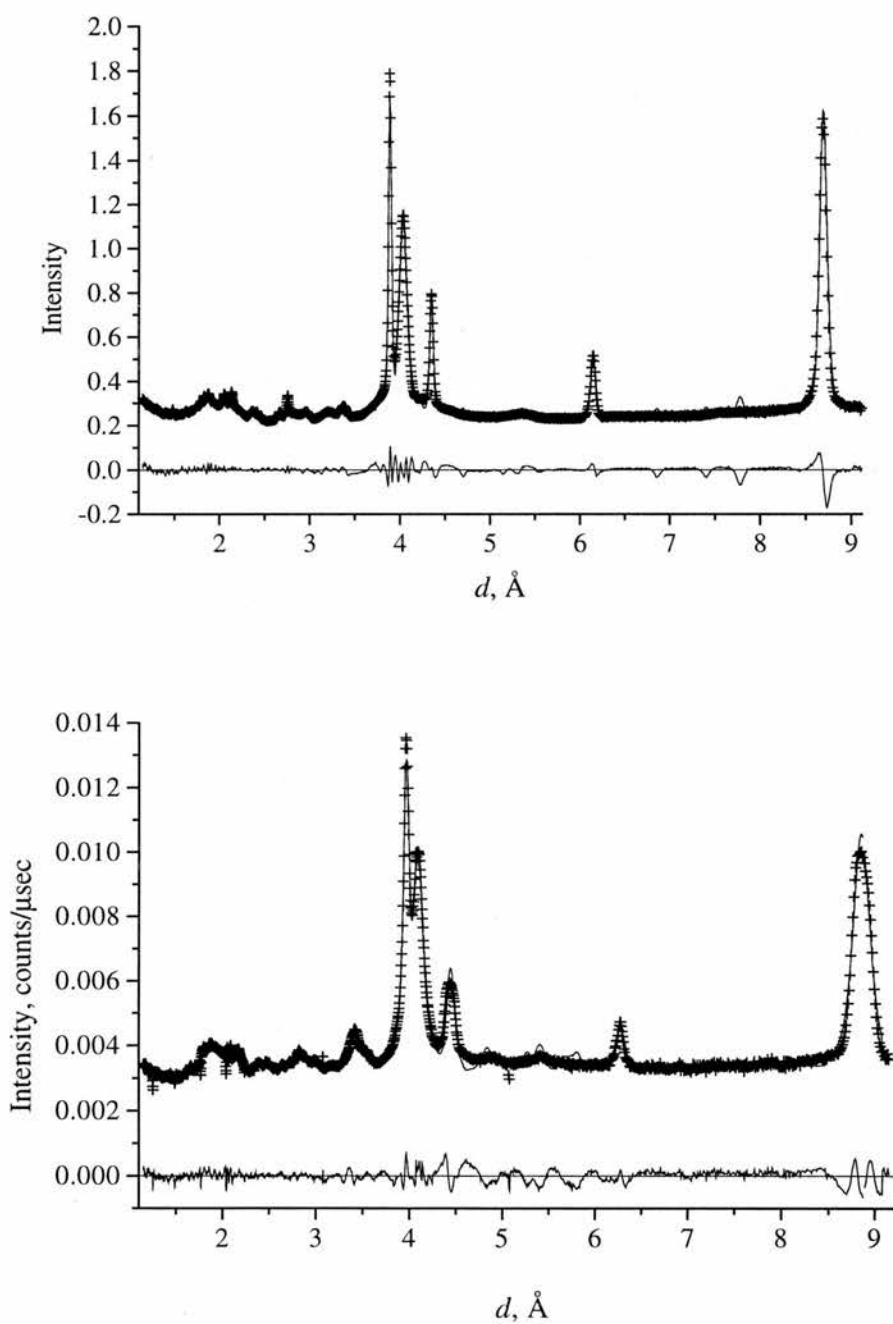


Fig.4.1. Final observed (crosses), calculated (line) and difference profiles (below) for the Rietveld refinement of $\text{PEO}_6\text{:LiPF}_6$ (top figure) and $\text{PEO}_6\text{:LiSbF}_6$ (figure below)

The refinements involved 1734 data points, 800 reflections, 50 atoms in the asymmetric unit, 162 variables and 135 soft constraints. It is shown in section 4.1.1c that the use of soft constraints in the Rietveld method can be of particular importance for the refinement of complex structures. The introduction of soft constraints in the present work aimed at increasing the number of observations, thus allowing more parameters to be refined. In addition, the geometry of the structural model could be kept sensible. The use of soft constraints proved to be of crucial importance for the convergence of the structure refinement procedure. When less constrained models were used, the refinement diverged and unreasonable values for bond lengths, angles or interatomic distances were obtained. The following soft constraints were used throughout the refinements: C-O bonds 1.430 Å, C-C bonds 1.550 Å, P-F bonds 1.550 Å, Sb – F bonds 1.82 Å, C-O-C angles 109°. These values were taken from previous structural studies of similar compounds [7-19]. Displacement parameters were constrained to be equal for all atoms in the chain. The same assumption was made for the atoms of the anions.

The final refinement structures yielded good fits to the experimental data (fig.4.1) with $R_{wp} = 0.042$ for $PEO_6:LiPF_6$ and $R_{wp} = 0.035$ for $PEO_6:LiSbF_6$. Unit cell parameters obtained after the refinement are listed in table 4.2. The atomic coordinates, atomic displacement factors and selected interatomic distances are presented in Appendix I and Appendix II.

	PEO ₆ :LiPF ₆	PEO ₆ :LiAsF ₆	PEO ₆ :LiSbF ₆
Space group	P2 ₁ /a	P2 ₁ /a	P2 ₁ /a
a, Å	11.723(4)	11.871(4)	12.01(1)
b, Å	17.375(4)	17.537(3)	17.787(9)
c, Å	9.131(2)	9.227(3)	9.296(4)
β	107.80(2)	108.21(1)	107.91(2)
Unit cell volume, Å ³	1770.27	1824.69	1889.92

Table 4.2. Unit cell parameters for the complexes PEO₆:LiXF₆ (X = P, As, Sb)

Discussion of the crystal structures

The structures of $\text{PEO}_6\text{:LiPF}_6$ and $\text{PEO}_6\text{:LiSbF}_6$ are similar to that of the $\text{PEO}_6\text{:LiAsF}_6$ (fig.4.2). As in the hexafluoroarsenate complex the Li^+ cations are arranged in rows with each row located along the axis of an axisymmetric surface formed by two PEO chains. The surface approximates to a cylinder in the case of $\text{PEO}_6\text{:LiPF}_6$ but in the case of $\text{PEO}_6\text{:LiSbF}_6$ it may be better described as a right parallelepiped. Each chain adopts a conformation $ct \bar{g} \bar{g} tt \bar{g} ctgtt \bar{g} \bar{g} g \bar{g} ct$ in $\text{PEO}_6\text{:LiPF}_6$ and $\bar{g} \bar{g} tcttcctgttc \bar{g} g \bar{g} \bar{g} t$ in $\text{PEO}_6\text{:LiSbF}_6$, compared to $ctg \bar{g} tgc \bar{g} tcttgt \bar{g} cgt$ in $\text{PEO}_6\text{:LiAsF}_6$, which defines either a half-cylinder (PF_6^- complex) or a half-right-parallelepiped (SbF_6^-) with the two halves (PEO chains) in each case interlocking on both sides. The above conformational sequences have been derived assuming that torsion angles in the range $0\pm 45^\circ$ are *cis* (c), $180\pm 45^\circ$ are *trans* (t), the remainder are either *gauche* (g) or *gauche-minus* (\bar{g}).

The cations are coordinated by both chains, involving 3 ether oxygens from one and 2 from the other with Li-O distances in the range of 2.14-2.19 Å. In both complexes the third ether oxygen from the second chain is located over 3 Å away from the Li^+ ion and is not involved in the coordination of the cation. There are two Li-Li distances along the chain axis and these are 7.4 and 4.4 Å for $\text{PEO}_6\text{:LiPF}_6$, 6.5 and 5.4 Å for $\text{PEO}_6\text{:LiAsF}_6$ and 7.1 and 5.0 Å for $\text{PEO}_6\text{:LiSbF}_6$. The separation of Li^+ ions between neighbouring chains is 9.1, 9.2 and 9.3 Å for the three complexes in order of ascending anion size. The PF_6^- and SbF_6^- anions do not coordinate the cations (all Li-F distances are greater than 4.5 Å) and, like the anions in the structure of $\text{PEO}_6\text{:LiAsF}_6$, are located in the interchain space.

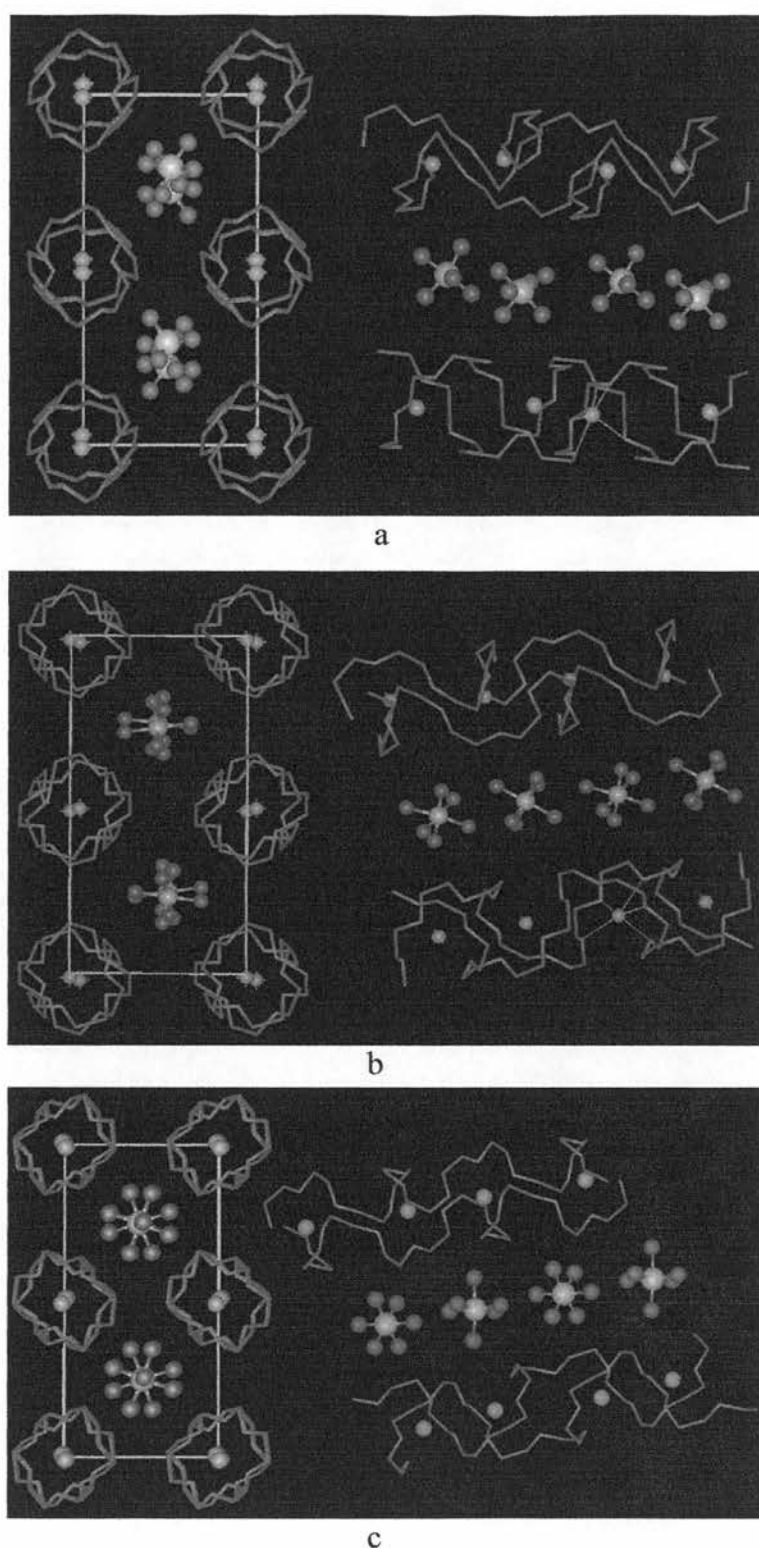


Fig.4.2. The structures of: a) $\text{PEO}_6:\text{LiPF}_6$, b) $\text{PEO}_6:\text{LiAsF}_6$, c) $\text{PEO}_6:\text{LiSbF}_6$. Left, view of the structure along the axis a showing rows of Li^+ ions perpendicular to the page. Right, view of the structure showing the relative position of the chains and their conformation (hydrogens not shown). Thin lines indicate coordination around the Li^+ cation. Blue spheres - lithium; white spheres - P, As or Sb; magenta - fluorine; green - carbon; red - oxygen.

The structures of all three 6:1 complexes ($\text{PEO}_6\text{:LiXF}_6$, $X = \text{P, As, Sb}$) possess similar features but there are some differences which arise from the increasing anion size. The volume of the anion rises by 25% on replacing PF_6^- by AsF_6^- and by a further 29% on substituting AsF_6^- by SbF_6^- . The increase in anion size has the effect of pushing apart the columns formed by the pairs of PEO chains and this is reflected in the increase of the b and c lattice parameters (table 4.2). a also increases resulting in a rise in unit cell volume and, in addition, the PEO columns become stretched along their columnar axis. Despite this the average Li-O bond length and the coordination number around Li^+ remain the same. It is likely that the conformational changes that occur in the PEO chains on replacing PF_6^- by AsF_6^- and SbF_6^- arise because of the need to accommodate the dimensional changes of the anion while maintaining the strong cation-ether oxygen coordination.

The change in the PEO conformation from cylindrical columns around Li^+ in $\text{PEO}_6\text{:LiPF}_6$ to the rectangular cross-section of the right parallelepiped in $\text{PEO}_6\text{:LiSbF}_6$ has the effect of increasing the size of the cavity available for the anion. As a result the separation of the PEO columns does not increase as much as would be anticipated in the absence of such a conformational change. This is reflected in the fact that the unit cell does not expand in proportion to the increase in the anion size.

The degree of disorder in the structures decreases as the anion size increases. The Li^+ and XF_6^- ions together form a zig-zag arrangement along the a -axis in the $\text{PEO}_6\text{:LiPF}_6$ complex. This arrangement becomes more linear as the anion size increases. The anions, especially in $\text{PEO}_6\text{:LiSbF}_6$, are almost eclipsed when viewed along a .

Bond lengths and angles within the chains and the anions lie in the range of the previously reported values.

4.2. Powder X-ray diffraction applied for studies of physical properties (particle sizes) of crystalline complexes

The present work was involved with studies of crystalline complexes of various molecular weights (ranging from 1,000 up to 100,000). As already discussed in Chapter 2, the variation of the molecular weight in the range 1,000 – 100,000 did not effect the crystal structures of the crystalline complexes; all complexes of the same chemical composition, but differing in the molecular weight only were isostructural.

While the use of different molecular weight polymer ($M_w = 1,000 \div 100,000$) did not effect the structures of the crystalline complexes, significant differences were observed in the degree of crystallinity (in terms of peak-to-background ratio and peak widths). This section deals mainly with the crystallite size broadening effects in the complexes of different molecular weight and some conclusions are made concerning the crystallite sizes of the complexes under study.

4.2.1. Effect of crystal size on the powder pattern – particle size measurements

The size of the individual crystals in a polycrystalline sample is important information related to crystal growth conditions and to mechanical properties. The powder diffraction method provides a simple way of measuring the mean crystallite size of a specimen taking into account the broadening of the diffraction lines which occurs in the case of small particle sizes (below $\sim 2000\text{\AA}$) [20, 21, 22].

In the absence of broadening due to small particle size, powder diffraction lines have a finite breadth for several reasons: *i)* the radiation is not absolutely monochromatic, *ii)* the $K\alpha$ line has an intrinsic breadth due to the Heisenberg uncertainty principle and *iii)* normally, the focussing geometry of the instrument is not perfect.

The observed peak shape $h(\theta)$ in a powder diffraction experiment is an integral convolution of the physical peak shape $f(\theta)$ (arising from the small crystallite size) and instrumental broadening $g(\theta)$:

$$h(\theta) = \int f(\theta') \cdot g(\theta - \theta') d\theta' \quad (4.10)$$

The solution of eq.(4.10) is a challenging mathematical problem due to the incorrectness of the solution which in its turn is caused by statistical errors in $h(\theta)$.

The commonly accepted formula for particle size broadening is the Scherrer formula:

$$t = K\lambda/B\cos\theta_B \quad (4.11)$$

where t is the size of the crystallite (in angstroms), λ is the X-ray wavelength, B is the line broadening (full width at half maximum of $f(\theta)$), K is a constant close to unity and θ_B is the Bragg angle. The line broadening B is measured from the extra peak width at half the peak height and is obtained from the formula

$$B^2 = B_M^2 - B_S^2 \quad (4.12)$$

where B_M is the measured peak width in radians at half peak height. B_S is the full width at half maximum of $g(\theta)$ and therefore it is related to the instrumental broadening. B_S can be determined from the corresponding width of a peak of a standard specimen made from a well-crystallised material without size effects such as quartz SiO_2 or alumina Al_2O_3 . The particle size for the standard should be considerably greater than 2000\AA and there should be a diffraction peak near to the relevant peak of the sample.

It is evident from equation (4.11) that the crystallite size broadening is inversely proportional to $\cos\theta_B$; for other causes of line-broadening the relation is different. Therefore, if the line-broadening is found to be proportional to $\cos\theta_B$ for a particular substance, it can be assumed that the broadening is due to the small size of the crystals.

Strictly speaking, the above discussion is valid when the particles belong to the cubic system and are uniform in size. In general, the breadths of different reflections depend on the dimensions of the crystals in different directions and on the indices. Therefore the breadths of different lines do not vary regularly with the Bragg angle. In addition, the relation (4.11) implies the absence of any other peak-widening effects which can be due to microstrains or packing faults, or to peak overlap. However, it is usually agreed that equation (4.11) can be used quite generally without risk of serious error.

It should be noted that the line broadening gives no information on the size distribution among the crystals responsible for the effect since it indicates only an average size.

4.2.2. Estimation of crystallite size – experimental results

Crystallite size broadening effects were examined for the complexes $\text{PEO}_6\text{:LiPF}_6$ and $\text{PEO}_6\text{:LiSbF}_6$ which were prepared with polymers of different molecular weights. Alumina and Si were used as standard materials to measure peak broadening. These materials do not have diffraction peaks at low 2θ angles (near the peaks of the samples), and the value of B_s was obtained by extrapolation of the data at higher 2θ angles as suggested in reference [21]. Detailed analysis of the polymer electrolyte samples was not carried out due to the small number of peaks in the X-ray diffraction patterns of the complexes under study. Furthermore, most of these peaks

consisted of two or more overlapping reflections and no attempts were made to deconvolute these composite peaks into their individual components. The only well-resolved single reflection in the powder patterns was the reflection 021 and this reflection was used to estimate the crystallite size of the samples. The calculated values are listed in table 4.3.

The data in table 4.3 indicate that there is significant increase of the crystallite size for the samples of low molecular weight, particularly for the samples of molecular weight $M_w = 1,000$. The calculations show that the crystal structure in this case is coherent on a length scale of $1000 \pm 2000 \text{ \AA}$. Some variations in B_M were observed for different samples of the same molecular weight. The numbers in brackets in table 4.3 show the corresponding variations of the particle size. Irrespective of these variations, however, it is clear that the crystallite size increases continuously with reducing the molecular weight of the complex.

It should be noted that the above estimation of crystallite size is based on the assumption that peak broadening is due to particle size effects only. Because of the limited data in the X-ray diffraction patterns, it has been impossible to discriminate among all other possible causes of broadening, such as variation of lattice dimensions, existence of structural irregularities in the crystals. Therefore the data in table 4.4 should be used to gain only a general idea of the size of the crystals. For more precise particle size estimation, it may be necessary to use other relevant techniques, e.g. electron microscopy, etc. which can provide supplementary data for performing more detailed and accurate analysis.

Sample	Molecular weight	Estimated particle size, Å
PEG ₆ :LiPF ₆	1,000	1500 (±500)
PEG ₆ :LiPF ₆	2,000	750 (±60)
PEO ₆ :LiPF ₆	100,000	500 (±60)
PEG ₆ :LiSbF ₆	1,000	1500 (±500)
PEG ₆ :LiSbF ₆	2,000	650 (±60)
PEO ₆ :LiSBF ₆	100,000	500 (±60)
$B_S = 0.00174rad, K = 0.9$		
$\lambda = 1.54 \text{ Å}$		
$\theta_B = 7.2^\circ$ (LiPF ₆ complex) $\theta_B = 7.08^\circ$ (LiSbF ₆ complex)		

Table 4.3. Estimated particle sizes for the complexes PEO₆:LiXF₆ (X = P, Sb) of different molecular weights

4.3. CONCLUSIONS

Crystal structures of the stoichiometric 6:1 complexes

The crystal structure studies demonstrate that all stoichiometric crystalline complexes $\text{PEO}_6:\text{LiXF}_6$ ($X = \text{P, As, Sb}$) are isostructural. Their structures differ markedly from the previously known structures of 3:1, 4:1 and 1:1 crystalline stoichiometric complexes. In the 6:1 complexes, the Li ions are located within tunnels formed by pairs of interlocking polymer chains. Thus Li ions are coordinated to the oxygen atoms in the polymer chains only but not to the anions which is in contrast to the structures of the other stoichiometric complexes of compositions 3:1, 4:1 or 1:1. The structures of the 6:1 complexes are distinctive since they provide permanent pathways which may permit significant ion transport.

Influence of the molecular weight

The examination of 6:1 complexes of different molecular weight (ranging from 1,000 to 100,000) demonstrates that the crystal structures are the same when the molecular weight is varied in the above range. The fact that the crystal structures are preserved has important consequences since the properties of samples of different molecular weight can be directly compared. In addition, it has been shown that the physical (mechanical) properties of the samples can be significantly improved by varying the molecular weight. Therefore, the properties and processes in high-quality crystalline samples can be studied, and the results can be extrapolated in order to make more general conclusions.

4.4. REFERENCES

1. R.A.Young, *The Rietveld Method*, Oxford University Press, 1993
2. C.Giacovazzo, *Fundamentals of Crystallography*, Oxford University Press, 1992
3. L.B.McCusker, R.B.VonDreele, D.E.Cox, D.Louer and P.Scardi, *J.Appl.Cryst.*, **32**, 36 (1999)
4. R.B.VonDreele, J.D.Jorgensen and C.G.Windsor, *J.Appl.Cryst.*, **15**, 581 (1982)
5. H.M.Rietveld, *J.Appl.Crystallogr.*, **2**, 65 (1969)
6. A.C.Larson and R.B.VonDreele, Los Alamos National Laboratory Report NoLA-UR-86-748 (1987)
7. G.MacGlashan, Y.Andreev and P.G.Bruce, *Nature*, **398**, 792 (1999)
8. P.G.Bruce, *Electrochim.acta*, **40**, 2077 (1995)
9. P.Lightfoot, M.A.Mehta and P.G.Bruce, *Science*, **262**, 883 (1993)
10. P.Lightfoot, M.A.Mehta and P.G.Bruce, *J.Mater.Chem.*, **2**(4), 379 (1992)
11. P.Lightfoot, J.L.Nowinski and P.G.Bruce, *J.Amer.Chem.Soc.*, **116**, 7469 (1994)
12. Y.Chatani and S.Okamura, *Polymer*, **28**, 1815 (1987)
13. Y.G.Andreev, P.Lightfoot and P.G.Bruce, *Chem.Comm.*, 2169 (1996)
14. Y.Chatani, Y.Fujii, T.Takayanagi and A.Honma, *Polymer*, **331**, 2238 (1990)
15. J.B.Thomson, P.Lightfoot and P.G.Bruce, *Solid State Ionics*, **85**, 203 (1996)
16. Y.Andreev, G.MacGlashan and P.G.Bruce, *Phys.Review B*, **55**, No18, 12011
17. R.Iwamoto, Y.Saito, H.Ishihara and H.Tadokoro, *J.Polymer Sci.,A-2*, **6**, 1509 (1968)
18. Y.G.Andreev, P.Lighthfoot and P.G.Bruce, *J.Appl.Cryst.*, **30**, 294 (1997)
19. P.G.Bruce and Y.Andreev, *J.Chem.Soc.-Dalton Trans.*, **24**, 4071 (1998)
20. J.P.Eberhart, *Structural and Chemical Analysis of Materials*, J.Willey&Sons, 1991

21. C.W.Bunn, *Chemical Crystlography*, Oxford University Press, 1945
22. A.West, *Solid State Chemistry and Its Applications*, J.Wiley&Sons, 1984

CHAPTER 5

CONDUCTIVITY STUDIES

5.1. GENERAL CONSIDERATIONS

In general, the basic electrical properties of polymer electrolytes are characterised by the following [1, 2]:

- variation of the total conductivity as a function of temperature
- charged species which contribute to conduction
- proportion of the current carried by each charged species as a function of temperature.

The total conductivity σ is the sum of electronic, σ_{el} , and ionic, σ_i , contributions:

$$\sigma = \sigma_{el} + \sigma_i \quad (5.1)$$

Normally polymer electrolytes exhibit low electronic conductivity and their total conductivity is determined mainly by the ionic contribution σ_i [1, 2].

The ionic conductivity can be treated as the product

$$\sigma_i = c_i q u_i \quad (5.2)$$

where c_i is the concentration of the mobile species, q is their charge, and u_i is their mobility. However, the quantitative application of eq.(5.2) is very difficult since it is difficult to obtain independent estimates of c_i and u_i . In favourable circumstances, it is possible to measure directly diffusion coefficients and mobilities by the pulse field gradient NMR method, or radiotracer techniques [3].

For polymer electrolytes, three types of temperature dependence of ionic conduction have been observed according to the nature of the salt and its concentration [4]. For electrolytes with high degree of crystallinity, this dependence is described by an Arrhenius type relation

$$\sigma_i = A \exp(-E_a/RT) \quad (5.3)$$

where A is a pre-exponential factor and E_a is an activation energy. A and E_a are related to the number of charge carriers and their mobility. In some cases, discontinuity is observed in the $\log(\sigma_i)$ vs. $1/T$ curve and then eq.(5.3) applies to each segment.

For an amorphous electrolyte, the Vogel – Tamman – Fulcher (VTF) equation provides a better description

$$\sigma_i = A \exp[-B/R(T-T_0)] \quad (5.4)$$

where the pre-exponential factor A is proportional to $T^{1/2}$ and T_0 is a reference temperature which can be associated with the glass transition temperature of the electrolyte. The constant B divided by the gas constant is not related to any simple activation process although B has the dimensions of energy.

The third type of temperature dependence is a combination of the first two, i.e. an Arrhenius type for the temperatures below the transition temperature and a VTF for higher values.

This is a phenomenological classification of the polymer electrolytes and the above equations do not yield to the mechanisms governing ionic conductivity, although analysis of the characteristic parameters (E_a , T_0 and A) obtained from these equations can serve as a basis for formulating assumptions [5, 6].

The variations of the ionic conductivity measured as a function of temperature usually depend on the experimental conditions, such as the presence of residual water [7], heating and cooling rates and the thermal history of the samples. Lack of control over these parameters may result in contradictory and confusing results which do not represent the intrinsic ionic conductivity properties.

5.2. ALTERNATING CURRENT MEASUREMENTS WITH BLOCKING ELECTRODES

Alternating current measurements with blocking electrodes are the most popular method for characterisation of the electric properties of polymer electrolytes. This is mainly because very simple cells incorporating inert blocking electrodes may be used to determine bulk electrolyte properties.

In the alternating current (a.c.) experiment, a sinusoidal voltage is applied to the cell and the sinusoidal current passing through the cell as a result of this perturbation is determined. Two parameters are required to relate the current to the applied potential; one is analogous to the resistance in direct current measurements and is equal to the ratio of the

voltage and current maxima V_{max}/I_{max} ; the other parameter is the phase difference θ between the voltage and current. The combination of these parameters is the impedance Z of the cell. For an electrochemical cell, both the magnitude of the impedance $|Z| = V_{max}/I_{max}$ and its phase angle θ are functions of the applied frequency, thus it is possible to extract information about the different electrical properties of the cell. Interpreting the results of an a.c. experiment relies on considering the possible electrical processes, describing them as an equivalent circuit and fitting it to the experimental data.

5.2.1. Experimental details

The a.c. impedance measurements were made using a Solartron 1255 frequency response analyser coupled to a Solartron 1286/1287 potentiostat and driven by a PC under software control. The measurements were performed over the frequency range 0.1Hz to 100kHz at various temperatures.

The impedance measurements were carried out in two-electrode, one compartment PTFE cell. The polymer electrolyte disks were mounted between two parallel stainless steel disk electrodes, which were polished with alumina suspended in water before each measurement cycle. The cell was dried and then assembled and located within an evacuable stainless steel can with electrical feedthroughs and a thermocouple. All manipulations prior to the conductivity measurements were performed in dry Ar-filled glove box.

For variable temperature a.c. measurements, the can was placed in either a Buchi oven B-580 or Si-oil bath. The temperature was controlled by the thermocouple located near the sample. Prior to each measurement, the sample was kept at a given temperature for sufficient time to attain thermal equilibrium.

Polymer electrolyte disks suitable for loading into the cells were obtained by cold pressing of powder samples. The resulting pellets had very smooth surfaces. In some cases the electrolyte disks were coated with Ag paste or sputtered Au to ensure good contact with the

electrodes. These tests gave the same results as compared to the tests without coating on the samples. This confirmed that the electrical contact between the samples and the electrodes was sufficiently good to produce reliable data. It should be noted that, though brittle, the electrolyte samples (particularly the low-molecular weight ones) were sticky and resembled in appearance organic molecular crystals. It is possible that for this reason the experiments with or without coatings gave the same results in contrast, for example, to the inorganic ceramic electrolytes.

Conductivity values were extracted from the complex impedance plots. The conductance $G = 1/R$ was calculated on the basis of the measured resistance R from the low-frequency intercept of the semicircle associated with the bulk response. The conductivity was then obtained taking into account the cell constant (l/a):

$$\sigma = G(l/a), \quad (5.5)$$

where l is the thickness of the polymer electrolyte sample, and a is the surface area of one electrode.

5.2.2. Analysis of complex impedance plots and equivalent circuits

Typical impedance plots obtained in the course of this work are shown in fig.5.1 and 5.2. The impedance plots represent the behaviour of a pure ionic conductor with both bulk and electrode contributions. The semicircle in the high-frequency region can be associated with the bulk response of the electrolyte whereas the spike in the low-frequency region can be associated with the electrode-electrolyte interface.

The physical processes which occur in the cell are: migration of ions which can be represented by a resistor R_b and dielectric polarisation of the polymer chains which can be represented by a capacitor C_b . The ion migration and bulk polarisation are physical processes which occur in parallel and thus the corresponding components R_b and C_b are connected in parallel.

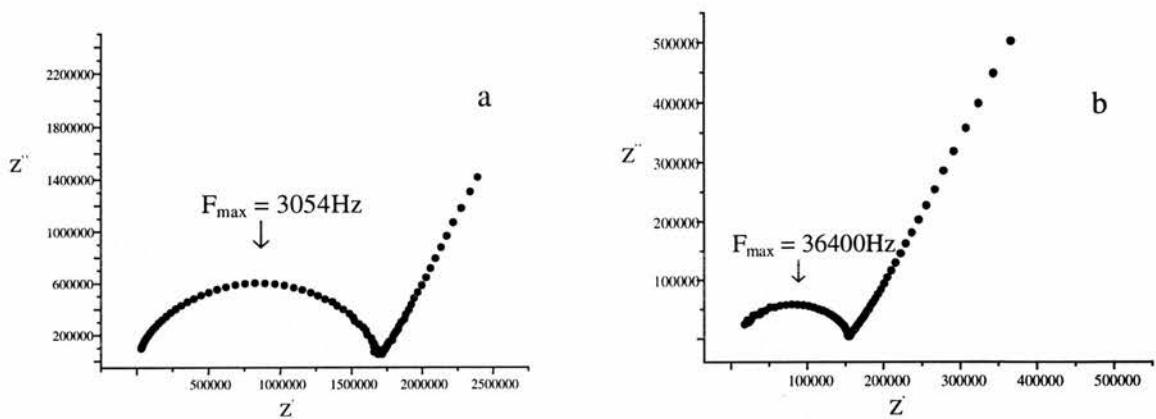


Fig.5.1. Complex impedance plots for the crystalline complex $PEG_6:LiSbF_6$ ($M_w = 2,000$) at different temperatures:
a) $22^\circ C$, frequency range $100,000 - 0.1 Hz$
b) $43^\circ C$, frequency range $300,000 - 0.1 Hz$

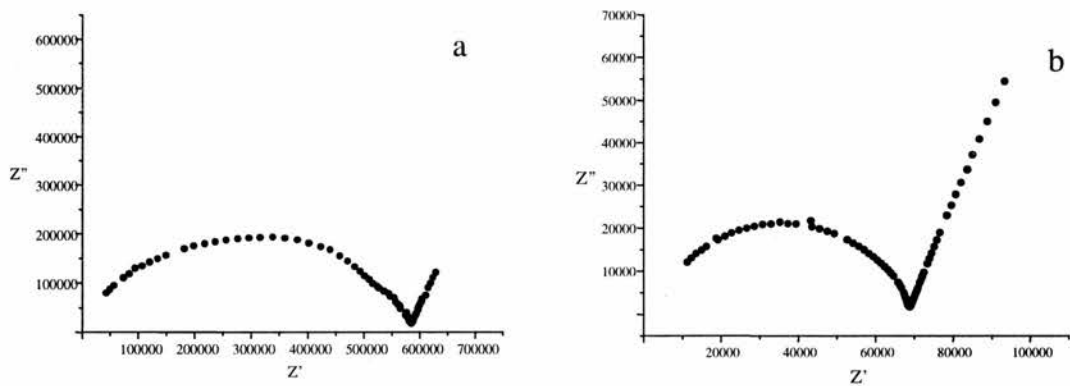


Fig.5.2. Complex impedance plots for the amorphous complex $PEO_6:LiSbF_6$: a) $50^\circ C$, frequency range $1 - 70,000 Hz$;
b) $72^\circ C$, frequency range $1 - 400,000 Hz$

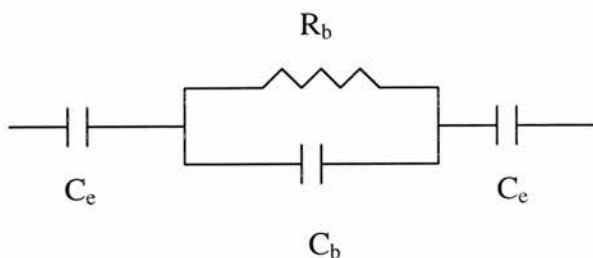


Fig.5.3. Equivalent circuit for the a.c. response shown in fig.5.1 and 5.2.

In the alternating field, ionic charge builds up within the electrolyte near the electrodes and these charges are balanced by an equal but opposite electronic charge on the electrodes. Thus each electrode can be represented by a capacitance C_e which is connected in series with the parallel combination of R_b and C_b . Since the electrodes in the cell under study are identical, they can be represented by one capacitor which represents the overall electrode response: $1/C_e = 1/C_{e1} + 1/C_{e2}$. It should be noted that the representation of the electrolyte/electrode interface as a double-layer capacitance is a reasonable approximation when the ionic concentration within the electrolyte is high, $\geq 1M$ [1]. Then the ionic charge required to balance the electronic charge on the electrode is concentrated onto one plane near the electrode surface. The polymer electrolytes in this work have high ionic concentration and therefore the above approximation is acceptable.

Therefore, the impedance data in fig.5.1 can be modelled by equivalent circuit consisting of resistor R_b and capacitor C_b which are connected in parallel and both are in series with capacitance C_e (fig.5.3).

At high frequencies, the impedance of the bulk resistance and capacitance are of the same magnitude whereas the impedance of the electrode capacitance C_e is insignificant. Therefore the equivalent circuit can be reduced to a parallel combination $R_b C_b$ which gives rise to a semicircle in the complex impedance plot. The high-frequency region provides information about the properties of the electrolyte, e.g. the bulk capacitance C_b can be

determined using the relation $w_{max}R_bC_b = 1$ which holds at the maximum of an ideal semicircle (w is the angular frequency). The calculated capacitance C_b in this work was of the order of $1.5 \times 10^{-12} \text{F}$ at all temperatures. This is a typical value for the bulk capacitance.

At low frequencies, the impedance of the bulk capacitance is negligible and the equivalent circuit can be reduced to a series combination of R_b and C_e . This gives rise to the vertical spike in the complex impedance plot.

It can be seen (fig.5.1 and 5.2) that the semicircles in the impedance plots are depressed or distorted (for the amorphous complex $\text{PEO}_6:\text{LiSbF}_6$) and the spike is tilted (for both the crystalline and amorphous complexes). These deviations are very pronounced for the amorphous complex in the temperature range $40\text{-}65^\circ\text{C}$ in which case two superimposed semicircles are observed in the high-frequency region of the a.c. plots (fig.5.2a). The inspection of the impedance plots at different temperatures shows that the angle of the spike to the horizontal tends towards 68° for the amorphous complex $\text{PEO}_6:\text{LiSbF}_6$ and 60° for the crystalline complexes $\text{PEG}_6:\text{LiPF}_6$ and $\text{PEG}_6:\text{LiSbF}_6$ of $M_w = 1,000$.

Distorted semicircles and non-vertical spikes are common observations in studies of polymer electrolyte and other ionically conducting materials [1, 2, 8, 9]. Taking into account the polymer electrolytes in the present work and the electrochemical cell as a whole (i.e. the use of blocking electrodes in symmetrical cell) it is possible to consider several causes for the non-ideal behaviour of the impedance plots. First, distorted or depressed semicircles can be due to inhomogeneities in the samples, e.g. the presence of two phases (crystalline and amorphous material). Alternatively, inhomogeneities may be due to granular nature of the samples, in which case the electrolyte separates into a mosaic of individual grains in contact with each other at the grain boundaries. In the case of such polycrystalline materials, the overall a.c. response depends on the bulk properties of all individual grains or crystallites. Because of differing grain sizes and orientations, the bulk semicircle at the high-frequencies may be displaced downward so that its center lies below the real axis. It should be noted that distorted semicircles were observed mainly in the case of the amorphous complex

PEO₆:LiSbF₆ and the high molecular weight crystalline complexes. The deviations from the ideal semicircles were less pronounced in the a.c. response of the highly crystalline low molecular weight complexes. This may indicate that the a.c. response of the amorphous and high molecular weight crystalline complexes is determined by the occurrence of two or more different physical processes (e.g. ionic conduction in different phases) which have similar pertinent time constants and therefore are not well separated in frequency.

Second, the deviation of the spike from the vertical line can be due to rough electrodes, specific adsorption, large differences between the mobilities of mobile positive and negative species [9]. In practice, it is often difficult to distinguish between a rough surface and incomplete blocking (electrode reaction). A rough surface, for example, may enhance electron transfer at the electrode, and thus the probability of electrode reaction is increasing. In addition, it has been demonstrated in [10] that even when complete blocking can be assured, the larger the ratio of mobilities of positive/negative charges, the larger the departure from verticality. As already pointed out, the deviations from the ideal 90° spike were more pronounced in the case of the crystalline complexes as compared to the amorphous complex PEO₆:LiSbF₆. At the same time, for both materials, the angle between the spike and the real axis was the same at all temperatures (within experimental errors). This implies that the deviations from the ideal 90° vertical are not related in a simple way to a thermally activated process. In particular, for the amorphous complex PEO₆:LiSbF₆ one would expect the spike to tend to the ideal 90° at higher temperatures due to increase of the free volume and the formation of more ideal double layer capacitance.

Third, non-ideality of the impedance plots can arise from ion pairing (ion associations). The contribution of ion-ion interactions is expected to be negligible, particularly for the crystalline complexes of composition 6:1. For these complexes, the NMR studies indicate that no detectable ion-ion interactions occur in the temperature range under study (as discussed in Chapter 6). However, the a.c. response of the amorphous complex PEO₆:LiSbF₆ could be significantly influenced by ion pair formation. The NMR data in this

case suggest that in the temperature range 25 – 50°C significant fraction of ions is present as ion pairs or larger clusters. The ion pairs are a form of electric dipole which may orientate in an electric field [1] and at low frequencies this will increase the dielectric constant and therefore the bulk capacitance. At high frequencies, the dipoles no longer contribute to the bulk capacitance. Therefore, the equivalent circuit for the electrolytes (fig.5.3) will include some additional components – a capacitor C_p (representing the contribution of the dipoles to the low-frequency dielectric constant) and a resistor R_p (representing their relaxation). The overall bulk impedance then consists of two semicircles representing the conduction and polarisation processes. Also, there could be a distribution of dielectric relaxation times and this will result in broadening of the semicircles in the complex impedance plots.

5.2.3. Analysis of conductivity data

5.2.3a. Temperature dependence of total ionic conductivity

The temperature dependence of total ionic conductivity was studied for the following systems: $\text{PEO}_6:\text{LiPF}_6$, $\text{PEO}_x:\text{LiAsF}_6$ ($x = 3, 6$ and 20) and $\text{PEO}_6:\text{LiSbF}_6$. (fig.5.4). The ionic conductivity of these polymer electrolytes was found to depend on the molecular weight of the polymer, degree of crystallinity and composition of the complexes.

Taking into account the poor thermal stability of some of the above systems (as discussed in Chapter 3), the conductivity measurements were performed in suitable temperature ranges in order to avoid thermal decomposition of the samples. In addition, each sample was examined by XRD before and after each measurement cycle to ensure that the obtained conductivity values were true representation of the electrical properties of the system under test. The conductivity of the amorphous complex $\text{PEO}_6:\text{LiSbF}_6$ was measured at temperatures above its glass transition.

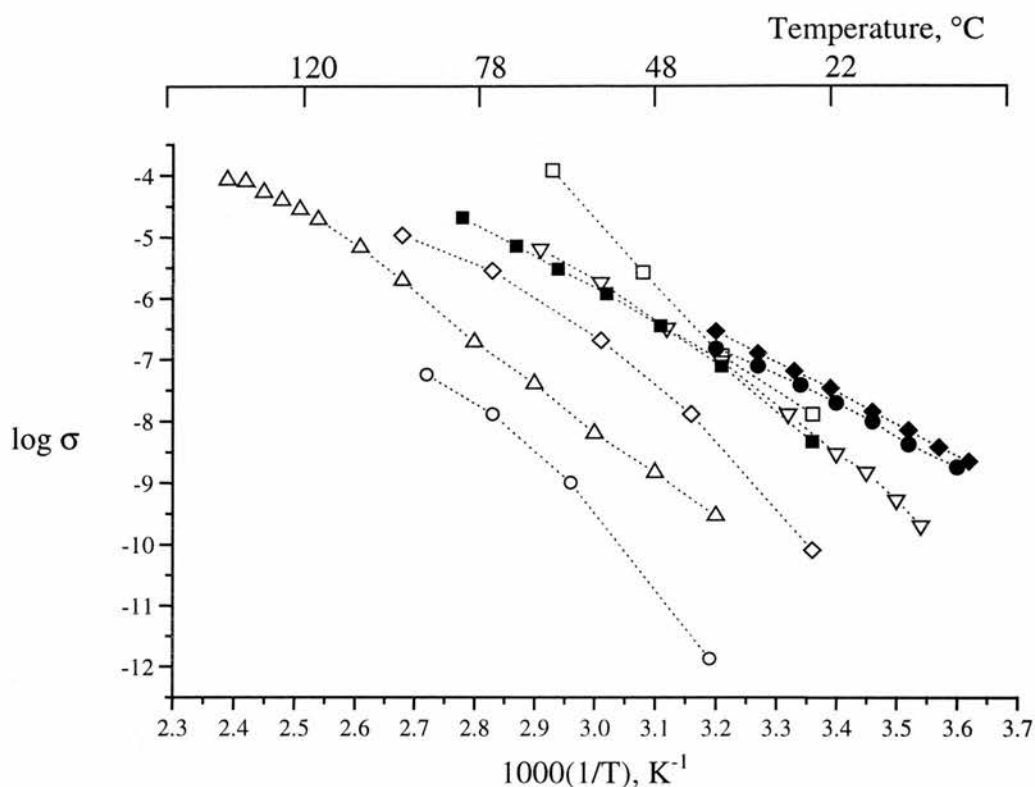


Fig.5.4. Temperature dependence of total ionic conductivity for the polymer electrolyte systems (all data are on first heating cycle):

$PEO_3:LiAsF_6$ ($M_w = 100,000$) – open circles

$PEO_6:LiAsF_6$ ($M_w = 100,000$) – open up triangles

$PEO_6:LiSbF_6$ ($M_w = 100,000$) – open diamonds

$PEO_{20}:LiAsF_6$ ($M_w = 100,000$) – open squares

$PEG_6:LiPF_6$ ($M_w = 1,000$) – solid circles

$PEG_6:LiSbF_6$ ($M_w = 1,000$) – solid diamonds

$PEG_6:LiSbF_6$ ($M_w = 2,000$) – solid squares

$PEO_6:LiSbF_6$ ($M_w = 100,000$) amorphous complex – open down triangles

Assuming that the conductivity data for the crystalline complexes obeyed the Arrhenius law (eq.5.3.) the following values for activation energy for ion conduction were obtained from the plots $\ln\sigma$ vs. $1/T$:

Complex	Molecular weight	E_a , eV
PEO ₃ :LiAsF ₆	100,000	1.77
PEO ₆ :LiAsF ₆	100,000	1.54
PEO ₆ :LiSbF ₆	100,000	1.49
PEO ₂₀ :LiAsF ₆	100,000	1.85
PEG ₆ :LiSbF ₆	2,000	1.23
PEG ₆ :LiSbF ₆	1,000	1.01
PEG ₆ :LiPF ₆	1,000	0.97

These values were relatively high compared to some values of E_a reported in the literature, e.g. 0.3-0.7eV for PEO_x:LiClO₄ [11], 0.7eV for PEO_x:LiCF₃SO₃ [11], 0.3-0.4eV for PEO_x:LiBF₄ [12], 1.11eV for PEO_{4.5}:LiSCN [13].

The conductivity curves in fig.5.4 exhibit no discontinuities or transition temperatures, i.e. the conductivity increases gradually over the whole temperature range. In contrast, one would often find two regions with different activation energy in many polymer electrolytes that are not fully amorphous [13-15].

Conductivity data on both heating and cooling cycles were collected for several polymer electrolyte systems. In some cases, there were no significant variations in the temperature dependence of the ionic conductivity on heating and cooling. For some complexes, however, strong dependence on the thermal treatment of the samples was observed.

Conductivity data were collected for the sample $\text{PEO}_6\text{:LiAsF}_6$ ($M_w = 100,000$) on both heating and cooling cycle (fig.5.5). Due to the relatively good thermal stability of this complex, measurements can be made above the melting point; the two points at the highest temperatures correspond to conductivity values of the melt. Since the melt is very viscous, measurements can be made above the melting point without losing the electrical contact between the sample and the electrodes. Hysteresis is observed on cooling and this is consistent with the DSC measurements according to which this complex recrystallises at lower temperature (80-90°C) but not at the melting temperature (140°C). The results indicate that out of the hysteresis interval, the conductivity values are similar on heating and cooling cycle.

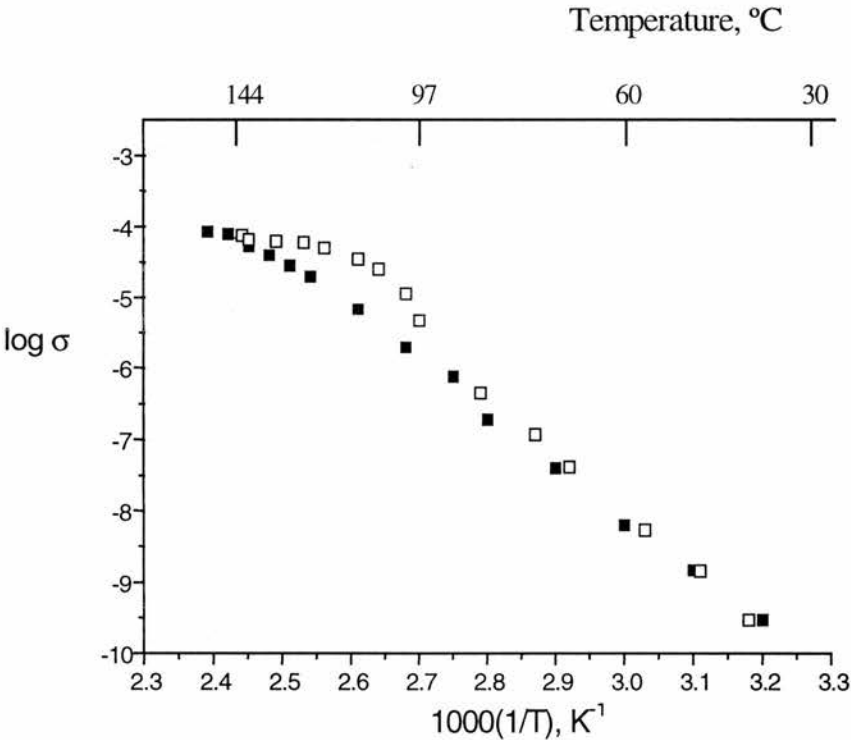


Fig.5.5. Total ionic conductivity on heating (squares) and cooling (open squares) for the complex $\text{PEO}_6\text{:LiAsF}_6$ ($M_w = 100,000$)

In contrast, different conductivity values were obtained on heating and cooling for the complex $\text{PEO}_6\text{:LiSbF}_6$ of $M_w = 100,000$ (fig.5.6). During the cooling cycle, the bulk resistance did not reach equilibrium values and changed continuously over long time intervals at a given temperature. The data reported here were collected after 1-1½ hour-equilibrating time for each temperature but it should be noted that no equilibrium could be achieved even after longer time intervals. This demonstrated that there was strong time dependence of the conductivity at a given temperature. As seen in fig.5.6, the conductivity was higher on cooling and the difference ranged from 0.5 orders of magnitude at higher temperatures up to 3 orders of magnitude at room temperature.

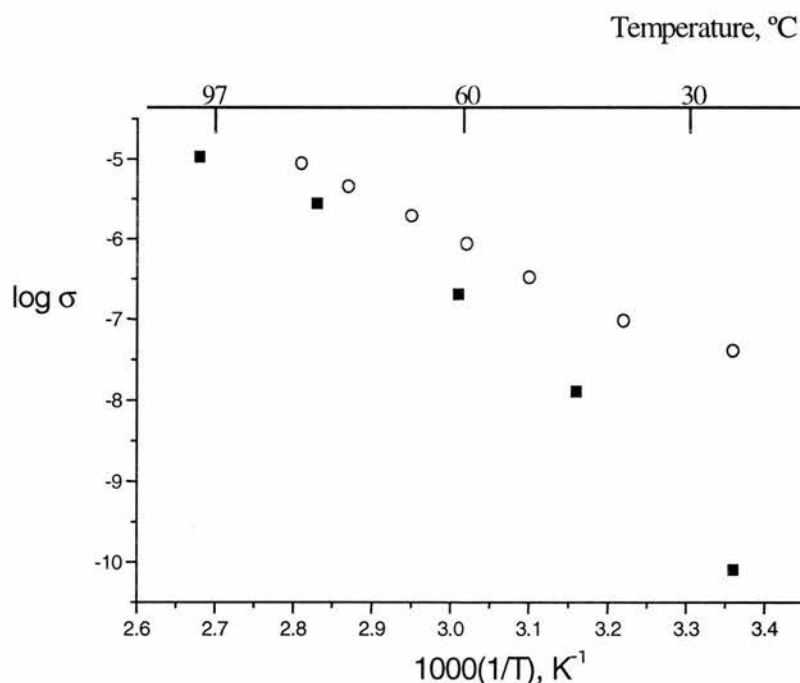


Fig.5.6. Total ionic conductivity on heating (squares) and cooling (open circles) for the complex $\text{PEO}_6\text{:LiSbF}_6$

Two radically different reasons for the observed hysteresis can be considered: *i*) slow rate of re-crystallisation and increased fraction of amorphous phase on cooling (i.e. higher conductivity on cooling due to bigger fraction of amorphous material which is more conducting) and *ii*) improved crystallinity in the course of slow cooling which has the effect of annealing (i.e. higher conductivity on cooling due to better crystallinity which implies higher level of conductivity in the crystalline phase than in the amorphous phase). Explanation *i*) can be rejected because the measurements did not involve melting of the complex (due to its poor thermal stability) and hence no re-crystallisation could have occurred but only annealing of the crystalline complex. Therefore only explanation *ii*) can be accepted which implies that the crystalline phase may support higher conductivity than the analogous amorphous phase.

The absence of hysteresis for the complex $\text{PEO}_6\text{:LiAsF}_6$ (fig.5.5) may be explained with the much better “initial” crystallinity of this complex which does not change significantly in the course of slow cooling or annealing within the time intervals of the present experiments.

In the case of the stoichiometric complexes $\text{PEG}_6\text{:LiXF}_6$ ($X = \text{P, Sb}$) prepared with low-molecular weight polymer ($M_w = 1,000$), the impedance measurements on heating and cooling produced the same conductivity values (fig. 5.7).

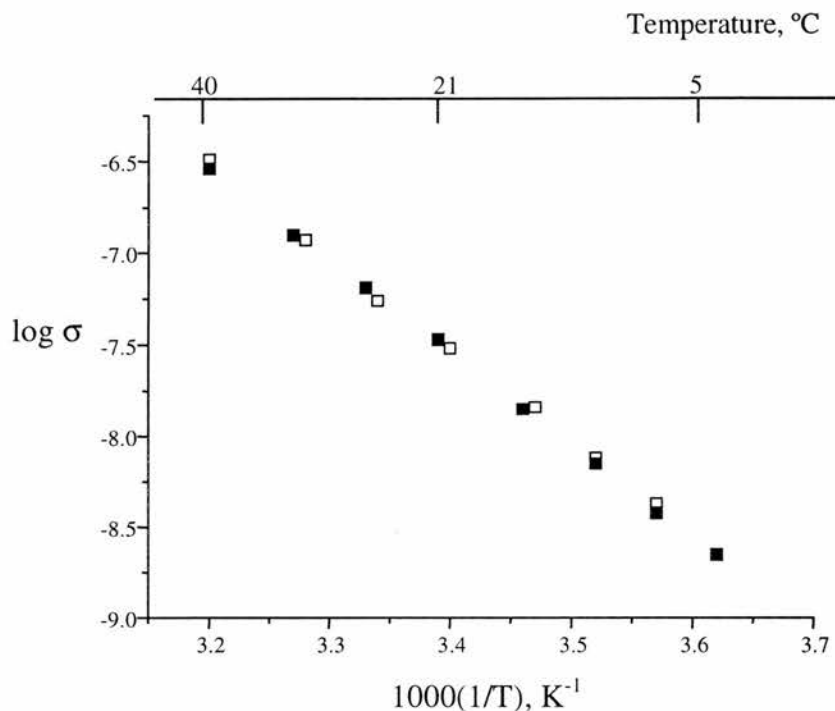


Fig.5.7. Total ionic conductivity on heating (solid squares) and cooling (open squares) for the complex $\text{PEG}_6\text{:LiSbF}_6$ ($M_w = 1,000$)

5.2.3b. Ionic conductivity and its relation to the degree of crystallinity and molecular weight

The electrical measurements on samples of different molecular weight show significant differences in the conductivity behaviour. As already discussed in Chapter 2, the use of low molecular weight polymer influenced the degree of crystallinity of the stoichiometric complexes. According to the XRD and NMR data, the stoichiometric complexes of $M_w = 1,000$ were ~100% crystalline while the stoichiometric complexes of $M_w = 100,000$ contained, on average, 5-10% amorphous material. As shown in fig.5.4, the conductivity values are higher for the complexes of low molecular weight (higher degree of crystallinity). This trend is very clearly seen for the complexes $\text{PEO}_6\text{:LiSbF}_6$ which have been prepared with three different molecular-weight polymers (100,000, 2,000 and 1,000). At room

temperature, the conductivity of the complex $\text{PEG}_6\text{:LiSbF}_6$ of $M_w = 1,000$ is about 2.8 orders of magnitude higher than the conductivity of the same complex of $M_w = 100,000$. In addition, the conductivity of the complexes $\text{PEG}_6\text{:LiSbF}_6$ and $\text{PEG}_6\text{:LiPF}_6$ of $M_w = 1,000$ at room temperature is higher than all of the other samples, including the amorphous complex $\text{PEO}_6\text{:LiSbF}_6$ and the dilute complex $\text{PEO}_{20}\text{:LiAsF}_6$.

The temperature dependence of the conductivity for the low molecular weight complexes can be well described by a straight line in agreement with the Arrhenius equation (eq.5.3.) In contrast, the temperature dependence for the high molecular weight complexes is represented by curved plots which are more characteristic of amorphous polymer electrolytes. This type of temperature dependence is better described by the WLF – type equation, the VTF relation or the Gibbs configurational entropy model rather than the Arrhenius equation. It is possible that in the case of the high molecular weight complexes, the mechanism of ionic conduction and the conductivity values were influenced by the presence of amorphous material in the crystalline complexes. As a whole, the conductivity behaviour of the high molecular weight crystalline complexes is complicated and this probably reflects the multi-phase nature of these samples. As already noted, the conductivity values for the low molecular weight (fully crystalline) complexes are reproducible at a given temperature, regardless of the previous thermal treatment of the sample (e.g. on heating, cooling, or second heating cycle).

The experimental data indicate that ion transport is energetically more favourable in the more organised crystalline environment of the low molecular weight complexes than in the more disordered, partially amorphous environment of the high molecular weight complexes. This result may have important implications regarding the mechanism of ion transport in the systems under study: ion transport in disordered environment occurs by means of long range re-organisation (segmental motion) of the polymer chains which is a relatively slow process. The ion transport mechanism in the crystalline complexes ($M_w = 1,000$) might be more localised and probably involves hopping between neighbouring lattice sites of similar energy and environment.

5.3. CONDUCTIVITY STUDIES USING NON-BLOCKING ELECTRODES

5.3.1. A.c. measurements with non-blocking electrodes

Impedance measurements with non-blocking electrodes can be used to determine a whole range of electrical properties such as charge transfer resistance, transport numbers, and double layer capacity.

For the case of a.c. measurements with non-blocking electrodes, the Li^+ conducting electrolyte is sandwiched between two identical lithium electrodes. The equivalent circuit for this cell configuration is shown in fig. 5.8.

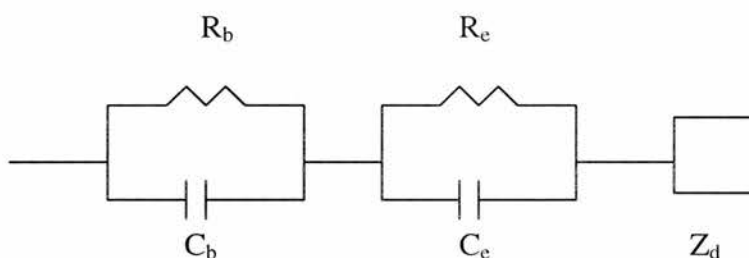


Fig.5.8. Equivalent circuit for electrolyte with non-blocking electrodes

The a.c. response of the electrolyte is represented by a parallel combination of the bulk resistance and capacitance, R_b and C_b , giving rise to a high-frequency semicircle in the complex impedance plane. The a.c. response of the electrode/electrolyte interface is represented by a parallel combination of R_e and C_e . R_e may be identified with the electrode reaction resistance and C_e may be identified with the electrode capacitance C_e . C_e is often found to be nearly the double layer capacitance of two diffuse space charge layers in series,

one from each electrode for identical plane parallel electrodes [9]. The parallel combination $R_e C_e$ gives rise to a low-frequency semicircle at the intermediate frequencies. At the lowest frequencies, a third feature can be observed and this can be attributed to diffusion arising from the presence of concentration gradient within the electrolyte. It is represented by Z_d in the equivalent circuit. It should be noted that all three features may not be observed in every case.

Experimental details

The impedance measurements were made as described in Section 5.2.1. Lithium metal electrodes of diameter 0.8cm were punched from Li ribbon. The surfaces of the electrodes were carefully cleaned before loading into the cells. The electrolyte films were mounted between two identical lithium metal electrodes which were then sandwiched between the stainless steel electrodes of a spring-loaded cell.

Results and discussion

Impedance measurements with non-blocking (Li metal) electrodes were made for the complex $\text{PEG}_6\text{:LiSbF}_6$ of $M_w = 1,000$. The measurements were performed at 32-35°C and this temperature was chosen for two reasons: first, it was low enough to avoid thermal decomposition of the sample on prolonged heating and, second, it was sufficiently high to observe and resolve the first two semicircles which could be anticipated in the complex impedance plots. The impedance measurements were made with the aim of studying the behaviour of the above polymer electrolyte system when placed in contact with lithium metal electrodes for long time intervals.

The a.c. response of the cell was monitored at various times during the course of 24 hours (fig.5.9). Two arcs could be distinguished and the first of these (at the high frequencies) could be attributed to the electrolyte resistance R_b and capacitance C_b . The second arc represented the resistance R_e and the capacitance C_e at the electrode/electrolyte interface and

it could be assigned to growing passivating layers [16,17] on the lithium metal electrodes. These assignments were based on the values of the capacitances C_b and C_e .

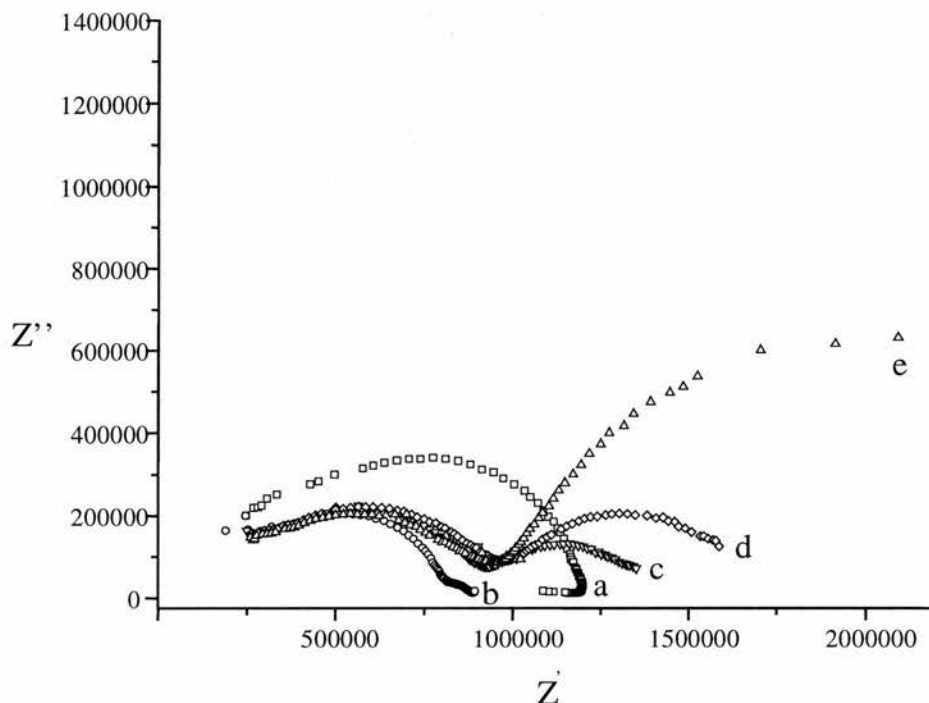


Fig.5.9. Variation of the a.c. response of the cell $\text{Li/PEG}_6\text{:LiSbF}_6\text{/Li}$ with time: a) 30min (squares); b) 90min (circles); c) 150min (down triangles); d) 350min (diamonds); e) 1400min (up triangles). The frequency range is 0.1Hz – 100kHz.

As seen in fig.5.9a, an electrode reaction (nucleation) begins almost immediately after assembling the cell. This is evident from the loop in the a.c. plot observed at the low frequencies. Initially the bulk resistance varies until thermal equilibrium is reached after about 2 hours. In contrast, R_e continues to increase with time and reaches a stabilised value after 30 – 40 hours. These variations in the resistance R_e were observed for several cells with Li metal electrodes. Similar results have been obtained for other polymer electrolytes [13, 16-18]. For example, time-dependent values of R_e for the system $\text{Li/PEO}_{20}\text{:LiCF}_3\text{SO}_3\text{/Li}$ have been

reported [16-18] and these were interpreted as being indicative of the growth of an ionically conducting film at the lithium electrode/polymer electrolyte interface.

The bulk capacitance was stable during the experiment and its values were within the expected range $1\text{-}3\text{pFcm}^{-2}$. C_e increased in the course of the measurements starting from $0.03\mu\text{Fcm}^{-2}$ and reaching final values of $\sim 0.5\text{-}0.6\mu\text{Fcm}^{-2}$. This value is smaller than one would expect on the basis of the double-layer theory. A typical double-layer capacity for a metal – electrolyte interface will generally exceed $20\mu\text{Fcm}^{-2}$ [9, 17]. Therefore the capacitance values also suggest the formation of a passivating film on the lithium metal electrodes.

It should be noted that the capacitance C_e can be expected to decrease during the growth of the passivating layer since the thickness of the layer increases ($C_e \sim A/l$). The variation of C_e in the present experiments suggests that other factors may also influence C_e , e.g. the nature of the passivating layer may change with time and this will result in variation of the dielectric constant ($C_e \sim \epsilon$).

In the present work, the formation of passivating layers was confirmed by the visual change of the colour and appearance of the lithium metal electrodes after contact with the electrolyte material. Black surface layer on the electrodes was observed after disassembling of all cells. Fauteux [17] commented on the nature of the passivating film on the Li metal electrodes in the cell $\text{Li/PEO}_x\text{:LiCF}_3\text{SO}_3\text{/Li}$. He pointed out that at low salt concentrations, residual inorganic compounds used as catalysts in the ethylene oxide polymerization, may react with the lithium metal to form a passivating film. For high-salt-concentration electrolytes, however, an electrochemical reaction of LiCF_3SO_3 leading to the formation of LiF has been noted. Since LiF is not soluble in PEO, it remains at the electrode/electrolyte interface. In addition, XPS studies of lithium surfaces immersed in organic solutions of LiAsF_6 and LiPF_6 [19, 20] have suggested the formation of LiF on the lithium surface. The formation of LiF in these studies was found to depend strongly on the kind of salt.

The observation of black surface layers in the present work suggests that these can not be just LiF (LiF is white). Therefore the nature of the passivating films is more complicated and may also involve reaction of the lithium metal with residual N₂ gas in the glove-box atmosphere, or with impurities from the polymer.

While the nature of the passivating layers on the lithium metal electrodes was not studied in the present work, the electrolyte samples were subjected to several tests to establish whether these samples were effected by placing in the Li cells. X-ray data of electrolyte films collected before and after the electrical measurements indicated that there was significant reduction in the degree of crystallinity of the samples after the measurements. These results suggested that the electrochemical reaction at the electrode/electrolyte interface caused irreversible changes in the structure of the electrolyte in terms of the long-range order. Since no peaks for impurities or other new crystalline phases were observed, it could be concluded that the structural changes of the electrolyte samples were related to disordering and loss of long-range structure. Also, there was a possibility that new amorphous phases had been formed which could not be identified by X-ray diffraction.

An anomalous feature of the Li metal cells was the non-zero open-circuit potential (OCP). The OCP changed significantly within 24 hours, starting from 10-20mV after assembling the cell and reaching values of 250 – 450mV after 24 hours. The final values were different for each cell. In addition, the OCP was not constant even after 24 hours but there were fluctuations around a certain value. In some cases, after longer time intervals (2 – 3 days) the OCP dropped again close to the initial values (10 – 30mV). In other words, anomalous OCP was observed in all Li metal cells but the values and the trends in the changes of the OCP were not reproducible. This suggested that the variations in the OCP might be due to the occurrence of random processes at the electrolyte/electrode interface (e.g. highly anisotropic random orientation of crystallites near the electrodes which, in extreme cases, could result in non-symmetrical cell configuration). Taking into account the X-ray data for the electrolyte samples as discussed earlier in this section, the variations of the OCP could

be a result of the formation of amorphous phase and its random distribution at the electrolyte/electrode interface.

5.3.2. Direct current measurements

Direct current techniques are the most straightforward method for measuring the ionic conductivity. However, their use is significantly less than that of a.c. techniques because of the problems arising from the influence of the electrode contacts on the measured electrolyte conductivity. When a d.c. voltage is applied across a cell with non-blocking electrodes, the kinetics of the charge transfer process at the electrodes (i.e. charge transfer to and from electrons and ions at the two interfaces) are not infinitely facile and therefore there is a resistance R_{el} associated with this process. This results in a built-up of charge on either side of the interface, which produces an associated charge – transfer capacitance in parallel with the resistance R_b . Thus with a two-electrode cell the applied voltage V causes a current to flow through the two electrode (charge transfer) resistances and the electrolyte resistance in series and hence $V/I = (2R_{el} + R_b)$. Normally R_{el} is not negligible in comparison with R_b and therefore this method does not give the electrolyte resistance R_b directly.

Due to the above charge transfer processes, a charge gradient (and correspondingly, ionic concentration polarisation) is normally established across the electrolyte. This can be used to positive advantage in the construction of polarisation cells which allow one to determine the contribution of individual ionically conducting species [1, 2, 16, 18].

The d.c. measurements were made as described earlier (section 5.2.1). Normally, a potential difference of 10mV was applied to the cells and the response was monitored during the course of 10 – 30 hours by applying an a.c. perturbation on top of the d.c. value. The aim of these measurements was to study the behaviour of the system Li/PEG₆:LiSbF₆/Li when

subjected to d.c. bias and, eventually, to evaluate the Li^+ transference numbers using the d.c. polarisation technique [16, 18]. In this method, transference numbers of binary polymer electrolytes may be obtained from polarisation data on cells of the type $\text{M/polymer:M}^+\text{X}^-/\text{M}$. In addition, allowance is made for electrode resistances. The method is based on measurement of the initial and steady-state currents (I^0 and I^s respectively) with a fixed applied potential in a cell of the type as described above. It has been shown that under defined conditions the transference number $T_+ = I^0/I^s$. For real electrolytes, the error introduced by using polarisation voltages of up to 10mV is acceptable.

D.c. measurements were carried out on two systems - crystalline $\text{PEG}_6\text{:LiSbF}_6$ ($M_w = 1,000$) and amorphous $\text{PEO}_6\text{:LiSbF}_6$.

Crystalline $\text{PEG}_6\text{:LiSbF}_6$

A d.c. bias of 10mV was applied to the cell $\text{Li/PEG}_6\text{:LiSbF}_6/\text{Li}$ and the a.c. response was monitored at various times during the course of d.c. polarisation (fig.5.10). The results were consistent with the growth of passivating layers on the lithium electrodes as already discussed in the previous section.

The surface layer capacitance calculated from the impedance data was in the range $0.2 - 0.5\mu\text{Fcm}^{-2}$. The passivating layers increased in resistance with time and no stable value was reached even after 30 hours. The bulk resistance initially changed (20 –25% within 900min) and then a relatively constant value was observed till the end of the measurements. The bulk capacitance values were in the range $1 - 3\text{pFcm}^{-2}$.

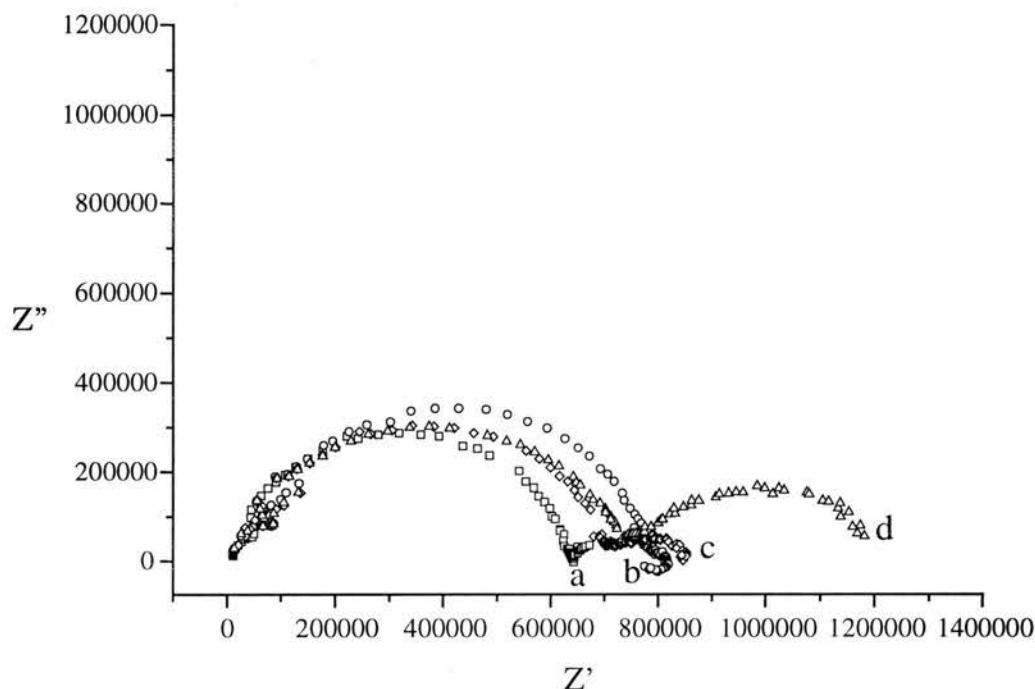


Fig.5.10. A.c. impedance of the cell $\text{Li/PEG}_6\text{:LiSbF}_6\text{/Li}$ at 30°C polarised with a potential difference of 10mV: a) polarisation time $t=0\text{min}$, i.e. before application of d.c.voltage (squares), b) $t = 197\text{min}$ (circles), c) $t = 856\text{min}$ (diamonds) d) $t = 1600\text{min}$ (triangles)

The main problem in these measurements was the non-zero open-circuit potential (OCP) which made it impossible to evaluate the Li^+ transference numbers. The OCP changed significantly with time and no constant values were obtained after long time intervals. Although polarisation measurements were attempted in the course of relative stabilisation of the OCP, the fluctuation of the voltage before and after the polarisation runs were significant and thus the errors in the applied voltage values exceeded 50% in the best cases. As a result, the current values necessary for T_+ evaluation could not be reliably measured.

The electrochemical stability of the samples when subjected to higher d.c. voltages was not studied in detail. The application of a d.c. voltage of 20mV gave similar results as described above. D.c. voltages of 100mV, however, caused irreversible changes of the

electrolytes. Fig.5.11 shows the a.c. impedance plot of a cell which has been subjected to a d.c. bias of 100mV for 5 min. It is evident that the high-frequency semicircle is significantly broadened and most probably consists of two melded semicircles. The second semicircle at the low frequencies can be associated with the passivating layers at the electrolyte/electrode interface.

XRD tests on electrolyte samples subjected to a d.c. voltage of 100mV show that the crystalline samples transform to completely amorphous material after such d.c. polarisation. In other words, the application of a high d.c. voltage (>100mV) results in irreversible structural changes and disordering in the electrolyte.

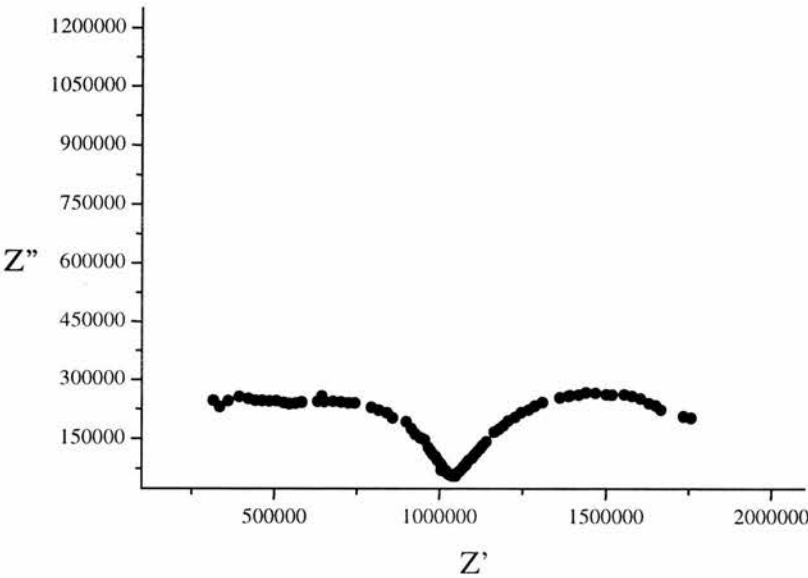


Fig.5.11. A.c. response of a cell Li/PEG₆:LiSbF₆/Li which has been subjected to a d.c. bias of 100mV for 5 min.

Amorphous PEO₆:LiSbF₆

The amorphous complex PEO₆:LiSbF₆ was tested in the same way as already described for the crystalline complex PEG₆:LiSbF₆. The experimental data demonstrated that the electrochemical behaviour of the amorphous complex PEO₆:LiSbF₆ was different from the corresponding crystalline complex. Fig 5.12 shows the a.c. response at various times for the cell Li/ PEO₆:LiSbF₆/Li polarised with a potential difference of 10mV. Again, two semicircles are observed in the complex impedance plots and these can be associated with the bulk resistance and capacitance of the electrolyte (at high frequencies) and the charge transfer resistance and capacitance at the electrodes (at low frequencies).

In contrast to the crystalline electrolyte PEG₆:LiSbF₆, the charge transfer resistance R_e does not change much with time while the bulk resistance represented by the high frequency semicircle continues to increase in the course of the d.c. polarisation. At longer times, the two semicircles overlap significantly.

The capacitance values C_b were within the range expected for bulk capacitance and the values of C_e were in the range $0.1 - 0.5 \mu\text{Fcm}^{-2}$.

As a whole, the results show that the electrochemical behaviour of the amorphous compound PEO₆:LiSbF₆ is complicated. The complications probably arise from long-range re-organisation processes which take place in this amorphous phase (evident from the NMR and X-ray diffraction studies). Therefore, further spectroscopic studies (mainly on the microscopic level) are necessary to understand the structure, dynamics and electrochemistry of these amorphous materials.

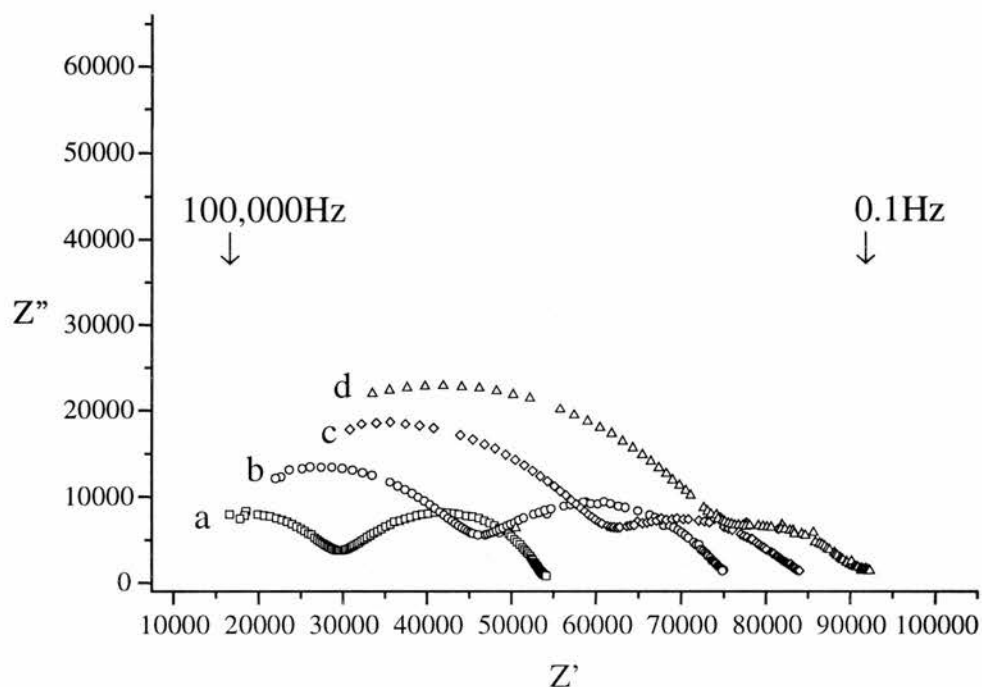


Fig.5.12. A.c. impedance of the cell Li/amorphous $\text{PEO}_6\text{:LiSbF}_6\text{/Li}$ at 47°C polarised with a potential difference of 10mV: a) polarisation time $t=0\text{min}$, i.e. before application of d.c.voltage (squares), b) $t = 399\text{min}$ (circles), c) $t = 821\text{min}$ (diamonds) d) $t = 1200\text{min}$ (triangles)

5.4. CONCLUSIONS

1. Levels of conductivity

It has been demonstrated that the crystalline (ordered) phases of the polymer electrolytes under study may exhibit higher conductivities than the analogous amorphous (disordered) systems above their glass transition temperature. This is in contrast with the view that ionic conductivity in polymer electrolytes occurs mainly in the amorphous phases where ion transport is related to the segmental motion of the polymer host. The ionic conductivity in

the crystalline 6:1 complexes is most probably related to their distinctive structure which defines permanent pathways for ion transport (discussed in Chapter 4).

2. Transference numbers

The electrochemical studies did not provide reliable information on the Li^+ transference numbers. Therefore it is not clear which ions contribute to the ionic conductivity. This issue is addressed in the NMR studies as discussed in Chapter 6.

3. Stability vs. Li metal electrodes

It is clear that the electrochemical stability of the electrolytes vs. Li metal electrodes is limited. This issue is not studied in detail in the present work but obviously this is of particular interest in terms of the practical application of these materials. Further studies are necessary to establish precisely the electrochemical stability window of the electrolytes under investigation as well as their compatibility with various lithium electrodes.

5.5. REFERENCES

1. P.G.Bruce, in *Polymer Electrolyte Reviews*, Ed. by J.R.MacCallum and C.A.Vincent, Elsevier Science Publishers Ltd., 1989
2. R.Linford, in *Electrochemical Science and Technology of Polymers*, Ed.by R.Linford, Elsevier Science Publishers, 1990
3. A.V.Chadwick and M.R.Worboys, in *Polymer Electrolyte Reviews*, Ed. by J.R.MacCallum and C.A.Vincent, Elsevier Science Publishers Ltd., 1989
4. D.R.Payne and P.V.Wright, *Polymer*, **23**, 690 (1982)
5. D.Fauteux, M.D.Lupien and C.D.Robitaille, *J.Electrochem.Soc.*, **134**, No11, 2761

6. A.R. West, in *Solid State Electrochemistry*, Ed. by P.G.Bruce, Cambridge University Press, 1995
7. F.L.Tanzella, W.Bailey, D.Frydrych, G.Farrington and H.S.Story, *Solid State Ionics*, **5**, 681 (1981)
8. L.C.Hardy and D.F.Shriver, *J.Amer.Chem.Soc.*, **107**, 3823 (1985)
9. J.R.Macdonald and J.A.Garber, *J.Electrochem.Soc.*, **124**, No.7, 1022 (1977)
10. J.Ross Macdonald, *J.Chem.Phys.*, **61**, No.10, 3977
11. C.D.Robitaille and D.Fauteux, *J.Electrochem.Soc.*, **133**, No2, 315 (1986)
12. G.Chiodelli, P.Ferloni, A.Magistris and M.Sanesi, *Solid State Ionics*, **28-30**, 1009 (1988)
13. P.R.Sorensen and T.Jacobsen, *Electrochim.Acta*, **27**, No.12, 1671 (1982)
14. B.L.Papke, M.A.Ratner and D.F.Shriver, *J.Electrochem.Soc.*, **129**, 1694 (1982)
15. D.Benrabah, D.Baril, J.-Y.Sanchez and M.Armand, *J.Chem.Soc., Faraday Trans.*, **89(2)**, 355 (1993)
16. P.G.Bruce, J.Evans and C.A.Vincent, *Solid State Ionics*, **28-30**, 918 (1988)
17. D.Fauteux, *Solid State Ionics*, **17**, 133 (1985)
18. J.Evans, C.A.Vincent and P.G.Bruce, *Polymer*, **28**, 2324 (1987)
19. K.Kanamura, H.Tamura, S.Shiraishi and Z.Takehara, *Electrochim.Acta*, **40(7)**, 913 (1995)
20. K.Kanamura, H.Tamura and Z.Takehara, *J.of Electroanal.Chem.*, **333(1-2)**, 127 (1992)

CHAPTER 6

NMR STUDIES

6.1. THEORETICAL BACKGROUND

6.1.1. Magnetic interactions in the solid state

The main interactions involving a nucleus with a magnetic moment which may occur in the solid state are:

1. the Zeeman interaction with the magnetic field;
2. direct dipole-dipole interactions with other nuclei;
3. magnetic shielding by the surrounding electrons giving chemical shifts;
4. spin-spin couplings to other nuclei;
5. quadrupolar interactions which will be present for nuclei with spin $>1/2$ only and

will often dominate the NMR spectra of these nuclei.

In a particular solid state system, one or two of the interactions will determine the characteristics of the spectrum [1-5]. Typical values for the interactions are given in Table 6.1.

Most of the above magnetic interactions are relevant to the present work and they are discussed briefly here. The quadrupolar effects are reviewed in more detail in Chapter 6.1.6 since these interactions are of particular importance in the present experiments.

<i>Interactions</i>	<i>Range, Hz</i>
Zeeman	$10^6 - 10^9$
Dipolar	$0 - 10^5$
Chemical shift	$0 - 10^5$
Scalar coupling	$0 - 10^4$
Quadrupolar	$0 - 10^9$

Table 6.1. Approximate ranges of the different spin interactions [6]

Zeeman interactions

The Zeeman interaction occurs for all nuclei with odd atomic mass or odd atomic number between the magnetic moment of the nucleus and the applied magnetic field B_0 , yielding $2I+1$ energy levels (where I is the nuclear spin quantum number) of separation

$$hw_0 = \gamma h B_0 \quad (6.1)$$

where γ is the magnetogyric ratio and w_0 is the corresponding Larmor frequency. The interaction is linear with the applied magnetic field, larger separations of the energy levels occurring at higher fields with a corresponding increase in the population difference between them and increase in the signal-to-noise ratio of the spectrum.

Dipolar interactions

The dominant interactions in solids containing spin $I = 1/2$ nuclei is usually the dipole – dipole interaction. The local field B_{loc} at a nucleus I generated by a nucleus S is given by:

$$B_{loc} = \pm \mu_S r_{IS}^{-3} (3\cos^2\theta_{IS} - 1) \quad (6.2)$$

where μ_S is the magnetic moment of S , r_{IS} is the internuclear distance, θ is the angle between the internuclear vector and the B_0 field. The plus or minus sign depends on the orientation of the spins generating the local field with or against the applied field. Thus the characteristics of the NMR signal depend on the nucleus producing the local field, the internuclear distance and the orientation of the internuclear vector with respect to the magnetic field.

Chemical shift (CS) interactions

The chemical shift is produced by the electrons which shield the nucleus from the applied magnetic field. The electron distribution usually has a definite directional character and as a result the chemical shift takes on directional properties.

The axially symmetric chemical shift depends on $(3\cos^2\theta - 1)$ where θ is the angle between the magnetic field and the principal axis about which the shift is defined. Since in a polycrystalline sample the crystallites are oriented at random, a dispersion of the peak positions is observed.

The magnitude of CS depends also on the nucleus being studied and the chemical environment in which the nucleus resides; different CS can be observed for a given nuclear

species in different environments. The chemical shift is dominated by the immediate electrons around the nucleus.

The CS is a shielding effect and therefore it is proportional to the applied magnetic field, i.e. the interactions will be larger and more important at higher magnetic field strengths. Since the chemical shift interaction involves the surrounding electrons, it is the most sensitive interaction to the geometry and identity of the other atoms surrounding a particular nucleus.

Spin-spin coupling interactions

The indirect interaction between a pair of spins is field independent and is usually smaller than the other interactions under consideration.

Quadrupolar interactions

The quadrupolar interaction occurs only when $I > 1/2$ and arises from the interaction of the nuclear electric quadrupole moment eQ with the non-spherically symmetrical field gradient around the nucleus.

6.1.2. Techniques for line narrowing in solids

The NMR spectra of polycrystalline solids are often broad and featureless. In order to obtain useful and high-resolution spectra, it is necessary to apply the relevant techniques for line narrowing.

Magic angle spinning (MAS)

The MAS experiment involves spinning of the sample container at the so-called magic angle $54^{\circ}44'$ in the applied magnetic field (fig.6.1). Line narrowing occurs because both the dipolar coupling and the chemical shift anisotropy contain an angular dependence of the form $3\cos^2\theta - 1$. Therefore dipolar splitting and chemical shift anisotropy (CSA) can be averaged when $3\cos^2\theta - 1 = 0$, i.e. when $\theta = 54^{\circ}44'$.

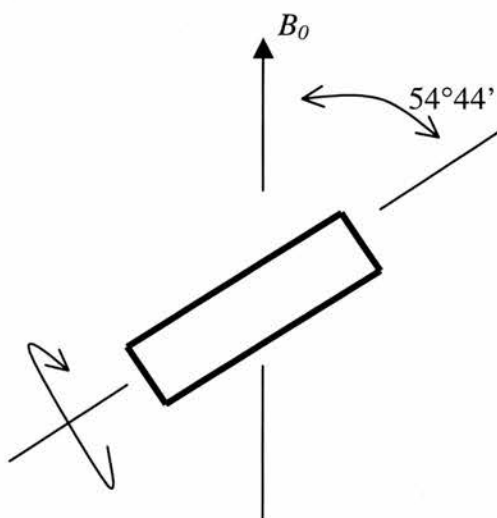


Fig.6.1. Geometry of the sample with respect to the applied magnetic field B_0 in MAS experiment

In order for the MAS experiment to narrow a line which is broadened by chemical shift anisotropy (CSA), the spinning frequency must be at least of the order of the CSA linewidth. Since the linewidth in solids is usually about few kilohertz, MAS experiments can be successfully performed with rotation at about 3-10kHz. If the CSA linewidth is larger than the spinning frequency, a set of sharp lines is observed; these lines are spaced at the spinning frequency and centered on the isotropic chemical shift.

MAS can reduce dipolar broadened lines when the dipolar interactions are not very large. In organic solids, usually MAS alone can not produce line narrowing. In many inorganic solids, however, there are relatively few or no protons or ^{19}F . The dipolar broadening in this case is small and MAS can reduce the linewidths to 50-100Hz.

Dipolar decoupling

In some solids there is high concentration of different magnetic nuclei and the heteronuclear dipolar interactions (e.g. C – H) can be very strong. The linewidth in this case can be significantly reduced by heteronuclear decoupling with high decoupling power during the observation of the free induction decay. Dipolar decoupling is normally used in combination with MAS. Then both CSA and dipolar broadening can be reduced.

Other techniques

There are other techniques for line narrowing in solids, e.g. multiple-pulse sequences for removing the homonuclear dipolar interactions, cross polarisation, etc. Their discussion, however, is outside the scope of this work.

6.1.3. Free induction decay (FID) measurements

A basic pulsed experiment is to apply an intense pulse at the Larmor frequency, in order to tip the magnetisation 90° from the direction of the magnetic field (90° , or $\pi/2$ pulse). The signal obtained would correspond to a curve showing the exponential decay of the signal down to zero as the thermal population of the spin states was re-established. This signal is known as the free induction decay (FID) and it can be described by an exponential law.

The observed signal decreases, in fact, with a characteristic time T_2^* :

$$1/T_2^* = 1/T_2 + \gamma\Delta H_0, \quad (6.3)$$

where T_2 is the true transverse relaxation time essentially due to dipolar interactions (for $I = 1/2$ spins) and ΔH_0 is the applied field inhomogeneity. The term $\gamma\Delta H_0$ in eq.(6.3) is not always negligible and, in the case of amorphous or liquid phases, is comparable to $1/T_2$. To measure the FID accurately, the spin-echo technique can be applied which involves the application of a pulse π a time τ after the initial $\pi/2$ pulse. The spin-echo mechanism eliminates the adverse effect of field inhomogeneity.

In the solid state, the corresponding linewidth is much larger than $\gamma\Delta H_0$. The FID signal can be directly observed after the $\pi/2$ pulse.

Since the FID is a measurement of intensity as a function of time, it is often referred to as a time domain signal. The time domain signal can be converted into a frequency domain signal (i.e. intensity as a function of frequency) by means of Fourier transformation.

6.1.4. Relaxation times

Relaxation studies provide most direct information on the static and dynamic properties of solid electrolytes. These studies allow one to determine the motional correlation times which can be related to microscopic processes such as diffusion of ions and vacancies, moving defects, molecular rotations, etc.

Spin-spin relaxation time (transverse relaxation time) T_2

This is the time constant for the FID, i.e. the time for the transverse magnetisation $M(t)$ to decay to $1/e$ of its original value, $M(0)$, and is approximately equal to $1/\Delta\omega$, where $\Delta\omega$ is the linewidth (full width at half-maximum). In thermodynamic terms, T_2 is the relaxation time for the spins to come to internal thermal equilibrium following a perturbation.

Spin-lattice relaxation time T_1

After a sufficiently long time following a 90° pulse, the spins will return to a precession about the main magnetic field (z -direction) and the original magnetisation will be recovered. The characteristic relaxation time for this process is known as the spin-lattice relaxation time T_1 (since relaxation occurs by the loss of energy from the excited nuclear spins to the surrounding lattice). If the initial magnetisation along the z -axis was M_0 and the component at a time t s after the pulse has been applied is M_z , then M_z returns to M_0 by means of an exponential decay:

$$(M_0 - M_z) = M_0(1 - \cos\theta)\exp(-t/T_1) \quad (6.4)$$

where θ is the angle through which the magnetisation has been tipped.

Spin-lattice relaxation time in the rotating frame $T_{1\rho}$

The spins can be “locked” along certain directions, using specific pulse sequences. Thus the main magnetic field B_0 can be effectively removed and the characteristic time for the spins to relax in the B_1 field can be determined (B_1 is the oscillating radio-frequency magnetic field applied perpendicular to the B_0 field). This relaxation time is known as the spin-lattice relaxation time in the rotating frame $T_{1\rho}$. Since $B_1 \approx 10^{-3}B_0$, the smaller separation of the Zeeman levels means that smaller quanta are required to cause relaxation. Measurements of $T_{1\rho}$ are useful in the study of slow motions.

6.1.5. The application of solid state NMR for study of ionic motions

When molecules or ions undergo random translation or rotational motion, any nuclear magnetic moment which may be present will experience the rapidly fluctuating magnetic field produced by the neighbouring nuclear magnetic moments. The Fourier component of this time-variant field, having a frequency equal to the resonance frequency ω_0 , causes transitions between energy levels in the same manner as the applied radiofrequency field.

Bloembergen, Purcell and Pound [7] related the molecular motion to the relaxation rates as follows:

The fluctuations in the local field are assumed to follow an exponential time correlation function $G(t)$:

$$G(t) = G(0)\exp(-|t|/\tau_c) \quad (6.5)$$

where τ_c is the correlation time of the motional process. τ_c defines the time scale for changes of the local magnetic field experienced by the resonant nucleus. In the case of translational diffusion, τ_c can be regarded as the mean residence time of the atom on a lattice site and $(\tau_c)^{-1}$ as the jump frequency.

Because of the above assumption, the following general results for the relaxation rates $1/T_1$ and $1/T_2$ can be obtained:

$$1/T_1 \propto B_{loc}^2 (\tau_c / (1 + \omega_0^2 \tau_c^2)) \quad (6.6)$$

$$1/T_2 \propto \tau_c \quad (6.7)$$

B_{loc} is the part of the local field which is modulated by the local motion and ω_0 is the Larmor frequency.

The expression (6.7) holds only for $\langle \Delta w^2 \rangle^{1/2} \tau_c \ll 1$. For $\langle \Delta w^2 \rangle^{1/2} \tau_c > 1$, $1/T_2$ is given by the second moment so that $1/T_2 \propto \langle \Delta w^2 \rangle^{1/2}$ where Δw is the linewidth.

Normally the correlation time follows Arrhenius behaviour:

$$\tau_c = \tau_c^0 \exp(E_a/kT) \quad (6.8)$$

where E_a is the activation energy of the process. $1/\tau_c^0$ is the attempt frequency which is usually of the order of an optical phonon frequency (10^{12} to 10^{14} Hz) [8]. $1/\tau_c^0$ can be roughly identified with the oscillation frequency of the ion in its potential well.

Combining the above equations leads to the temperature dependence as shown in fig.6.2.

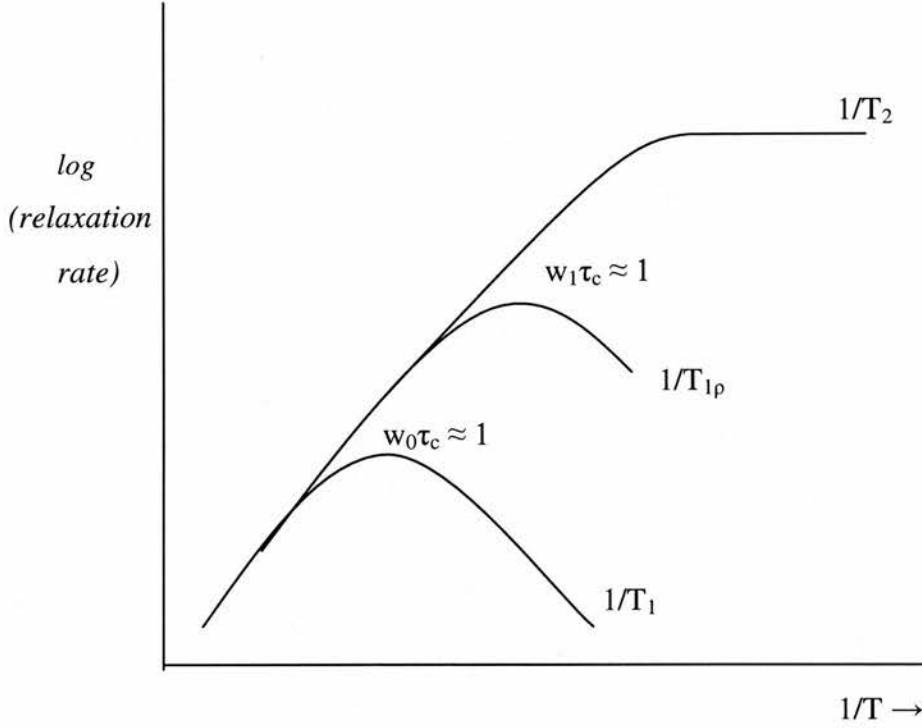


Fig.6.2. The variation of relaxation rates with temperature. $1/T_1$ peaks at $w_0\tau_c \approx 1$ and $1/T_{1\rho}$ peaks at $w_1\tau_c \approx 1$. $1/T_2$ begins to decrease when $\Delta w_{RL}\tau_c \approx 1$ (Δw_{RL} is the rigid lattice linewidth).

Several features of the relaxation rates can be noted. At high temperatures, i.e for large hopping rates, the three rates are equal:

$$1/T_2 = 1/T_{1\rho} = 1/T_1 \quad (w_0\tau_c \ll 1) \quad (6.9)$$

In this regime the relaxation rates are frequency independent but depend on τ_c .

At low temperatures $1/T_1$ is Larmor frequency dependent according to

$$1/T_1 \sim 1/w_0^2 \tau_c \quad (w_0\tau_c \gg 1) \quad (6.10)$$

At even lower temperatures

$$1/T_{lp} \sim 1/w_I^2 \tau_c \quad (w_I \tau_c \gg 1) \quad (6.11)$$

where w_I is the precession frequency in the radio-frequency magnetic field B_I .

The relaxation rates peak at different hopping rates. $1/T_{lp}$ has a maximum near $w_I \tau_c \approx 1$ and thus it is most sensitive to hopping rates $1/\tau_c \sim w_I \sim 10^5 \text{ s}^{-1}$. $1/T_I$ peaks near $w_0 \tau_c \approx 1$, i.e. for $1/\tau_c \sim w_0 \sim 10^8 \text{ s}^{-1}$. So the various relaxation rates can be measured to probe a wide range of ion hopping rates. The curves $\log(\text{rate})$ vs. $1/T$ are symmetrical and the activation energy E_a can be determined from the slopes.

In the case of translational diffusion, the diffusion coefficient D can be calculated from the Einstein equation:

$$D = a^2/6\tau_c \quad (6.12)$$

where a is the jump distance.

It should be noted that the above relationships can be applied in simple systems when only the magnetic dipole – dipole interactions are important and quadrupolar and paramagnetic interactions can be neglected. The model outlined above (the so-called BPP model) is too simple for solids and the following failures are often observed [9]: *i)* the $\log T_I$ vs. $1/T$ plot is not symmetrical with respect to the temperature at the T_I minimum; *ii)* the values of E_a deduced from this plot do not agree with those obtained from conductivity measurements; *iii)* the values of $1/\tau_c^0$ are not in the range of an optical phonon frequency; *iv)* T_I is not proportional to w_0^2 on the low-temperature side.

Several reasons for these deviations from the BPP theory can be noted. In many solid state systems the relaxation processes are nonexponential with respect to time over many orders

of magnitude around the Larmor frequency, i.e. the assumption in eq. (6.5) is not valid. Second, transport and relaxation processes in some disordered solids possess no characteristic time scale and there is a wide distribution of relaxation rates [10]. In addition, transport in crystalline solids may take place in only 1 or 2 dimensions which affects the correlation function $G(t)$ in eq.(6.5) [11].

There are some complications in applying the BPP theory to polymer electrolytes. First, the most studied cation nuclei (^7Li and ^{23}Na) are spin $I = 3/2$ nuclei and therefore nuclear quadrupolar effects are important. Second, the ionic species are often in different phases and the interpretation of the data is further complicated. Nevertheless, linewidth and relaxation time measurements have been widely used in the studies of ionic motion in polymer electrolytes [12-25].

6.1.6. Quadrupole effects in the solid state and relevant NMR techniques

If the nuclear spin is $I > 1/2$, the nuclear charge distribution will no longer be spherical and the nucleus will possess quadrupole moment. When the nucleus is not in cubic or higher symmetry site, the quadrupole moment interacts with the electric field gradient experienced by the nucleus giving rise to quadrupolar relaxation. The strength of the quadrupolar interaction between the quadrupole moment (eQ) and the electric field gradient (eq) is given by the quadrupolar coupling e^2qQ/h .

If the quadrupolar interaction is much smaller than the Zeeman interaction (i.e. $e^2qQ/h \ll \gamma\hbar B_0$), the energy shifts due to the quadrupolar interaction for a single nucleus may be obtained by first order perturbation theory and these are given by:

$$\Delta E_Q = 3/8(e^2qQ/h)(3\cos^2\theta - 1) \quad (6.13)$$

where ΔE_Q is the energy shift due to the quadrupolar interaction. The energy level diagram for a nucleus of spin $3/2$ is shown in fig.6.3. It can be seen that the central transition $1/2 \leftrightarrow -1/2$ is not affected by the quadrupolar interaction. This situation is quite general and for most quadrupolar nuclei with non-integral spins the central transition can be observed and will be independent of the first order quadrupolar interaction.

When large quadrupolar interactions are present (second order perturbation), the central line is also shifted and the satellite transitions can be spread over a very wide frequency range so that they become unobservable. Only the central line $1/2 \leftrightarrow -1/2$ is normally presented in the resonance lineshape. The quadrupolar interactions in this case depend on $(9\cos^2\theta - 1)$.

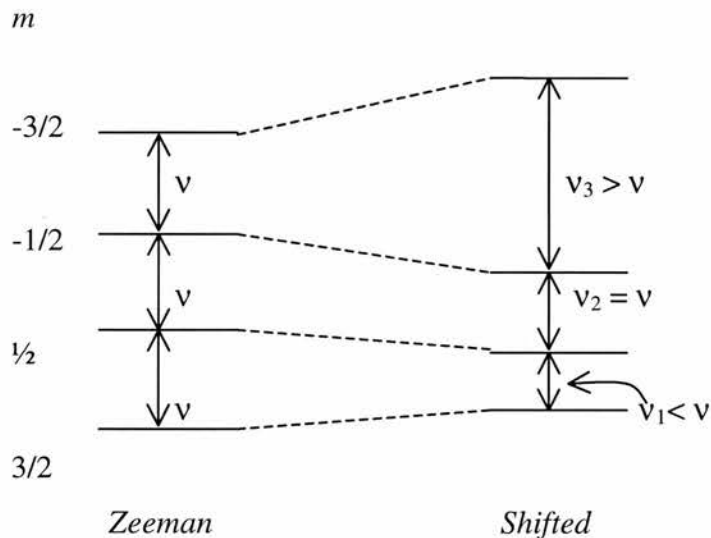


Fig.6.3. Shifts in Zeeman energy levels for a nucleus of spin $3/2$ (the shifts are exaggerated for clarity)

In a polycrystalline sample, eq. (6.13) must be averaged over all possible orientations. Due to this angular dependence, the resonance lines for powder samples are usually very broad.

Spin-lattice relaxation times in solids may be of the order of hours if quadrupolar effects are negligible. If the quadrupole effects are large, however, they may provide a very efficient relaxation mechanism, and T_1 as small as 10^{-4} s are found.

The electric field gradient may arise both from within a molecule (along a bond) and from its crystalline environment. It should be noted that the asymmetric distribution of electrons in the covalent bond gives rise to a large electric field gradient at the nucleus. Therefore, the intramolecular gradients cannot be reduced to zero, and broad lines are observed for covalently bonded quadrupolar nuclei even in solutions.

If the environment of the quadrupolar nucleus is sufficiently symmetrical, the electric field gradient will be zero at the nucleus, and the quadrupole coupling effects will be eliminated. Therefore it is possible to obtain good NMR signals for nuclei of large quadrupole moments when the nucleus is in cubic environment, e.g. in cubic crystals.

It is clear that some experimental difficulties can be encountered when observing NMR signals of quadrupolar nuclei in solids. Because of the short relaxation times (when quadrupole effects are large), some of the resonance may be lost in the dead-time between the pulse and the start of data acquisition. To overcome the problem of collecting data immediately after a pulse, echo sequences are normally employed to generate the spectrum.

Small quadrupolar interactions can be averaged by MAS since they have the angular dependence $(3\cos^2\theta - 1)$ (eq.6.13). More often, however, these interactions are very strong and no longer dependent on $(3\cos^2\theta - 1)$, therefore spinning at the magic angle fails to reduce the interactions down to zero.

6.2. ^7Li NMR STUDIES

6.2.1. Experimental details

NMR experiments were performed in a Bruker MSL500 spectrometer of magnetic field 11.75T in broad line or MAS probes. Variable temperature experiments were performed using a Bruker heating unit and the temperature was controlled by a thermocouple located near the sample. The samples were equilibrated for at least 30-40 min before every measurement. The signals were processed using an on-line dedicated Aspect3000 computer.

For broad line experiments, pieces of film or powder samples were placed in glass tubes which were sealed under Ar.

The MAS experiments were carried out in a Bruker multinuclear MAS probe. Each sample was ground to fine powder and then placed under Ar in zirconia rotor with plastic end cap. The spinning frequency was typically 4-8kHz and this was measured by a photo-sensitive detector.

FID signals were collected using one-pulse sequence 90° - *Acquire*. The pulse width was typically 2-3 μs since this was found to be the optimum 90° pulse width. The acquisition time was around 20ms. The signals were obtained by averaging 8-64 scans for each measurement. All linewidths reported are full widths at half-maximum. For linewidth measurements, the recycle delay time was chosen to be sufficiently long (20-30s) in order to observe the free induction decay for the slow relaxing components.

Spin-lattice relaxation times T_1 were measured by the standard saturation recovery technique. In this method, a "comb" of 90° pulses separated by a time delay τ was applied. The sequence was 90° - τ - 90° , pulse width was typically 2-3 μs , the acquisition time was 10-

20ms and the time delay τ was varied from 10ms to 40s. Each “comb” involved a series of 10 pulses. T_1 was determined by fitting the data to the equation:

$$M(\tau) = M(0)[1 - \exp(-\tau / T_1)] \quad (6.14)$$

where $M(0)$ is the intensity of the signal after saturation and $M(\tau)$ is the intensity of the signal obtained with time delay τ .

Proton decoupling experiments were performed for both FID and T_1 measurements. Data acquisition parameters were the same as above.

Some NMR characteristics of the two Li isotopes (^6Li and ^7Li) are listed in table 6.2.

	^6Li	^7Li
Nuclear spin quantum number, I	1	3/2
Natural abundance, %	7.42	92.58
Magnetic moment μ , in multiples of the nuclear magneton $eh/4\pi M_c$	0.82191	3.2560
Quadrupole moment Q , in multiples of $e \times 10^{-24} \text{cm}^2$	4.6×10^{-4}	-4.2×10^{-2}
Resonance frequency at 11.7T, MHz	73.578	194.317
Receptivity	6.31×10^{-4}	0.27

Table 6.2. NMR characteristics of the two Li isotopes

^7Li was the nucleus of choice in this work because of its larger natural abundance and larger magnetic moment. Due to these characteristics, the ^7Li isotope shows very good relative sensitivity. The relative sensitivity of ^6Li is much lower. However, better resolution can be achieved because of the smaller quadrupole moment.

6.2.2. ^7Li NMR studies of 6:1 crystalline complexes

6.2.2a. General considerations

The present work was involved with ^7Li NMR studies of several crystalline polymer – salt complexes of composition 6:1. These complexes ($\text{PEO}_6\text{:LiXF}_6$, $\text{X} = \text{P, As, Sb}$) were prepared with polymers of different molecular weight. The experimental data show that the NMR behaviour depends strongly on the molecular weight of the complexes; the influence of the different anions (PF_6^- , AsF_6^- or SbF_6^-) is less significant. In the case of the high-molecular weight complexes, the NMR behaviour was complicated due to the co-existence of crystalline and amorphous phase. It is impossible to obtain highly crystalline materials with the high molecular weight polymers and the samples normally contain 5-10% fraction of amorphous phase. This fraction of amorphous phase, however, has significant contribution to the overall response in the NMR experiments and makes the interpretation of the data difficult and uncertain in most cases. Therefore, the experimental results obtained for the high molecular weight complexes are not discussed in detail in this work. Summary of the most important results and some comments are given in Appendix III and IV.

The discussion in this Chapter is focussed mainly on the ^7Li NMR results for the highly crystalline 6:1 complexes of low molecular weight ($M_w = 1,000$). The interest in these complexes is determined by their high ionic conductivity as discussed in Chapter 5. Therefore it was of particular relevance to perform detailed NMR investigation of these materials in order to understand the mechanisms which govern the ion transport processes.

6.2.2b. ^7Li studies of crystalline 6:1 complexes of $M_w = 1,000$

Two crystalline 6:1 complexes of $M_w = 1,000$ have been studied: $\text{PEG}_6\text{:LiPF}_6$ and $\text{PEG}_6\text{:LiSbF}_6$. The experimental data for these complexes are very similar and the results are discussed in parallel.

Analysis of line shape and its temperature dependence

The ^7Li line has been examined in the temperature range 260 – 315K and the results are shown in fig. 6.4. Significant line narrowing is observed for both complexes. The line narrowing is more pronounced for the complex $\text{PEG}_6\text{:LiPF}_6$ than for $\text{PEG}_6\text{:LiSbF}_6$. This difference may result from slightly different dipolar or quadrupolar interactions which determine the linewidth (e.g. different Li – H distances).

For a nucleus of spin $I = 3/2$ (such as ^7Li) and small quadrupolar interactions, the resonance lineshape should consist of a central line associated with the central $1/2 \leftrightarrow -1/2$ transition and satellite lines which are associated with quadrupole transitions $\pm 3/2 \leftrightarrow \pm 1/2$ (as shown in fig. 6.3). In the present experiments, no satellite lines were observed. The proton decoupling experiments (discussed later) gave evidence that the outer (broad) components of the ^7Li line are due to dipolar Li – H interaction and do not represent satellite transitions. In addition, a nutation experiment was carried out in which the pulse width was varied from 1 μs to 10 μs . This experiment confirmed that the quadrupolar interactions do not influence the growth of the signal, and therefore the lineshape is determined only by dipolar effects.

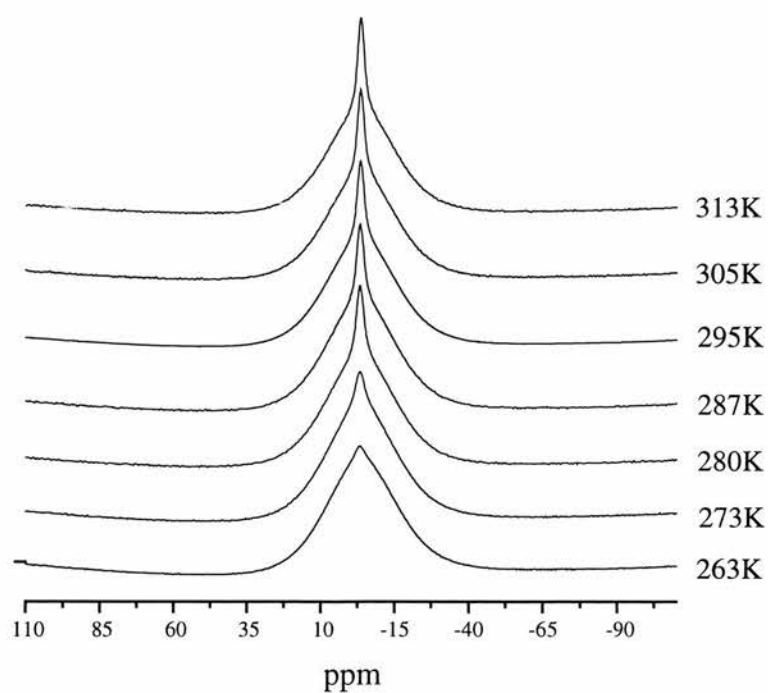
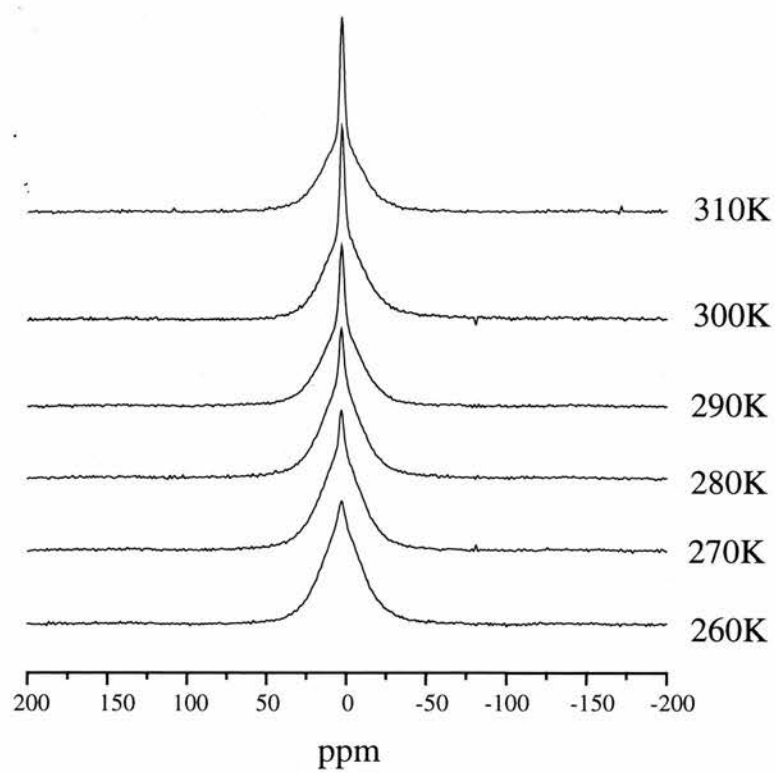


Fig.6.4. Temperature variation of the static ^7Li line for the complexes $\text{PEG}_6:\text{LiPF}_6$ (above) and $\text{PEG}_6:\text{LiSbF}_6$ (below)

The absence of satellite lines in the lineshape in this case may be due to the central line becoming very intense and narrow, so that the satellite lines become very weak (insignificant) and unobservable. These results show that the observed line narrowing is due to averaging of the dipolar interactions responsible for the width of the central line. Such averaging of the dipolar interactions may commence when the rate of fluctuations of the local dipolar fields due to ionic or molecular motion is comparable to the respective rigid lattice linewidth. The results suggest that there is significant increase in the Li ion mobility as the temperature increases.

An important feature for both complexes is the presence of two components in the lineshape in the whole temperature range and this suggests the presence of two different Li sites. These composite lines can be very well fitted to a sum of two Gaussians (or one Gaussian and one Lorentzian). The narrowing of the composite line is related to narrowing of both components.

The proportion between the integrated areas of the two components was calculated on the basis of the room-temperature spectrum in which the two components of the line can be well resolved. The double-Gaussian fit of the room-temperature spectrum shows that at room temperature ~20% of the ^7Li nuclei occupy the site which gives rise to the narrow line in the spectrum and the remaining 80% of the ^7Li nuclei occupy the site which gives the broad component. It should be noted that the room-temperature spectra used in these calculations were collected using very short pulse width (1 μs). In this way, the observed integrated areas are directly related to the number of nuclei giving rise to the individual lines and therefore quantitative estimations can be made. This is particularly important for the quadrupolar nuclei such as ^7Li in which case the integrated areas may not be true representation of the number of nuclei if longer pulse widths are being used. Also, the recycle delay time was chosen to be sufficiently long (40s) in order to observe the free induction decay of the slowly relaxing broad component.

Contributions to the linewidth (MAS and proton decoupling experiments)

MAS and proton decoupling experiments were performed in order to understand the contributions to the ^7Li line and the appearance of two components in the spectra. The proton decoupling experiments produced significant changes in the spectra, as shown in fig.6.5.

It can be seen that the effect of the proton decoupling is to reduce the linewidth of the broad component in the spectrum while the linewidth of the narrow component does not appear to be influenced by the Li-H dipolar interactions. Although Fig.6.5 represents the room temperature data, the same results were obtained in the whole temperature range under investigation. These results suggest the presence of two different lithium environments which arise from different proton co-ordination of the lithium sites.

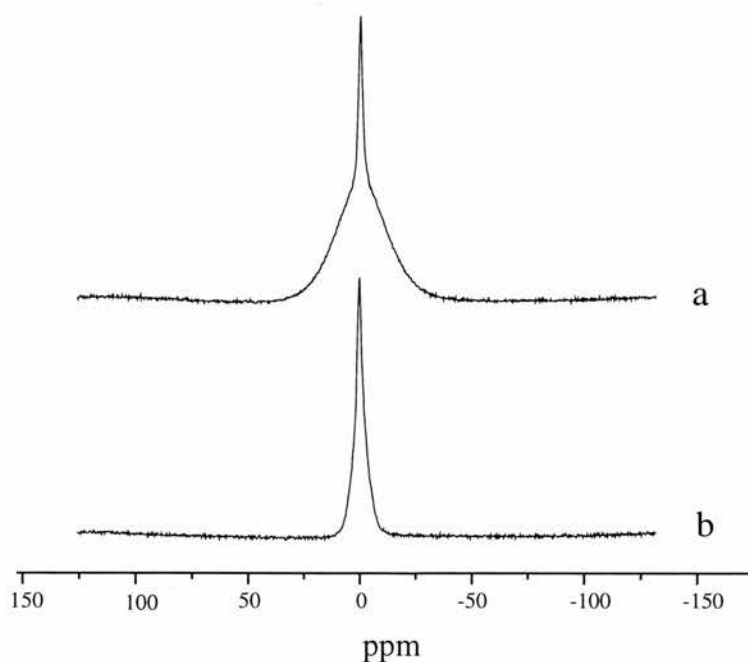


Fig.6.5. Static ^7Li spectra for the complex $\text{PEG}_6\text{:LiSbF}_6$ at room temperature: a) without proton decoupling, b) with proton decoupling

MAS experiments combined with proton decoupling were performed in order to achieve better resolution and observe more accurately the ^7Li chemical shifts (fig.6.6). In these experiments, the linewidth was reduced to 125Hz at spin rate 5kHz. With this resolution, only one line was observed in the spectrum. This is an indication that all Li nuclei reside in equivalent chemical environment, i.e. the Li – O co-ordination is equivalent for all lithium sites. In general, the observation of only one line in the MAS spectrum may also be due to rapid exchange between different environments. The line in this case would have a chemical shift which represents the average of the chemical shifts of the individual environments. The data in this work, however, show that there is no rapid exchange between different sites. Therefore, the observation of only one line in the MAS spectrum confirms the single-phase nature of the compounds under investigation.

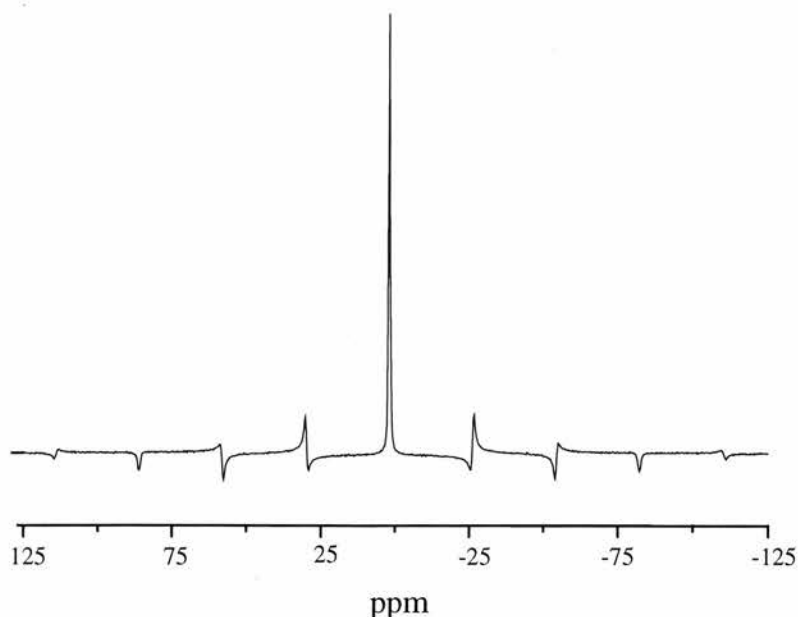


Fig.6.6. ^7Li MAS spectrum with proton decoupling for the complex $\text{PEG}_6\cdot\text{LiSbF}_6$

It should be noted here that the polymer used in the preparation of these samples is methoxy- ($\text{CH}_3\text{-O-}$)—ended and, because of its low-molecular weight, the fraction of CH_3 groups in these materials cannot be neglected. Therefore some Li atoms will be co-ordinated by oxygens from the groups $\text{-CH}_2\text{-O-CH}_2\text{-}$ and some Li atoms will be co-ordinated by oxygens from the groups $\text{-CH}_2\text{-O-CH}_3$. In other words, fraction of Li atoms will occupy “defect” sites which are adjacent to the -O-CH_3 groups from the chain ends. For the complexes of molecular weight 1,000, the calculations show that 10 - 20% of all Li atoms occupy these defect sites. Precise calculations cannot be made because the polymers are polydisperse and there is a distribution of molecular weights (polymer chain lengths). In addition, the distribution of “defect” Li sites may not be regular, i.e. some “defect” Li atoms may be coordinated to oxygens from four chain ends (-O-CH_3) and other “defect” Li sites may be coordinated to oxygens from only two chain ends. However, even with this low accuracy, the numbers agree very well with the calculations from the NMR data (as discussed earlier).

These results suggest that the ^7Li lineshape observed in the present experiments may be related to the defect structure of the low-molecular weight complexes. Since these defect sites involve mainly Li and hydrogen atoms, they can not be detected in the X-ray diffraction studies. However, the existence of such defects will influence significantly the lineshape and the relaxation in the NMR experiments.

Spin-lattice relaxation measurements

Spin-lattice relaxation measurements were performed in different modes, including data acquisition for static samples and MAS experiments.

The experiments with static samples confirmed the appearance of two Li sites (fig.6.7). The spin-lattice relaxation could be well described by a sum of two exponentials. The difference between the two relaxation times was about an order of magnitude at all temperatures and therefore the two relaxation rates could be well separated. The results from the double-exponential fit are plotted in fig.6.8. The data demonstrate that the magnetisation relaxes with two characteristic time constants (T_1' and T_1'') which differ in their temperature dependence.

It should be noted that deviations from a single exponential can arise from the ^7Li quadrupole moment. It has been shown [26] that for a quadrupolar relaxation mechanism involving nuclei of spin $I = 3/2$ or $I = 5/2$ in non-cubic environment, and under certain initial condition, the recovery of magnetisation to its equilibrium value is not a single exponential function of time but it is described by a superposition of two or more exponentials. In general, for quadrupolar relaxation mechanisms for nuclei of spin $I = 3/2$ or $I = 5/2$, in samples with non-cubic environments, single exponential spin-lattice processes are the exception rather than the rule. For example, if the initial “comb” of pulses completely equalises the populations of the four spin levels of a nucleus of spin $I = 3/2$, the signal associated with the central $1/2 \leftrightarrow -1/2$ transition has the form:

$$M(t) = M_0[1 + \exp(-2W_1T) - 2\exp(-2W_2t)] \quad (6.15)$$

where W_1 and W_2 are the probabilities for the $\Delta m_I = \pm 1$ and $\Delta m_I = \pm 2$ transitions due to the quadrupolar interactions.

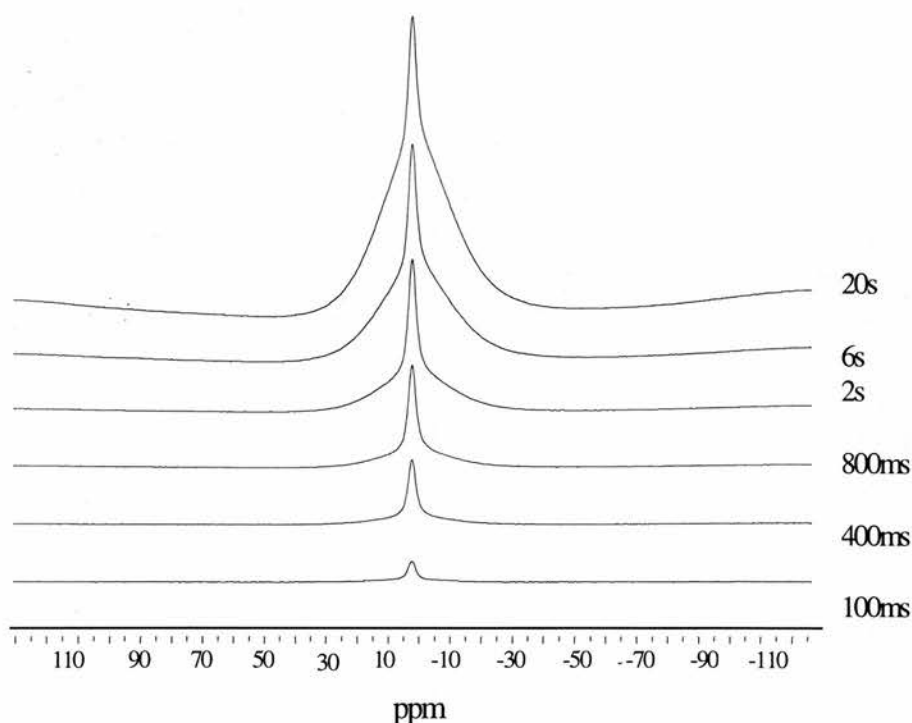


Fig.6.7. ^7Li spin-lattice relaxation for the crystalline complex $\text{PEG}_6\text{:LiSbF}_6$ at room temperature using saturation recovery technique with static sample. The delay time is indicated for each spectrum. Only 6 (of total 12) lines are shown for clarity.

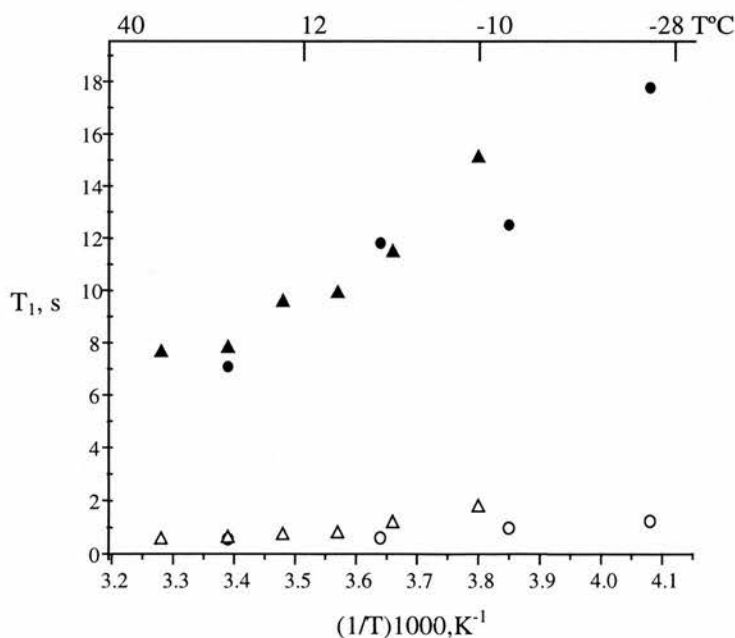


Fig.6.8. Temperature variation of the two spin-lattice relaxation times for the complexes $\text{PEG}_6\text{:LiPF}_6$ (circles) and $\text{PEG}_6\text{:LiSbF}_6$ (triangles). Solid symbols represent the longer relaxation times (T_1') and open symbols represent the shorter relaxation times (T_1'').

In the present work, it is assumed that the double exponential recovery of the magnetisation is due to the occurrence of two different relaxation processes for several reasons. Several NMR studies of polymer electrolytes containing Li salt have found that the ^7Li spin-lattice relaxation can be well described by a single exponential in non-cubic or disordered phases [16, 22, 27, 28]. In the case of polymer electrolytes containing Na salts, double exponential fits have been used to relate the corresponding relaxation rates to the transport processes [14, 29]. Most importantly, the results from the static NMR experiments in the present work show that there are two different Li environments which are likely to be associated with two different relaxation processes. Therefore the results from the double exponential fit of the magnetic relaxation (shown in fig.6.8) can be related to the corresponding physical processes.

Spin-lattice relaxation time measurements were also performed using MAS combined with proton decoupling. An example of spin-lattice relaxation in these experiments is shown in fig.6.9. A single line is observed at all delay times. The spin-lattice relaxation in this case can be relatively well described by a single exponential. The spin-lattice relaxation time at room temperature is 8.90s which is close to the spin-lattice relaxation time T_1' measured for the slow-relaxing (broad) component in the static experiments. It is possible, however, that the shorter spin-lattice relaxation time T_1'' is not so obvious since MAS narrows dramatically the broad component of the spectrum so that the peak amplitude is determined almost completely by the amplitude of this slow-relaxing component. In this case the amplitude of the narrow component does not change significantly and it occupies only a very small fraction of the total peak amplitude. Under these conditions, the shorter relaxation time T_1'' can become unobservable in the double exponential fit.

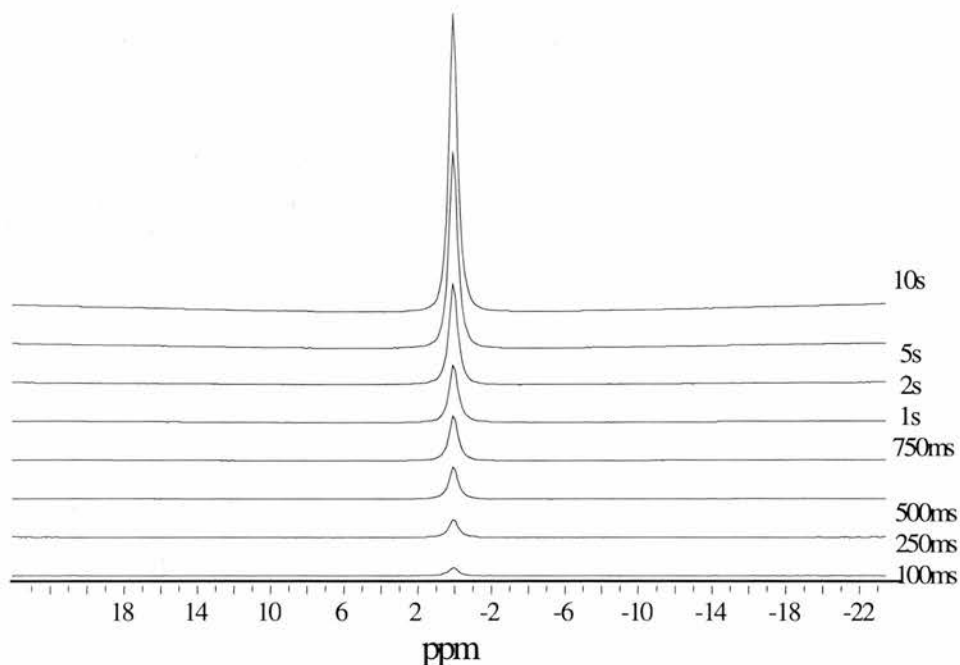


Fig.6.9. ^7Li spin-lattice relaxation for the crystalline complex $\text{PEG}_6:\text{LiSbF}_6$ at room temperature using saturation recovery technique and MAS combined with proton decoupling. The delay time is indicated for each spectrum.

More detailed analysis of the spin-lattice relaxation measurements was attempted for the complex $\text{PEG}_6:\text{LiSbF}_6$ due to better data statistics. The experimental results for the other complex ($\text{PEG}_6:\text{LiPF}_6$) were very similar and therefore the conclusions made for $\text{PEG}_6:\text{LiSbF}_6$ by implication should apply also for $\text{PEG}_6:\text{LiPF}_6$.

The two spin-lattice relaxation times (T_1' and T_1'') at each temperature were calculated by fitting the magnetic relaxation to a sum of two exponentials. The Arrhenius plots $\ln T_1'$ (or $\ln T_1''$ respectively) vs. $1/T$ were then made and the activation energy for the two ion hopping processes were calculated. The activation energy for the process with longer relaxation time was found to be $0.14(\pm 0.01)\text{eV}$ and the activation energy for the process with shorter relaxation time was $0.23(\pm 0.02)\text{eV}$. It is clear that these values are much lower compared to

the values for E_a obtained from the conductivity measurements, in which case $E_a(\text{conductivity}) = 1.01\text{eV}$.

In order to relate each of the two relaxation processes to the broad or narrow component in the static spectra, each line in the room-temperature T_1 data (as shown in fig. 6.7) was fitted to a sum of two Gaussians. The two sets of data were then used to calculate separately the spin-lattice relaxation times for the broad or narrow component. In both cases, the relaxation could be described by a single exponential, and the relaxation times were found to be 7.68s for the broad component and 0.76s for the narrow component. These values compare very well with the values obtained after double-exponential fit for the same data (7.77s and 0.59s). The good agreement of the data obtained by two different and independent procedures shows that the obtained results are valid and may be used to model the processes responsible for the observed NMR behaviour.

It can be concluded that the lithium sites which give rise to the broad component in the static spectra have longer relaxation time and lower activation energy for ion hopping. The lithium sites which give the narrow component have shorter relaxation time, but higher activation energy for ion hopping. The analysis so far shows that the narrow line in the composite spectra arises from the “defect” lithium sites which are located close to the CH_3 – groups of the polymer chains. This assignment is also plausible because the CH_3 groups are involved in rapid re-orientational motion [43] and thus the dipolar Li – H interactions are averaged without spinning or decoupling. As a result, for the defect Li sites, the corresponding line in the static spectra is narrow and the spin-lattice relaxation time is very short. Also, the defect sites have higher activation energy for ion hopping as compared to the “regular” lithium sites. This can be attributed to stronger Li – H van der Waals’ interactions with the hydrogens from the CH_3 - groups as compared to the interactions with hydrogens from the regular CH_2 – groups.

Model for Li ion motion based on the NMR data

The NMR data obtained in the present work can be used to make a simple model of the Li ion motion (fig.6.10).

The Li atoms can occupy two different sites - A and B. Site A corresponds to the site which gives rise to the broad component in the static NMR spectra. Site B corresponds to the site which is associated with the narrow line in the static spectra. At room temperature, 10 – 20% of the Li atoms occupy site B and 80-90% occupy site A. The crystal structure of the 6:1 complexes suggests that Li ion motion occurs along one-dimensional tunnels, i.e. each Li site has only two neighbouring Li sites into which it can hop. The sites A and B differ in two ways: first, the activation energy for hopping is different in A and B and second, the mean residence time in A and B is different. The activation energy for hopping from site B ($\Delta E'' = 0.23\text{eV}$) is higher than the activation energy for hopping from site A ($\Delta E' = 0.14\text{eV}$). However, according to the spin-lattice relaxation data, the Li atoms reside in site A for longer time intervals as compared to site B.

It is obvious that since the complexes 6:1 are stoichiometric, all Li sites are occupied. Therefore, the probability for isolated ion hopping into a neighbouring site is negligible. However, several additional notes can be made here. Unoccupied Li sites can arise as a result of the formation of certain types of defects in the lattice, e.g. interstitial defects. Such defects can exist without deviation from the stoichiometry of the complexes. Also, going back to the crystal structure, in each 6:1 repeat unit there is one “spare” oxygen which does not coordinate lithium. This can result in effect similar to partial occupancy of the lithium sites. In all of these cases, the fraction of unoccupied Li sites will be very small but it can be sufficient to promote ion hopping. The Li ion hopping can also involve several neighbouring Li sites but not isolated jumps. It is very likely that ion motion actually occurs by means of cooperative ion migration.

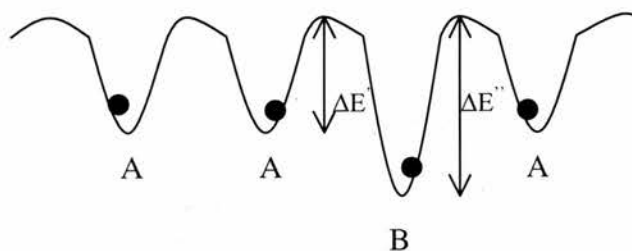


Fig.6.10. Schematic of Li ion motion in the crystalline 6:1 complexes

It can be suggested that the two Li sites appear as a result of the “defect” coordination of the Li atoms near the polymer chain ends. These “defect” sites, however, act as a “trap” for the Li ions since there is higher energy barrier on going back to the regular Li sites.

6.2.3. ^7Li studies of the amorphous complex $\text{PEO}_6\text{:LiSbF}_6$

Analysis of lineshape and its temperature dependence

The variation of the ^7Li line was studied in the temperature range 25 - 100°C (fig.6.11). The room temperature line is relatively broad (3400Hz) and this suggests that the lithium sites are involved in mainly static dipolar interactions. Significant line narrowing is observed at elevated temperatures which can be attributed to modulations of the Li – H dipolar interaction resulting from the polymer segmental motion. At lower temperatures (from room temperature up to 330K), the lines are composite and they cannot be described by a single Gaussian. In other NMR studies of amorphous polymer-salt complexes, these composite lines have been attributed to either different cation environments due to the presence of ion aggregates, or to the existence of more than one population of cations each with a different mobility [14, 27, 29, 31]. This issue is further discussed in the section on spin-lattice relaxation times measurements.

Above 350K, a single line is observed (500Hz) which can be fitted to a single Lorentzian line. The line does not narrow above this temperature which means that the high-temperature linewidth limit has been achieved. This is a common observation in linewidth studies of polymer electrolytes [27-29] and it has been attributed to rapid spin-lattice relaxation which introduces a lifetime broadening contribution to the total linewidth. These effects are very pronounced in the Na-polymer electrolytes in particular, and may result in broadening of the line at high temperatures.

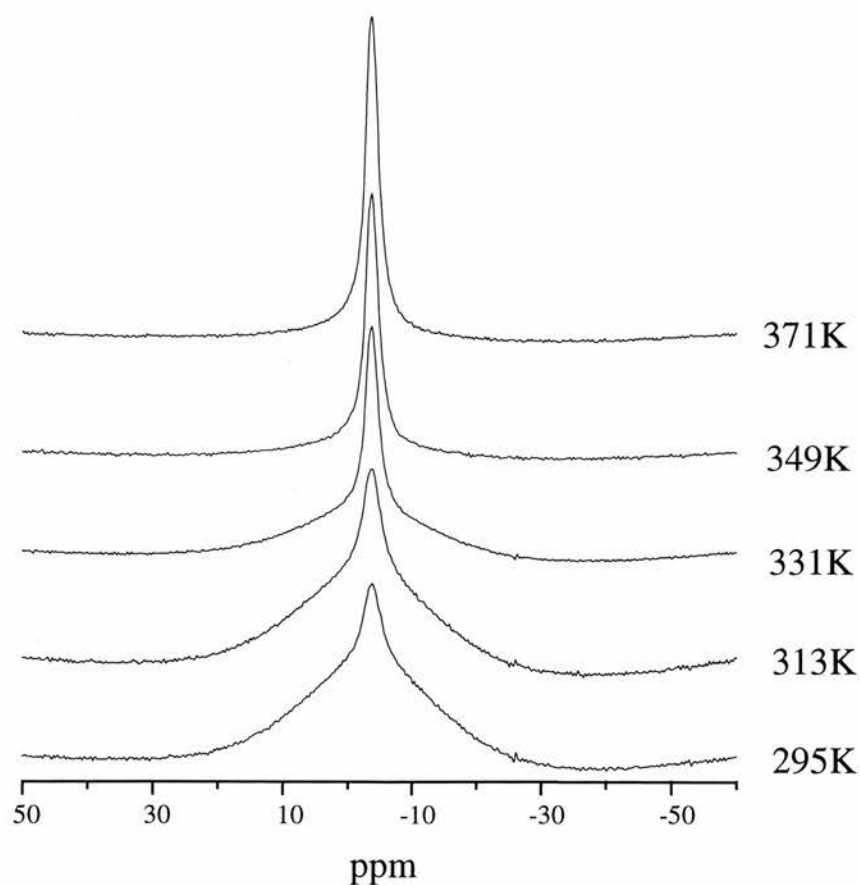


Fig.6.11. Temperature variation of the ^7Li line for the amorphous complex $\text{PEO}_6\text{:LiSbF}_6$ in static NMR experiments

In the present experiments, the high-temperature limit of the linewidth may be explained as follows: the total linewidth W can be represented as a sum of two terms $W_1 + W_2$. W_1 is related to the temperature dependent dipolar interactions which cause narrowing of the line at all temperatures. The second term W_2 is related to the chemical shift anisotropy or inhomogeneity and it is temperature independent. Therefore, above certain temperatures, the total linewidth can reach constant values depending on the relative contributions of W_1 and W_2 .

Contributions to the ^7Li line

Proton decoupling experiments were performed in order to study the influence of the Li – H dipolar interactions on the ^7Li line. The data are summarised in fig.6.12 and table.6.3. As seen, the Li – H interaction has significant contribution to the ^7Li line at room temperature since ~56% reduction in the linewidth is observed. At higher temperatures, however, the contribution of the Li – H coupling is less significant which indicates that these dipolar interactions have been already averaged due to the increased mobility of the Li sites.

The comparison of the spectra collected with or without proton decoupling (fig.6.12) shows that multicomponent lines are observed in both cases. These multicomponent lines suggest the presence of various species, or a distribution of Li – O environments associated with the amorphous complex.

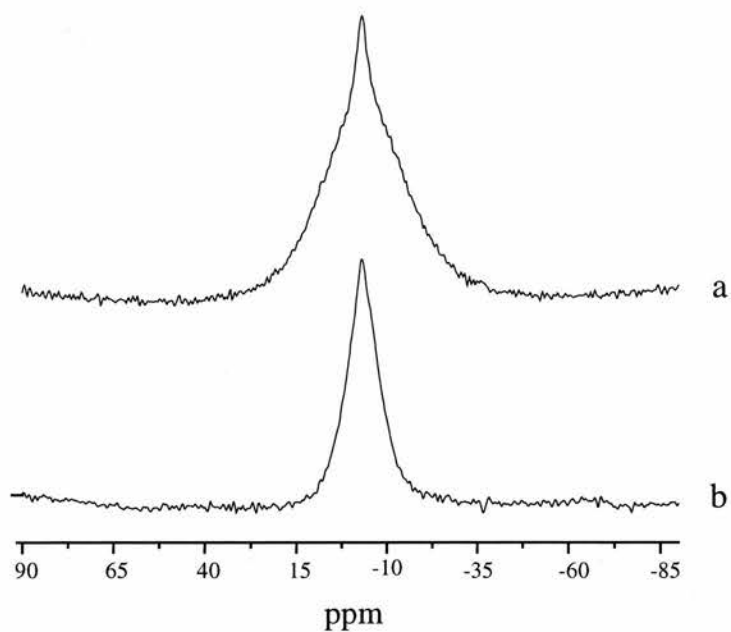


Fig.6.12. Static ^7Li line at room temperature for the amorphous complex $\text{PEO}_6\text{:LiSbF}_6$: a)without proton decoupling, b)with proton decoupling

T, °C	T, K	Static linewidth, Hz	Static linewidth with proton decoupling Hz
22	295	3400	1900
32	305	3000	1800
41	314	2300	1750
49	322	1500	1500

Table 6.3. ^7Li linewidths for the amorphous complex $\text{PEO}_6\text{:LiSbF}_6$

Spin-lattice relaxation time (T_1) measurements

T_1 measurements were made in the temperature range 22 - 98°C. In all cases, the relaxation could be well described by a sum of two exponentials, i.e. the magnetisation was found to relax with two different time constants. The results are listed in table 6.4 where T_1' denotes the longer relaxation time and T_1'' denotes the shorter relaxation time. At all temperatures, the difference between the two relaxation times is significant and therefore the two time constants can be easily resolved.

T, °C	T, K	T_1' , s	T_1'' , s
22	295	11.89	0.58
40	313	9.22	0.47
58	331	3.94	0.23
76	349	0.52	0.004
98	371	0.50	0.003

Table 6.4. Spin-lattice relaxation times for the amorphous complex $PEO_6:LiSbF_6$

An example is given in fig.6.13 which represents the results from a saturation recovery experiment used for T_1 measurements. The data in fig.6.13 are collected at 58°C. The two components can be clearly seen – the spin-lattice relaxation time for the narrow line (T_1') is ~229ms and the spin-lattice relaxation time for the broad line (T_1'') is more than an order of magnitude longer (~3.94s). The data in table 6.4 show that the temperature variation is more significant for the short spin-lattice relaxation time (T_1'') which changes by factor of ~200 in the temperature interval under study. The longer spin-lattice relaxation time (T_1') changes only by factor of ~24 in the same temperature range.

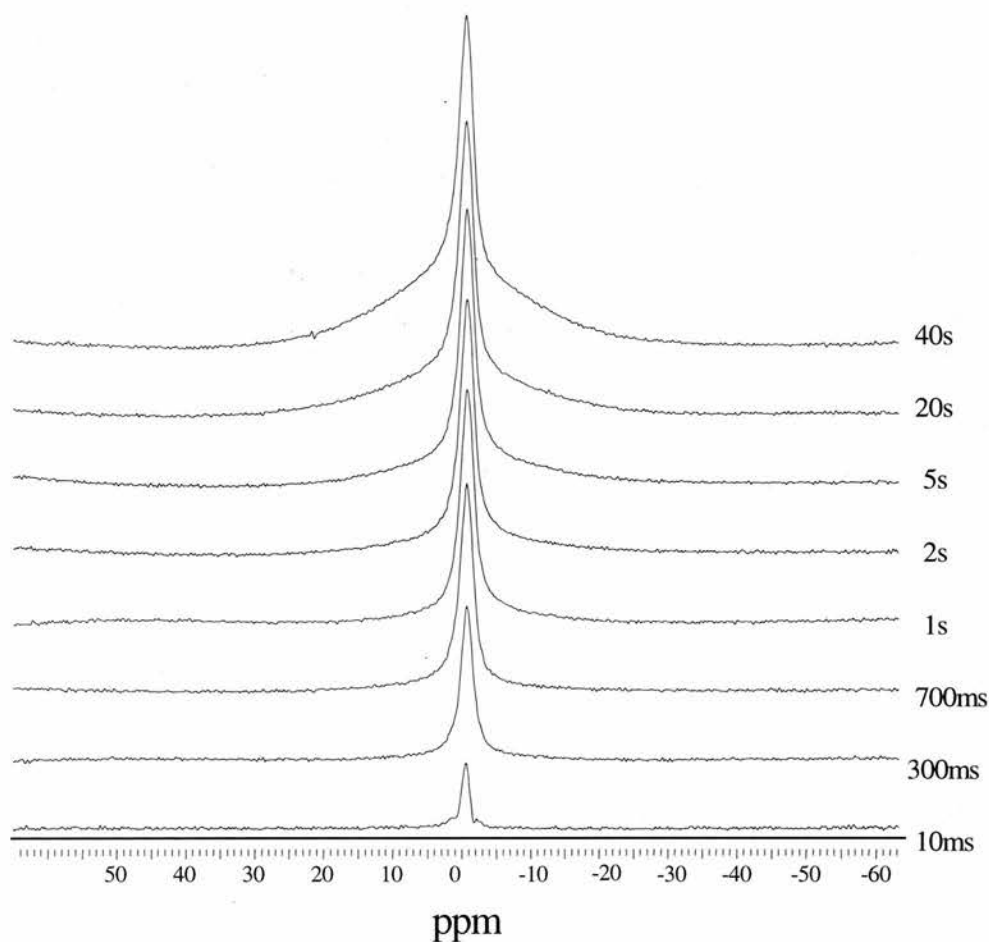


Fig. 6.13. Static ^7Li spin-lattice relaxation spectra for the amorphous complex $\text{PEO}_6:\text{LiSbF}_6$ at 58°C using the saturation recovery technique. The delay time is indicated for each spectrum.

Similar results have been obtained in NMR studies of amorphous polymer-salt complexes based on sodium salts. In some cases [14], the observation of two different spin-lattice relaxation times has been attributed to the existence of two different species – dissociated cations (shorter relaxation time) and cation – anion pairs (longer relaxation times). In other studies [29, 31], the interpretation is slightly different since the narrow component (short T_1) is attributed to mobile cations and the broad component (longer T_1) is attributed to ionic clusters. In the present work, the presence of specific configurations (ion pairs or ion clusters) could not be established unambiguously but some speculations can be made. The proportion between the broad and the narrow component changes significantly with

temperature as clearly seen in fig.6.11. At room temperature, the spectrum consists mainly of the broad component while at the higher temperatures the later disappears and only a single narrow line is observed. The changes in the proportion between the two components may be an indication of temperature-dependent ion dissociation which results in increasing the number of free (mobile) ions. It should be noted that increase in the number of free ions would not necessarily result in proportional increase of ion mobility. Ion motion is controlled also by other factors such as rate of long-range segmental motion, free volume and other thermodynamic parameters.

6.2.4. Conclusions from the ^7Li NMR studies

The ^7Li NMR studies provided important information in terms of local environment of the lithium sites and their dynamics. As a whole, the NMR data are in agreement with the crystal structure and conductivity studies and, at the same time, they make it possible to further understand the structure and dynamics of the compounds under investigation.

The NMR results for the highly crystalline 6:1 complexes agree with the crystal structure studies since they confirm that all Li sites are involved in equivalent chemical environment in terms of Li – O coordination. This is evidenced by the observation of a single line in the high resolution MAS experiments with proton decoupling. Also, the NMR results for the highly crystalline 6:1 complexes give evidence for strong interactions between the Li sites and the polymer chain. Cation – anion (Li – F) interactions are found to be insignificant. The chemical shifts for these complexes measured in the MAS experiments relative to 1M LiCl aqueous solution were slight and probably insignificant. The similar shift values obtained from the reference and from the samples demonstrate that in both cases the Li nuclei are involved in similar ionic configuration.

The relation between the NMR and the conductivity measurements is not straightforward and similar issues have been addressed in several reviews on NMR studies of solid ionic conductors [8, 9, 12, 27, 32]. The principal difficulty is to relate the NMR parameters to long range motion as distinct from short range motion. NMR is sensitive to localised motion since the dominant relaxation mechanisms, such as dipole-dipole or quadrupolar interactions, are short range. Therefore NMR is sensitive to local motional processes which are not necessarily related to the long range transport mechanisms which determine the conductivity. It should be noted that diffusion coefficients can be measured directly in favourable circumstances by the pulse field gradient method. This technique, however, can be used to study relatively fast diffusion in solids and it has not been applied in the present work.

Variable-temperature linewidth measurements give evidence for significant motional narrowing of the ^7Li line for the amorphous complex $\text{PEO}_6:\text{LiSbF}_6$ and the low-molecular weight 6:1 complexes. The results from the static experiments and the spin-lattice relaxation time measurements for these complexes are remarkably similar. However, analysis of the lineshape performed by MAS and proton decoupling experiments shows that the relaxation mechanisms responsible for the observed line narrowing are not the same and therefore the microscopic physical processes which contribute to the line narrowing may be radically different. The ^7Li results on the low-molecular weight complexes are influenced very strongly by the presence of CH_3^- groups in the samples. The observed data are close to these that can be theoretically predicted for such Li environment. In the high molecular weight amorphous complex, CH_3^- groups are present in insignificant amount, along with OH^- end groups. Because of the very long chain lengths in the high-molecular weight polymer, these end groups would not in practice effect the ^7Li NMR behaviour. Therefore the observed lineshape and relaxation behaviour in the amorphous complex originate from completely different processes as compared to the low-molecular weight 6:1 crystalline complexes.

Although the NMR data give evidence for Li ion mobility, it may be necessary to perform further studies in order to understand the dynamics in these polymer electrolytes and to relate the NMR data to the long-range transport processes observed in the conductivity studies. The application of high-resolution methods, e.g. ^6Li NMR with MAS and proton decoupling may provide more information on the local environment of the Li sites in the different complexes. This may help to understand the role of the different Li sites in the transport processes. More systematic studies of the relaxation rates may also be necessary in order to understand whether the relaxation behaviour in these systems follows the BPP model, or whether there are some deviations which can be related to the mechanism of the transport processes.

6.3. NMR STUDIES OF THE ANION STRUCTURE AND DYNAMICS

6.3.1. Experimental considerations

The anion structure and dynamics were probed by means of ^{31}P , ^{75}As and ^{121}Sb NMR spectroscopy. The ^{75}As and ^{121}Sb nuclei possess similar NMR characteristics and the experimental data are very similar. Therefore the results from these studies are discussed in parallel. The results from the ^{31}P experiments are discussed separately.

^{75}As and ^{121}Sb NMR

These nuclei possess unfavourable NMR characteristics (table 6.5) and so far they have not been employed in NMR studies of polymer electrolytes. However, several solid state ^{121}Sb NMR studies have been reported [33, 34] and these were involved with examining magnetic materials at low temperatures.

Arsenic has only one NMR active nucleus – ^{75}As (100% natural abundance). Antimony has two active nuclei – ^{121}Sb and ^{123}Sb . The receptivity of ^{121}Sb is more favourable and its quadrupole moment is slightly smaller than in the case of ^{123}Sb . Thus ^{121}Sb is normally the nucleus of choice for NMR experiments.

All of the above nuclei possess moderate nuclear quadrupole moments and relaxation is dominated by the efficient quadrupolar mechanism. Therefore, when these nuclei are at low-symmetry sites, the resonance can be extremely broad.

	⁷⁵ As	¹²¹ Sb	¹²³ Sb
Nuclear spin quantum number, <i>I</i>	3/2	5/2	7/2
Natural abundance, %	100	57.25	42.75
Magnetic moment μ , in multiples of the nuclear magneton $eh/4\pi M_c$	1.4349	3.3417	2.5334
Quadrupole moment <i>Q</i> , in multiples of $e \times 10^{-24} \text{ cm}^2$	0.3	-0.8	-1.0
Resonance frequency at 11.7T	85.634	119.652	64.796
Receptivity	2.51×10^{-2}	9.16×10^{-2}	1.95×10^{-2}

Table 6.5. NMR characteristics of the As and Sb isotopes

It has been shown in chapter 6.1.6. that the quadrupolar interactions may provide very efficient relaxation mechanism and T_1 can be very short. Therefore some of the resonance may be lost in the dead-time between the pulse and the start of data acquisition. To overcome this problem, the spin-echo sequence developed by Hahn [35] was employed in the present experiments. The sequence is $90^\circ - \tau - 180^\circ - \tau - \text{Acquire}$ and the effect of the two pulses is as follows: The first pulse tips the nuclear magnetisation through 90° . As a result of the small steady gradient of the external magnetic field, the individual magnetisations from nuclei in different locations within the sample start to lose their phase coherence. The second pulse rotates the magnetisation by 180° so that the individual magnetisations rephase, causing a spin-echo signal of amplitude $A(2\tau)$ at time 2τ , where τ is the time interval between the two pulses.

In the present experiments, the pulse width was typically $3\mu\text{s}$, and the time interval τ between the pulses was $50\mu\text{s}$. The recycle delay time was varied from 0.1s to 10s but this did not produce differences in the spectra. Spectra were collected by averaging of about 4,000 –12,000 scans for each measurement.

³¹P NMR

³¹P is the only naturally occurring isotope of phosphorus. Some NMR characteristics of the ³¹P nucleus are listed in table 6.6. ³¹P gives rise to chemical shifts which extend over a range of ~500ppm and this provides an excellent means of determining the molecular structures of phosphorus containing compounds. This large range of chemical shifts allows one to achieve very high resolution despite the low NMR sensitivity of phosphorus (6.64% that of the ¹H nucleus at constant magnetic field).

FID measurements in the present work were made using a simple one-pulse sequence *90° - Acquire*. The pulse width was typically 2μs. The recycle delay time was 20s in the static experiments and 5s in the MAS experiments. The signals were obtained by averaging 8-32 scans for each measurement. Spin-lattice relaxation measurements were made using the standard saturation recovery technique as described in chapter 6.2.1. The delay time τ was varied between 100ms and 40s.

	³¹P
Nuclear spin quantum number, <i>I</i>	1/2
Natural abundance, %	100
Magnetic moment μ , in multiples of the nuclear magneton $eh/4\pi M_c$	1.1305
Quadrupole moment <i>Q</i> , in multiples of $e \times 10^{-24} \text{ cm}^{-2}$	-
Resonance frequency at 11.7T	202.403
Receptivity	6.64×10^{-2}

Table 6.6. NMR characteristics of the ³¹P isotope

6.3.2. ^{31}P studies of the crystalline complex $\text{PEG}_6\text{:LiPF}_6$

Variable-temperature linewidth measurements with static samples

Variable-temperature linewidth measurements were performed for the complex of $M_w = 1,000$ in the temperature range 263 – 305K. The experiments focussed on the low-molecular weight complex since this was found to support higher ionic conductivity as compared to the analogous high-molecular weight complexes. Also, the degree of crystallinity for the complex $\text{PEG}_6\text{:LiPF}_6$ ($M_w = 1,000$) was very good and therefore the complications arising from the co-existence of crystalline and amorphous material (which is the case for the high-molecular weight complexes) could be eliminated.

In the whole temperature range, the ^{31}P resonance was represented by a broad line ($\sim 4300\text{Hz}$) which could be described by a single Gaussian. The linewidth did not change in the temperature interval under study (263 – 305K). The lack of motional narrowing suggests that the ^{31}P nuclei are involved in mainly static magnetic interactions. However, the linewidth is probably influenced by rotation of the anion PF_6^- as a whole. For example, NMR studies of alkali hexafluorophosphates [36] have shown that the PF_6^- anion is re-orienting about the octahedral axes at random for temperatures of 200K and above.

High-resolution MAS and proton decoupling experiments

MAS experiments were made at spinning frequency $\sim 6\text{kHz}$ with or without proton decoupling (fig.6.14). Spectra were collected in the temperature range from 263 to 305K. At all temperatures, the ^{31}P resonance consisted of a septet pattern as could be expected for the coupling of six equivalent fluorines with one phosphorus (for one nucleus coupled to n equivalent nuclei, the number of lines in the pattern is given by $n+1$). The theoretical intensity distribution in the pattern is 1:6:15:20:15:6:1 and this agrees very well with the experimental spectrum in fig.6.14.

The lines in the septet are separated uniformly by $\sim 710\text{Hz}$ and this is a typical value for spin-spin coupling J_{PF} in the PF_6^- anion [37].

The proton decoupling experiment resulted in narrowing of each of the seven lines in the pattern. This implies that the P – H dipolar interactions are mainly static. If there was translational diffusion of the anions PF_6^- as a whole, the dipolar P – H interactions would have been averaged by the motion and the proton decoupling would not effect the linewidth.

These results, in combination with the linewidth measurements of the static samples suggest that the anions PF_6^- are not involved in translational motion but there could be rapid tumbling about the center of the mass.

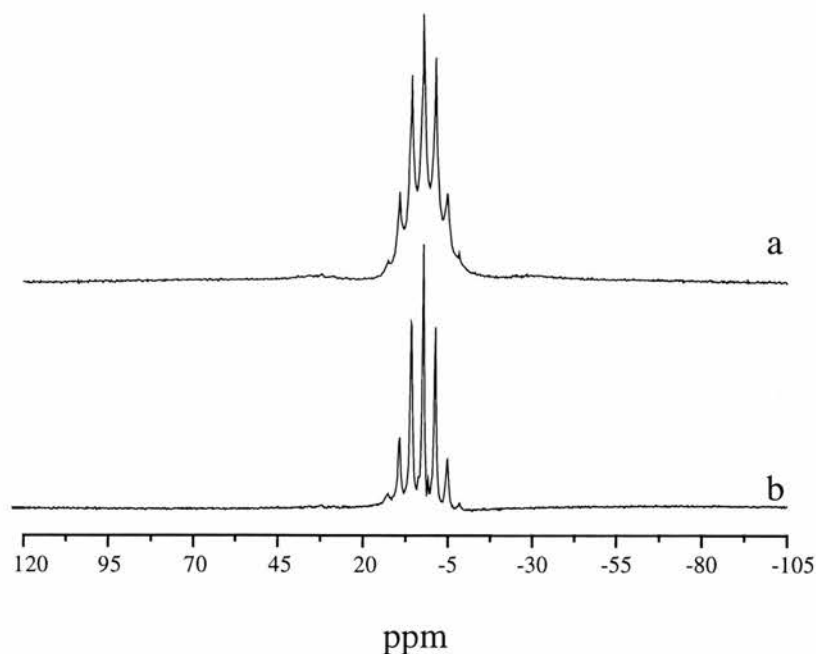


Fig.6.14. ^{31}P –MAS spectra for the complex $\text{PEG}_6\text{:LiPF}_6$ ($M_w = 1,000$) at room temperature: a) without proton decoupling, b) with proton decoupling

Spin-lattice relaxation time (T_1) measurements

The present work did not involve systematic ^{31}P spin-lattice relaxation time measurements. Measurements at room temperature show that the relaxation can be well described by a single exponential. Only the characteristic septet pattern was observed at all delay times. These results confirm the single-phase nature of the compounds under study. T_1 at room temperature is 3.8s.

6.3.3. ^{75}As and ^{121}Sb studies of crystalline 6:1 complexes

Two crystalline 6:1 complexes have been studied – $\text{PEO}_6\text{:LiAsF}_6$ and $\text{PEO}_6\text{:LiSbF}_6$. The complex $\text{PEO}_6\text{:LiSbF}_6$ was prepared with polymers of different molecular weight ($M_w = 100,000$, 2,000 and 1,000) but no differences were observed between the samples of different molecular weight.

Temperature dependence of the linewidth

The temperature variation of the ^{75}As line for the complex $\text{PEO}_6\text{:LiAsF}_6$ ($M_w = 100,000$) was studied in the temperature range 195 – 414K (fig.6.15). Very broad resonance line (~90kHz) was observed at all temperatures below the melting point. The line narrowed dramatically on heating above the melting temperature. Even above the melting point, the pattern had the features of a quadrupolar-split line.

Similar results were obtained for the complex $\text{PEO}_6\text{:LiSbF}_6$. However, this complex was studied over a limited temperature range due to its poor thermal stability. Again, the resonance line was very broad (~100kHz) and it did not change on heating above room temperature.

As noted in Chapter 6.1.6, the resonance lines of quadrupole nuclei are very sensitive to the chemical environment and symmetry of the site. The lineshape observed in the present experiments suggests that the nuclei ^{75}As and ^{121}Sb reside in low-symmetry sites but not in symmetric cubic environment. In contrast, sharp ^{75}As line was observed for the pure salt LiAsF_6 . These results show that the regular coordination of the anions AsF_6^- is significantly distorted after the process of complex formation.

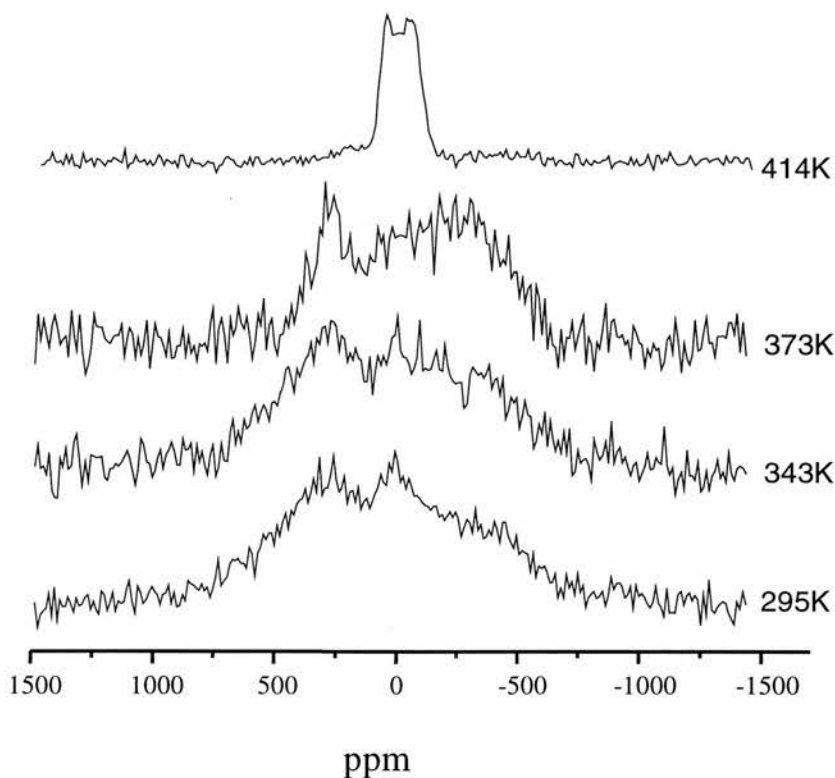


Fig.6.22. Temperature variation of the ^{75}As line for the complex $\text{PEO}_6:\text{LiAsF}_6$ in a static NMR experiment

The resonance lineshape observed in the present experiments below the melting temperature (fig.6.15) is very close to the lineshape one would expect for a nucleus of spin $I = 3/2$ with small quadrupole interaction in a polycrystalline sample. In this case three transitions are possible. These are the central transition $1/2 \leftrightarrow -1/2$ which gives rise to the central line in the spectrum, and the outer transitions $\pm 1/2 \leftrightarrow \pm 3/2$ which give rise to the satellite lines in the spectrum. From the static ^{75}As and ^{121}Sb spectra, the quadrupole coupling constant may be derived $Q = (e^2qQ/h) = 180\text{kHz}$ for both complexes $\text{PEO}_6\text{:LiAsF}_6$ and $\text{PEO}_6\text{:LiSbF}_6$ at room temperature.

The broad resonance lines described above can also be attributed to the interactions of the nuclear quadrupole magnetic moment with the fluctuating electric field gradient caused by rotational or translational motion of the anion AsF_6^- (SbF_6^-). Such motions would provide efficient relaxation mechanism and make the spin-lattice relaxation time T_1 very short. This then causes lifetime broadening, and washes out the structure of the NMR line.

To further understand the source of line broadening, the complex $\text{PEG}_6\text{:LiSbF}_6$ ($M_w = 1,000$) was studied at low (sub-ambient) temperatures (fig.6.16). When this complex was cooled down, the line narrowed significantly. This is a further indication of continuous freezing of the motion which is mainly responsible for the observed line broadening at higher temperatures. As seen in fig.6.16, the motion is still not completely frozen at 180K. Since the possibility for diffusion at this temperature can be ruled out (taking into account the conductivity data discussed in Chapter 5), the main source of line broadening could be the rapid tumbling (rotation) of the anion SbF_6^- . This rotational motion is temperature dependent and therefore at sufficiently high temperatures it can make T_1 very short and, correspondingly, result in very broad resonance lines.

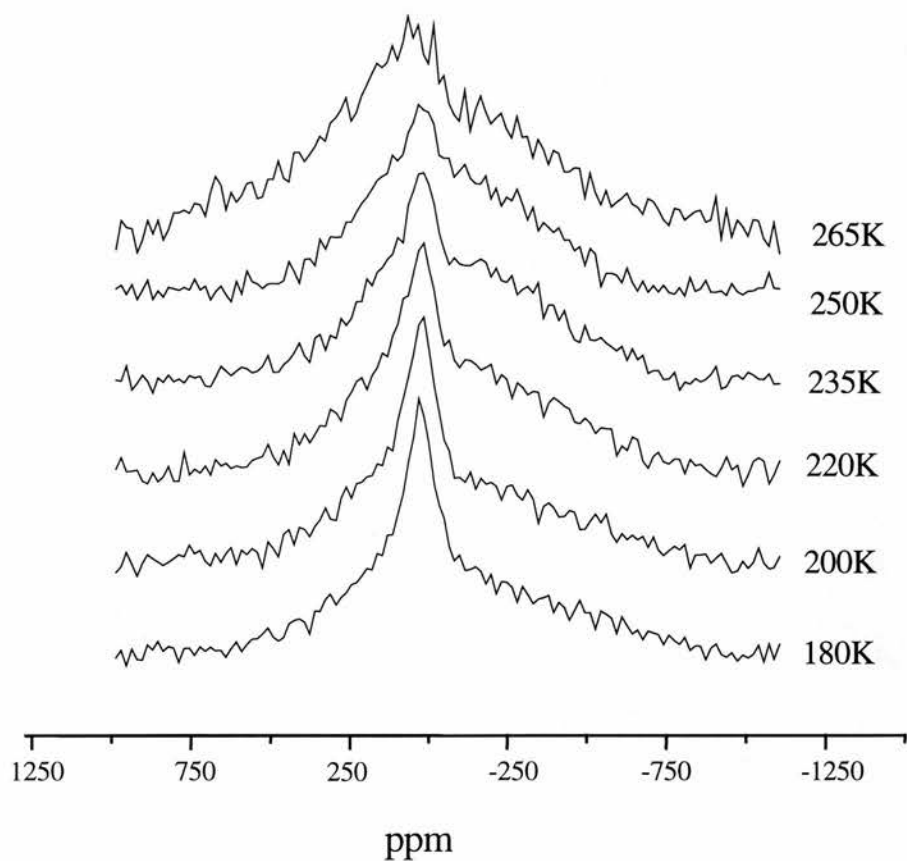


Fig.6.23. Temperature variation of the ^{121}Sb line for the complex $\text{PEG}_6\text{:LiSbF}_6$ ($M_w = 1,000$) in a static NMR experiments. Spectra collected above 265K are the same as at 265K and they are not shown.

The low-temperature experimental data also show that the line broadening above room temperature is not related to static disorder of the Sb sites. If this was the case, the low-temperatures would not produce such variations in the lineshape.

Spin-lattice relaxation time (T_1) measurements

Spin-lattice relaxation time measurements were made for the complex $\text{PEG}_6\text{:LiSbF}_6$ ($M_w = 1,000$) at several temperatures. Even at the lowest temperature (180K), the spin-lattice relaxation was very fast ($T_1 < 5\text{ms}$) and T_1 could not be estimated.

6.3.4. ^{121}Sb studies of the amorphous complex $\text{PEO}_6\text{:LiSbF}_6$

Analysis of lineshape and its temperature dependence

Variable-temperature measurements of the ^{121}Sb line were made in the temperature range 295 – 363K (fig.6.17). It can be seen that the resonance lineshape is very different from the lineshape observed for the crystalline complexes. The room temperature spectrum for the amorphous complex consists of two components – a very broad line of linewidth $\sim 100\text{kHz}$ and a narrow line of width $\sim 25\text{kHz}$. This interpretation of the pattern is supported by the following two observations: first, two-component lines were also observed in the ^7Li spectra, and second, spin-lattice relaxation time measurements on the amorphous complex suggest that the magnetic relaxation occurs by means of two different relaxation processes (as discussed later in this section). Therefore, it is assumed here that the resonance lineshape shown in fig.6.17 is associated with the superposition of two resonance lines, rather than with a typical spectrum resulting from first-order quadrupolar effects.

The variable temperature measurements of the lineshape show that there is narrowing of the total line at elevated temperatures which is associated with narrowing of the broad component. The width of the broad component changes from $\sim 100\text{kHz}$ at room temperature to $\sim 65\text{kHz}$ at 363K. The narrowing of the broad line is related to increasing the amplitude of the signal which overlaps significantly with the narrow line at elevated temperatures. Therefore, the variations of the narrow line cannot be clearly seen. It should be noted here that the intensities of the signals shown in fig.6.17 do not represent the true relative intensities at each temperature and should not be used to compare the intensity of the signal at different temperatures. The lines can be used only to describe qualitatively the lineshape at different temperatures.

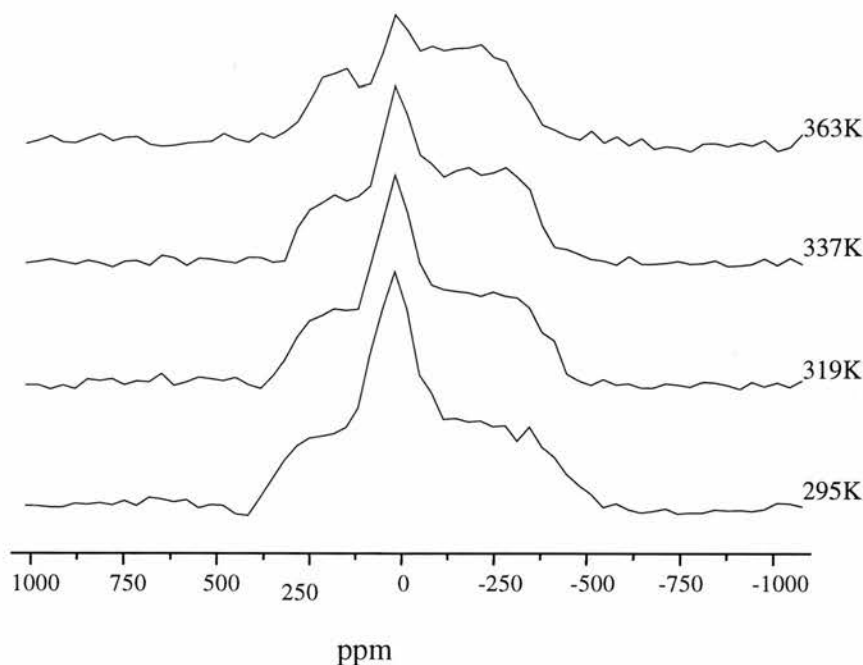


Fig.6.17. Temperature variation of the ^{121}Sb line for the amorphous complex $\text{PEO}_6:\text{LiSbF}_6$ (static sample)

According to the discussion of the ^7Li data for the amorphous complex $\text{PEO}_6\text{:LiSbF}_6$ (Chapter 6.2.3), there are two different environments – ion aggregates and free (mobile) ions. Following this line, the broad component in the ^{121}Sb lineshape can be attributed to ^{121}Sb nuclei in ion aggregates (clusters) and the narrow line can be attributed to ^{121}Sb nuclei in free (mobile) anions SbF_6^- . However, it is impossible to make quantitative interpretation of the ^{121}Sb data due to the very broad resonance lines. It is very likely that some fraction of the signal is lost in the dead-time between the pulse and the start of the data acquisition. Then the actual width of the broad component and, correspondingly, its area may be significantly larger than the observed ones. Therefore any calculations based on the integrated areas of the components in the spectra will lose their physical meaning.

Spin-lattice relaxation time (T_1) measurements

T_1 measurements were performed only at room temperature. Again, the data suggest the presence of two different environments for the ^{121}Sb nuclei which are associated with two very different time scales for magnetic relaxation. The broad component of the ^{121}Sb signal was saturated even at the shortest delay times (5ms). The spin-lattice relaxation time for the narrow line, however, was longer (300-400ms) and in this case the recovery of the magnetisation could be seen very well. The results suggest that the relaxation of the broad component is dominated by the quadrupolar effects. The relaxation of the narrow component, however, may be associated with other relaxation mechanisms (dipolar interactions or ionic motion).

6.3.5. Conclusions from the NMR studies of the anion structure and dynamics

The experimental data on the anion structure and dynamics are rather limited and further work is needed in order to make definite conclusions. Some initial conclusions, however, can be noted.

Considering the motional processes in the crystalline 6:1 complexes, no evidence for translational diffusion of the anions XF_6^- ($\text{X} = \text{P}, \text{As}, \text{Sb}$) has been found. However, these anions are most probably involved in rapid rotational processes even at low (sub-ambient) temperatures. This rotation is about the centre of the mass of the anion and does not contribute to a long range motion of the anion as a whole. The rapid tumbling of the anions XF_6^- ($\text{X} = \text{P}, \text{As}, \text{Sb}$) mainly determines the lineshape and the relaxation of the nuclei ^{31}P , ^{75}As and ^{121}Sb in the crystalline complexes.

The interpretation of the results for the amorphous complex $\text{PEO}_6\text{:LiSbF}_6$ is complicated because of the limited data. Therefore, the discussion in Chapter 6.3.4 includes mainly suggestions but not definite conclusions. There have been some experimental difficulties with collecting NMR data on this complex since the sensitivity of the nucleus ^{121}Sb is low, thus necessitating long times for data acquisition. At the same time, because of the transformation of the amorphous complex to a crystalline phase with time, the measurements need to be done quickly to ensure that the data represent the NMR behaviour of the amorphous phase. As a whole, the ^{121}Sb data for the amorphous complex are in agreement with the ^7Li data which suggest that at room temperature a significant fraction of ions is present as ion aggregates/clusters. The increased

ion mobility at elevated temperatures is due to thermal dissociation and, consequently, increased number of free charge carries.

To understand better the structure and dynamics of the anions XF_6^- ($\text{X} = \text{P}, \text{As}, \text{Sb}$) in the complexes under investigation, it is necessary to perform further studies including more detailed sub-ambient lineshape and spin-lattice relaxation measurements, proton-decoupling experiments on all samples, MAS experiments, etc.

6.4. NMR studies of chain mobility (^1H and ^{13}C NMR)

6.4.1. ^1H and ^{13}C NMR as a probe of the polymer structure and dynamics in polymer electrolytes

^1H and ^{13}C NMR spectroscopy has long been employed in observing the structure, morphology and molecular motions in polymers. In the area of polymer electrolytes, ^1H NMR studies have been mainly involved with examining the spin-lattice relaxation behaviour at various temperatures, with the aim of establishing the correlation between the ion mobility and the polymer chain mobility [12, 16, 17, 38, 39]. Also, ^1H NMR spectroscopy has been applied to deduce the amounts of crystalline and amorphous phases in polymer electrolytes at different temperatures. The estimation of the relative amounts of nuclei belonging to the different phases is based on the difference in the time scales of the free induction decay for the nuclei in the crystalline and amorphous phase [13, 40].

Only a few ^{13}C NMR studies of polymer electrolytes have been reported [38, 41, 42]. The lack of more extensive ^{13}C studies is mainly due to the very complex problems presented by the polymer electrolytes and difficulties in interpreting the data.

6.4.2. Results and discussion

General considerations

The present work was involved with a limited number of ^{13}C and ^1H experiments and therefore the experimental results are not discussed in detail. However, several notes on the main problems encountered in these studies can be made.

The ^{13}C data on the crystalline 6:1 complexes were different for the complexes of different molecular weight. In the case of the high molecular weight complexes, the

experimental results were very similar to these reported in the literature for other polymer electrolyte systems [41, 42]. In the temperature interval 295 – 360K, the ^{13}C MAS spectrum consists of two components – a narrow line which can be associated with any residual amorphous phase and a broad line which is attributed to the crystalline complex. At all temperatures, the narrow line is shifted to lower frequencies as compared to the broad line. Similar shifts have been observed for pure PEO [42].

The ^{13}C MAS spectra for the low molecular weight 6:1 complexes ($M_w = 1,000$) also consist of two lines. However, the narrow line in this case is shifted to the higher frequencies. The chemical shifts of the lines suggest that the broad line can be attributed to ^{13}C nuclei in the $-\text{CH}_2-$ groups and the narrow line can be attributed to ^{13}C nuclei in the $-\text{CH}_3$ end groups. Since the $-\text{CH}_3$ groups are involved in rapid re-orientational motion even at very low (sub-ambient) temperatures [4, 30], the corresponding line in the spectrum at room temperature is very narrow. Cross-polarisation MAS experiments also suggest that the narrow line in the ^{13}C spectra of the low molecular weight 6:1 complexes ($M_w = 1,000$) is related to the presence of $-\text{CH}_3$ groups in these materials.

As a whole, the interpretation of the ^{13}C data is very difficult and this requires additional experimental data in order to understand the polymer chain structure and dynamics. Further experiments, including variable temperature spin-lattice relaxation time measurements and cross-polarisation MAS may be very useful for the assignment of the lines in the spectra and for understanding the role of the polymer chains in the motional processes in the materials under investigation.

¹H linewidth studies of the amorphous complex PEO₆:LiSbF₆

In this work, ¹H linewidth measurements were carried out in order to examine the polymer segmental motion in the amorphous complex PEO₆:LiSbF₆ at various temperatures. These measurements provide information on the temperature of onset of the polymer segmental motion thus allowing one to determine the glass transition temperature of amorphous systems. At the onset of the chain motion, the dipolar interactions begin to average and therefore the corresponding line narrows. Similar approach has been used before [43] and it has been shown that T_g obtained through NMR and DSC measurements is similar. In general, the NMR measurements yield lower T_g temperature and this difference is attributable to the large difference between the heating rates in the NMR and DSC methods.

Free induction decay measurements were performed in the temperature range 220 ÷ 290K (fig.6.18). Line narrowing commences at around 240K which gives the glass transition temperature. The line narrows dramatically above this temperature due to averaging of the dipolar interactions responsible for the linewidth. As already noted, averaging of the dipolar interactions occurs because of the motion of the polymer chains.

In general, the ¹H resonance line could not be described by a single Gaussian. Similar observations have been made for other amorphous polymer electrolytes [43, 44]. It has been shown that, at high molecular weight polymers, the transverse relaxation function (the FID) is non-exponential and reflects a complex dynamics. In the entanglement regime, the dynamics are characterised by two sets of chain relaxation times: the longest relaxation times are associated with long-range disentanglement processes and the short relaxation times are associated with short segmental motions within submolecules, i.e. the entangled parts of the chain.

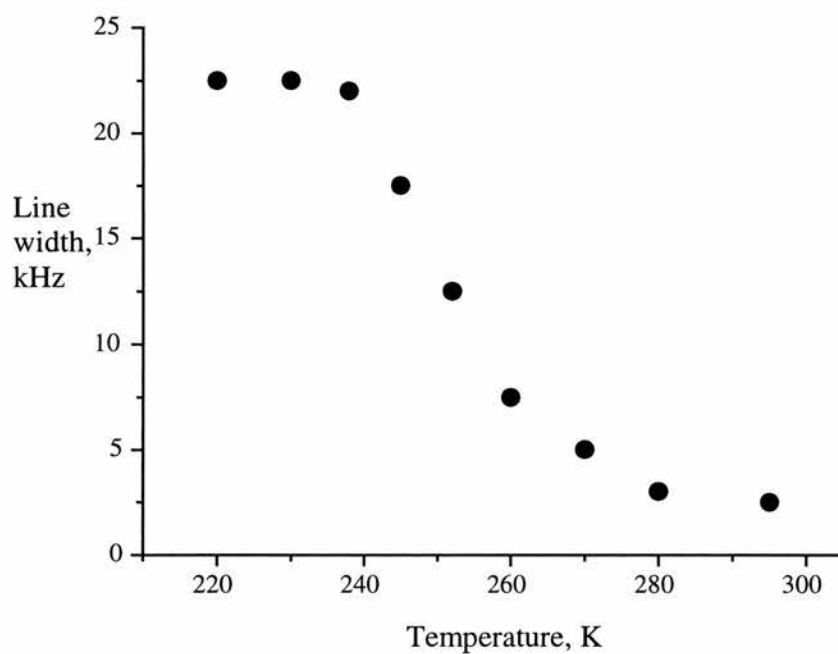


Fig.6.18. ^1H linewidth as a function of temperature for the amorphous complex $\text{PEO}_6:\text{LiSbF}_6$

The present work did not involve detailed study of the spin-spin or spin-lattice relaxation. However, it was shown that the amorphous complex is not a glass above 240K and hence all data collected above this temperature reflect the properties of an amorphous material.

6.5. REFERENCES

1. A.V. Chadwick and M.R. Worboy, in *Polymer Electrolyte Reviews*, ed. by J.R. MacCallum and C.A. Vincent, Elsevier Science Publishers Ltd., 1989
2. J. Sanders and B. Hunter, *Modern NMR Spectroscopy*, Oxford University Press, 1993
3. J.M. Hollas, *Modern Spectroscopy*, J. Wiley & Sons, 1992
4. R.J. Abraham and P. Loftus, *Proton and Carbon-13 NMR Spectroscopy*, Heyden & Son Ltd, 1978
5. J.W. Emsley, J. Feeney and L.H. Sutcliffe, *High Resolution NMR Spectroscopy*, Pergamon Press, 1965
6. C.A. Fyfe, *Solid State NMR for Chemists*, C.F.C. Press, 1983
7. N. Bloembergen, E.M. Purcell and R.V. Pound, *Phys. Rev.*, **73**, 679 (1948)
8. D. Brinkmann, *Solid State Ionics*, **5**, 53 (1981)
9. D. Brinkmann, *Progr. in Nucl. Magn. Res. Sp.*, **24**, 527 (1992)
10. W. Schirmacher and A. Schirmer, *Solid State Ionics*, **28/30**, 134 (1988)
11. D. Brinkmann, *Mag. Res. Rev.*, **14**, 101 (1989)
12. S.G. Greenbaum, *Solid State Ionics*, **15**, 259 (1985)
13. F.L. Tanzella, W. Bailey, D. Frydrych, G. Farrington and H.S. Story, *Solid State Ionics*, **5**, 681 (1981)
14. S. Schantz, M. Kakihana and M. Sandberg, *Solid State Ionics*, **40/41**, 645 (1990)
15. Y.S. Pak, K.J. Adamic, S.G. Greenbaum, M.C. Wintergill, J.J. Fontanella and C.S. Coughlin, *Solid State Ionics*, **45**, 277 (1991)
16. W. Gorecki, E. Belorizky, C. Berthier, P. Donoso and M. Armand, *Electrochim. Acta*, **37**, No9, 1685 (1992)
17. A. Johanson, A. Wendsjo and J. Tegenfeldt, *Electrochim. Acta*, **37**, No9, 1487 (1992)

18. M.C.Wintergill, J.J.Fontanella, J.P.Calame, M.K.Smith, T.B.Jones, S.G.Greenbaum, K.J.Adamic, A.N.Shetty and C.G.Andeen, *Solid State Ionics*, **18/19**, 326 (1986)
19. S.Arumagam, J.Shi, D.Tunstall and C.A.Vincent, *J.Phyc.C*, **5**, 153 (1993)
20. S.H.Chung, Y.Wang, S.G.Greenbaum, D.Golonitsky and E.Peled, *Electrochem.and Solid St.Lett.*, **2 (11)** 553 (1999)
21. Y.Dai, S.Greenbaum, D.Golodnitsky, G.Ardel, E.Strauss, E.Peled, Yu.Rosenberg, *Solid State Ionics*, **106**, 25 (1998)
22. J.P.Donoso, T.J.Bonagamba, H.C.Panepucci, L.N.Oliveira, W.Gorecki, C.Berthier, M.Armand, *J.Chem.Phys.*, **98 (12)**, 10026 (1993)
23. W.Schirmacher and A.Schirmer, *Solid State Ionics*, **28-30**, 134 (1988)
24. W.Gorecki, M.Jeannin, E. Belorizky, C.Roux and M.Armand, *J.Phys., Condens.Matter* **7**, 6823 (1995)
25. S.D.Brown, S.G.Greenbaum, M.G.McLin, M.C.Wintersgill and J.J.Fontanella, *Solid State Ionics*, **67**, 257 (1994)
26. E.R.Andrew and D.P.Tunstall, *Proc.Phys.Soc.*, **78**, 1 (1961)
27. S.H.Chung, K.R.Jeffrey and J.R.Stevens, *J.Chem.Phys.*, **94(3)**, 1803 (1991)
28. S.Panero, B.Scrosati and S.G.Greenbaum, *Electrochim.Acta*, **7**, No.9, 1533 (1992)
29. S.G.Greenbaum, Y.S.Pak, M.C.Wintergill, J.J.Fonatanella, J.W.Schultz and C.G.Andeen, *J.Electrochem.Soc.*, **135**, No.1, 235 (1988)
30. J.G.Powles, *Polymer*, **1**, 219 (1960)
31. S.G.Greenbaum, Y.S.Pak, M.C.Wintergill, J.J.Fonatanella, *Solid State Ionics*, **31**, 241 (1998)
32. J.B.Boyce and B.A.Huberman, *Physics Reports*, **51**, No.4, 189 (1979)
33. K.Hashi, A.Oyamada, S.Maegawa, T.Goto, D.X. Li, T.Suzuki, A.Donni and F.Hulliger, *Physica B*, **261**, 159 (1999)
34. A.Oyamada, K.Hashi, S.Maegawa, T.Goto, D.X.Li, T.Suzuki, A.Donni and F.Hulliger, *Physica B*, **199**, 42 (1994)
35. E.L.Hahn, *Phys.Rev.*, **80**, 580 (1950)

36. G.R.Miller and H.S.Gutowsky, *J.Chem.Phys.*, **39**, No8, 1983 (1963)
37. G.R.Miller, H.A.Resing, F.L.Vogel, A.Pron, T.C.Wu and D.Billaud, *J.Phys.Chem.*, **84**, No25, 3333 (1980)
38. A.Johansson and J.Tegenfeldt, *Macromolecules*, **25**, No18 (1992)
39. A.Johansson and J.Tegenfeldt, *J.Chem.Phys.*, **104**, 5317 (1996)
40. C.Berthier, W.Gorecki, M.Minier, M.B.Armand, J.M.Chabagno and P.Rigand, *Solid State Ionics*, **11**, 91 (1983)
41. L.J.M.Sawers, D.P.Tunstall and P.G.Bruce, *Solid State Ionics*, **107**, 13 (1998)
42. S.Schantz and S.L.Maunu, *Macromolecules*, **27**, 6915 (1994)
43. C.Roux, W.Gorecki, J.-Y.Sanchez, M.Jeannin and E.Beloritzky, *J.Phys.Condens.Matter*, **8**, 7005 (1996)
44. I.M.Ward, N.Boden, J.Cruickshank and S.A.Leng, *Electrochim.Acta*, **40**, No13-14, 2071 (1995)

CHAPTER 7

**CONCLUSIONS:
MECHANISM OF IONIC CONDUCTION
IN STOICHIOMETRIC POLYMER ELECTROLYTES**

7.1. Summary of the experimental evidence for ionic transport in stoichiometric polymer electrolytes

The crystal structures of the stoichiometric 6:1 complexes suggest that Li ion transport is possible in the crystalline phase. The Li ions in these compounds are located within tunnels formed by pairs of PEO chains. The anions are located outside these tunnels in the interchain space and do not coordinate the cations.

To investigate the potential for ionic conductivity, crystalline and amorphous 6:1 complexes were examined. In this way, ion transport in the crystalline and amorphous phase above T_g could be directly compared. The experimental results can be summarised in two

main points that are related to the levels of conductivity and the ion transport numbers in the materials under investigation.

Levels of ionic conductivity

The variation of the ionic conductivity as a function of temperature (discussed in Chapter 5, fig.5.4) shows that the highly crystalline 6:1 complexes may exhibit higher levels of conductivity than the analogous amorphous systems above T_g . A summary of the experimental data is given in fig.7.1 in which the ionic conductivity of the crystalline complex $\text{PEG}_6\cdot\text{LiSbF}_6$ is compared to the ionic conductivity of the amorphous complex of the same composition. The temperature range in fig.7.1 includes the conductivity data above T_g (for the amorphous complex), and below the decomposition temperature (for both complexes). It is evident that the ionic conductivity in the crystalline phase is higher than in the amorphous phase even above T_g . At the lowest temperatures, the crystalline phase reaches a conductivity more than one order of magnitude higher than the amorphous phase.

These experimental results suggest that ionic conductivity is more favoured in the static environment of the crystalline phase. The high levels of ionic conductivity in the crystalline 6:1 complexes is most probably related to their distinctive structures which define permanent pathways for ion migration. In contrast, ion transport in the dynamic environment of the amorphous phase appears to be more limited. Ion motion in this case requires suitable coordination sites that are created at random as a result of the segmental motion of the polymer chains. These segmental modes involve the motion of group of atoms on the polymer chain and are relatively slow. Therefore the hopping rates and the ionic conductivity are usually more limited.

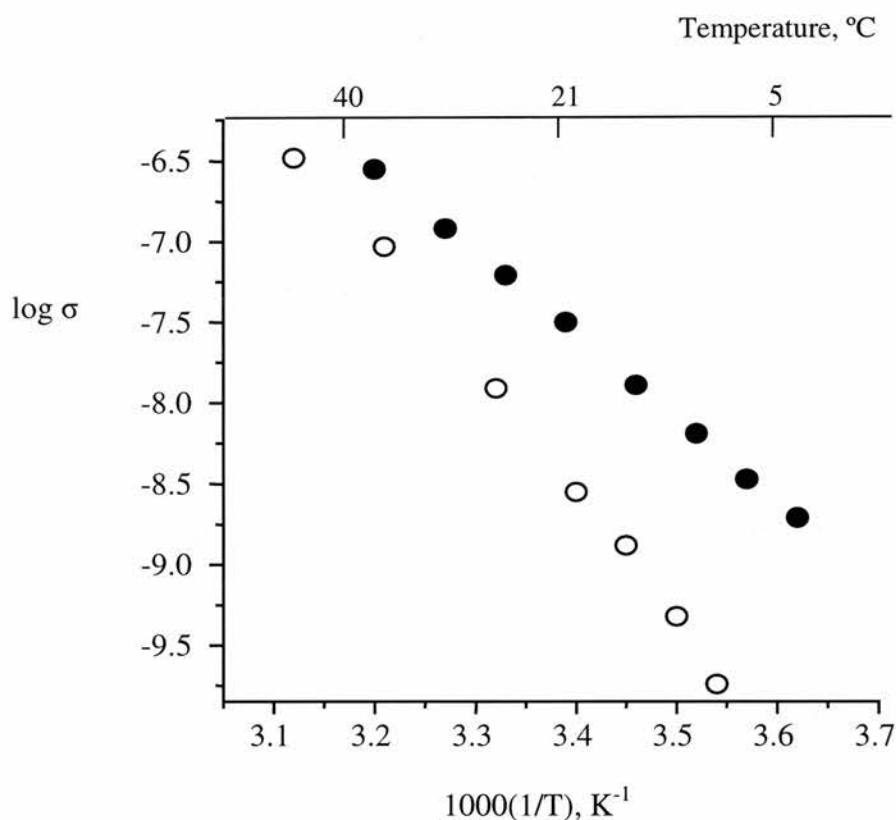


Fig.7.1. Total ionic conductivity of crystalline (solid circles) and amorphous (open circles) $\text{PEO}_6\text{:LiSbF}_6$ as a function of temperature

Highest levels of ionic conductivity were observed in the highly crystalline, low molecular weight polymer electrolytes where from the widths of the peaks in the X-ray data, the size of the crystalline regions is greater than in the case for the high molecular weight polymer. This is further support for the view that ion transport is more favoured in the more organised and ordered phases. It has been shown in the present work that high molecular weight crystalline electrolytes of reduced crystallite dimensions exhibit inferior conducting properties.

Transport numbers

The cation and anion transport numbers were investigated by NMR spectroscopy. The contribution of Li ion motion to the overall conductivity could not be studied by means of electrochemical techniques due to poor stability of the electrolytes vs. lithium metal electrodes that were employed in the present study.

Motional narrowing of the ^7Li line with temperature was observed for all highly crystalline 6:1 complexes. The anion motion was mainly examined for the low molecular weight complex $\text{PEO}_6\text{:LiPF}_6$ since ^{31}P is a spin $\frac{1}{2}$ nucleus, unlike ^{121}Sb and ^{75}As . This rendered ^{31}P more advantageous for monitoring the anion motion. The ^{121}Sb and ^{75}As NMR data, however, are in agreement with the ^{31}P data and therefore the conclusions on the anion motion are valid for all complexes.

Fig.7.2 shows the variation of linewidth over the temperature range 260 – 310K for ^7Li and ^{31}P . The ^7Li line narrows significantly whereas the width of the ^{31}P line remains constant with temperature. In addition, the proton decoupling experiments on ^{31}P demonstrate that the phosphorus atoms are involved in mainly static interactions with the hydrogens from the polymer, i.e. there is no translational motion of the anion PF_6^- as a whole with respect to the polymer chains. Combining the NMR results with those from the measurements of the total ionic conductivity demonstrates that the ionic conductivity is dominated by Li^+ motion, i.e. the cation transport number T_+ is close to unity.

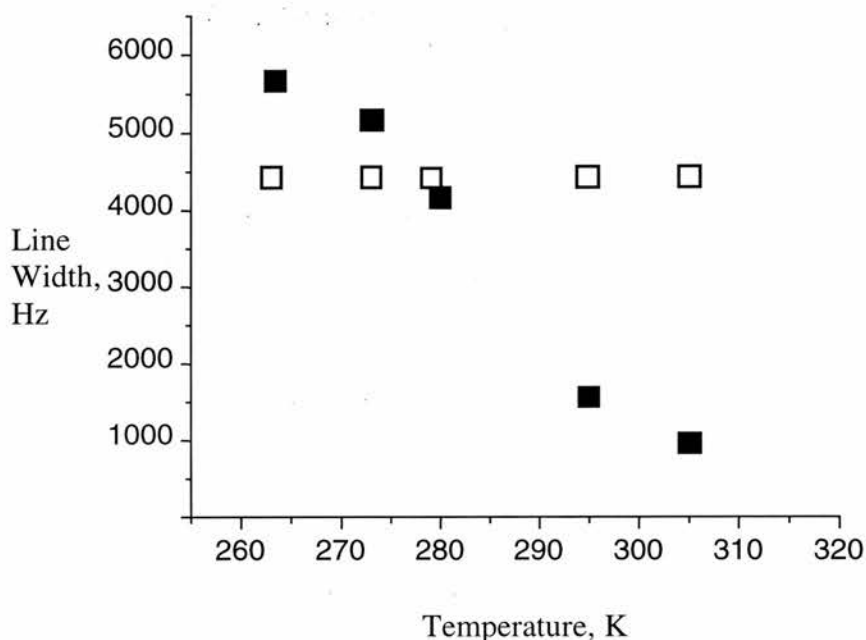


Fig.7.2. Linewidth variations for the crystalline complex $\text{PEG}_6\text{:LiPF}_6$ as a function of temperature: ^{31}P (open squares) and ^7Li (solid squares)

7.2. Ion transport in the crystalline complexes of composition 6:1

Ion conduction takes place in a variety of solids such as crystals, glasses and polymers. The crystalline solid electrolytes exhibit high conductivity in one of their sublattices at temperatures below their melting point and often as low as room temperature. The high ionic conductivity in these materials is essentially due to the high concentration of mobile ions and the low activation energy for ionic motion from site to site [1, 2].

Not all crystalline solids exhibit significant ionic conductivity. Only crystalline solids for which the crystal structure defines suitable pathways for ion migration between sites and there is partial occupancy of sites, can exhibit high levels of conductivity. Normally the structure is a 1-, 2- or 3-dimensional network of channels or planes (pathways) through which

the mobile ions can move. The crystalline electrolytes are usually single-ion conductors. Crystalline electrolytes, for example crystalline materials such as $\text{Na}\beta\text{Al}_2\text{O}_3$, RbAg_4I_5 , or $\text{Li}_{0.5}\text{La}_{0.5}\text{TiO}_3$ exhibit among the highest levels of ionic conductivity known in the solid state, exceeding by 1 to 3 orders of magnitude the maximum conductivity of conventional amorphous polymer electrolytes. RbAg_4I_5 possess a conductivity at room temperature that exceeds 10^{-1}Scm^{-1} and $\text{Li}_{0.5}\text{La}_{0.5}\text{TiO}_3$ achieve 10^{-3}Scm^{-1} at the same temperature [1-3].

According to the discussion so far, it is not so surprising that ion conduction may occur in certain crystalline polymer electrolytes. Not all of these materials can be expected to show significant ionic conductivity but only those for which the structure promotes ion transport. In contrast, all amorphous polymer electrolytes above T_g are ionic conductors since ion transport in this case is related to the segmental motion of the host polymer above T_g . Most previous studies [4-6] compared ion transport in the amorphous phase with that of crystalline 3:1 complexes. These crystalline complexes were found to be insulating and the results were extrapolated to conclude that, as a rule, the amorphous polymer electrolytes above T_g would always be more conducting than the crystalline materials.

The exact mechanism of ion conduction in the crystalline polymer electrolytes is not known although it must include ion hopping from site to site. The 6:1 materials are stoichiometric and this means that there is only a limited number of Li ion vacancies. Conduction must rely on either thermally created defects or imperfections in the structure. Ion transport may occur by a cooperative mechanism along the tunnels. Although defects can be an advantage in terms of generating ion hops, they can also inhibit ion transport if they result in blocking the channels, particularly in the case of one-dimensional ion transport.

7.3. Further work and optimising the ionic conductivity

The level of ionic conductivity in the crystalline 6:1 complexes is significantly higher than in the amorphous phase but it is not high in general terms. Therefore it is important to optimise the ionic conductivity in order to obtain technologically important materials. It is clear that ion transport in one-dimensional systems can be severely restricted by impurities and structural imperfections. However, crystalline polymer electrolytes that support ionic conduction in two or three dimensions may exhibit higher conductivity than the 6:1 complexes. Also, ion transport is more favoured when there is partial occupancy of the sites by the mobile ions. The introduction of vacancies or interstitials into the 6:1 complexes would result in significant increase in conductivity.

The results obtained in the present work define a different direction in the search for ionically conducting polymers. It is demonstrated that, in contrast to the prevailing view, ordered crystalline polymer electrolytes with suitable structures may promote high level of ionic conduction. Further advantage is the selectivity for Li ion transport in crystalline polymer electrolytes.

7.4. References

1. P.G.Bruce, *Solid State Electrochemistry*, Cambridge University Press, 1995
2. A.R.West, *Solid State Chemistry and its Applications*, J.Wiley&Sons, 1984
3. Y.Inaguma, L.Q.Chen, M.Itoh, T.Nakamura, T.Uchida, H.Ikuta and M.Wakihara, *Solid St.Comm.*, **86**, 689 (1993)
4. F.M.Gray, *Polymer Electrolytes*, RSC materials monographs, The Royal Society of Chemistry, Cambridge, 1997

5. C.Berthier, W.Gorecki, M.Minier, M.Armand, J.M.Chabagno and P.Rigaud, *Solid State Ionics*, **11**, 91 (1983)
6. W.Gorecki, M.Jeannin, E.Belorizky, C.Roux and M.Armand, *J.Phys.Condens.Matter*, **7**, 6833 (1995)

APPENDIX I

Refined structural data for $\text{PEO}_6\text{:LiPF}_6$ and $\text{PEO}_6\text{:LiSbF}_6$

Atom	x			y			z			U		
	$\text{PEO}_6\text{:LiPF}_6$	$\text{PEO}_6\text{:LiSbF}_6$	$\text{PEO}_6\text{:LiPF}_6$	$\text{PEO}_6\text{:LiSbF}_6$	$\text{PEO}_6\text{:LiPF}_6$	$\text{PEO}_6\text{:LiSbF}_6$	$\text{PEO}_6\text{:LiPF}_6$	$\text{PEO}_6\text{:LiSbF}_6$	$\text{PEO}_6\text{:LiPF}_6$	$\text{PEO}_6\text{:LiSbF}_6$	$\text{PEO}_6\text{:LiPF}_6$	$\text{PEO}_6\text{:LiSbF}_6$
Li	0.815(6)	0.791(12)	-0.018(4)	0.008(5)	-0.001(7)	-0.012(13)	0.04(1)	0.02(1)				
Hexafluorophosphate												
P (Sb)	0.674(4)	0.626(11)	0.284(3)	0.249(5)	0.491(5)	0.512(12)	0.015(3)	0.015(2)				
F1	0.629(9)	0.478(12)	0.294(5)	0.257(9)	0.633(8)	0.524(19)	0.015(3)	0.015(2)				
F2	0.779(6)	0.573(16)	0.336(4)	0.286(7)	0.59(1)	0.320(12)	0.015(3)	0.015(2)				
F3	0.739(8)	0.647(16)	0.206(3)	0.346(5)	0.54(1)	0.572(15)	0.015(3)	0.015(2)				
F4	0.610(6)	0.589(13)	0.354(4)	0.155(5)	0.393(9)	0.432(16)	0.015(3)	0.015(2)				
F5	0.558(6)	0.687(16)	0.235(5)	0.219(7)	0.44(1)	0.707(13)	0.015(3)	0.015(2)				
F6	0.734(7)	0.770(12)	0.279(5)	0.245(9)	0.362(8)	0.486(19)	0.015(3)	0.015(2)				

Chain

C1	1.384(6)	1.302(8)	0.019(4)	0.051(5)	0.699(9)	0.743(11)	0.006(5)	0.004(5)
C2	1.277(6)	1.177(7)	-0.037(4)	0.018(5)	0.687(9)	0.676(10)	0.006(5)	0.004(5)
O1	1.207(9)	1.161(10)	-0.018(4)	-0.039(5)	0.784(9)	0.776(11)	0.006(5)	0.004(5)
C3	1.141(6)	1.236(8)	-0.084(4)	-0.102(5)	0.801(7)	0.784(9)	0.006(5)	0.004(5)
C4	1.203(6)	1.189(8)	-0.112(5)	-0.159(5)	0.968(7)	0.878(10)	0.006(5)	0.004(5)
O2	1.112(6)	1.128(10)	-0.093(4)	-0.117(6)	1.035(7)	0.960(12)	0.006(5)	0.004(5)
C5	1.127(7)	1.112(8)	-0.102(5)	-0.138(5)	1.196(7)	1.100(10)	0.006(5)	0.004(5)
C6	1.049(6)	1.023(7)	-0.057(4)	-0.101(5)	1.277(9)	1.168(9)	0.006(5)	0.004(5)
O3	0.938(6)	0.912(8)	-0.087(4)	-0.087(5)	1.179(9)	1.059(12)	0.006(5)	0.004(5)
C7	0.919(6)	0.881(8)	-0.154(4)	-0.148(6)	1.085(9)	0.955(11)	0.006(5)	0.004(5)
C8	0.781(6)	0.749(8)	-0.170(5)	-0.159(4)	1.025(8)	0.868(13)	0.006(5)	0.004(5)
O4	0.750(7)	0.726(10)	-0.126(4)	-0.082(4)	0.887(9)	0.830(13)	0.006(5)	0.004(5)
C9	0.623(7)	0.631(9)	-0.129(4)	-0.077(5)	0.815(9)	0.695(10)	0.006(5)	0.004(5)
C10	0.640(7)	0.626(10)	-0.053(4)	0.009(5)	0.736(8)	0.676(10)	0.006(5)	0.004(5)

O5	0.650(7)	0.639(8)	0.015(4)	0.051(7)	0.829(7)	0.810(10)	0.006(5)	0.004(5)
C11	0.577(7)	0.554(8)	0.080(4)	0.104(6)	0.766(8)	0.821(15)	0.006(5)	0.004(5)
C12	0.500(6)	0.458(7)	0.122(5)	0.136(5)	0.86(1)	0.883(12)	0.006(5)	0.004(5)
O6	0.389(7)	0.371(10)	0.082(5)	0.082(7)	0.80(1)	0.883(10)	0.006(5)	0.004(5)
D1	1.402(8)	1.366(11)	0.048(5)	0.010(7)	0.606(8)	0.732(15)	0.006(5)	0.004(5)
D2	1.463(7)	1.295(11)	-0.025(5)	0.110(6)	0.71(1)	0.712(15)	0.006(5)	0.004(5)
D3	1.209(7)	1.093(10)	-0.019(5)	0.039(7)	0.574(9)	0.667(17)	0.006(5)	0.004(5)
D4	1.312(8)	1.171(13)	-0.106(4)	-0.006(9)	0.69(1)	0.565(11)	0.006(5)	0.004(5)
D5	1.14(1)	1.222(13)	-0.126(4)	-0.104(8)	0.73(1)	0.677(9)	0.006(5)	0.004(5)
D6	1.071(7)	1.319(9)	-0.067(6)	-0.089(8)	0.75(1)	0.866(15)	0.006(5)	0.004(5)
D7	1.267(7)	1.139(10)	-0.152(5)	-0.197(6)	1.037(9)	0.806(14)	0.006(5)	0.004(5)
D8	1.287(6)	1.266(10)	-0.104(5)	-0.174(8)	0.96(1)	0.967(13)	0.006(5)	0.004(5)
D9	1.094(9)	1.095(13)	-0.156(5)	-0.196(5)	1.19(1)	1.076(17)	0.006(5)	0.004(5)
D10	1.223(7)	1.196(9)	-0.081(5)	-0.114(9)	1.27(1)	1.171(13)	0.006(5)	0.004(5)
D11	1.066(8)	0.994(11)	0.008(4)	-0.139(7)	1.30(1)	1.233(13)	0.006(5)	0.004(5)

D12	1.132(8)	1.048(12)	-0.067(6)	-0.054(6)	1.374(9)	1.244(15)	0.006(5)	0.004(5)
D13	0.967(9)	0.933(15)	-0.156(5)	-0.129(9)	0.96(1)	0.884(15)	0.006(5)	0.004(5)
D14	0.943(8)	0.899(14)	-0.209(5)	-0.196(6)	1.14(1)	1.021(17)	0.006(5)	0.004(5)
D15	0.758(9)	0.738(14)	-0.222(5)	-0.185(7)	0.94(1)	0.763(16)	0.006(5)	0.004(5)
D16	0.722(8)	0.671(15)	-0.158(6)	-0.168(8)	1.097(9)	0.910(17)	0.006(5)	0.004(5)
D17	0.579(8)	0.641(15)	-0.135(7)	-0.127(7)	0.906(9)	0.652(15)	0.006(5)	0.004(5)
D18	0.593(8)	0.564(11)	-0.182(5)	-0.064(10)	0.76(1)	0.734(18)	0.006(5)	0.004(5)
D19	0.721(8)	0.703(12)	-0.061(6)	-0.002(10)	0.68(1)	0.652(18)	0.006(5)	0.004(5)
D20	0.531(7)	0.543(11)	-0.054(6)	-0.017(10)	0.69(1)	0.637(17)	0.006(5)	0.004(5)
D21	0.569(8)	0.481(9)	0.134(4)	0.077(9)	0.77(1)	0.781(19)	0.006(5)	0.004(5)
D22	0.556(8)	0.599(14)	0.066(6)	0.147(7)	0.620(8)	0.887(20)	0.006(5)	0.004(5)
D23	0.527(8)	0.502(13)	0.162(5)	0.162(9)	0.989(9)	0.981(13)	0.006(5)	0.004(5)
D24	0.428(8)	0.394(11)	0.165(5)	0.177(7)	0.83(1)	0.830(17)	0.006(5)	0.004(5)

Atomic displacement factors for the complexes $\text{PEO}_6\cdot\text{LiXF}_6$ ($X = \text{P, As, Sb}$)

	$\text{PEO}_6\cdot\text{LiPF}_6$	$\text{PEO}_6\cdot\text{LiAsF}_6$	$\text{PEO}_6\cdot\text{LiSbF}_6$
Li	0.04(1)	0.019(9)	0.02(1)
X (P, As, Sb)	0.015(3)	0.02(3)	0.015(2)
F	0.015(3)	0.02(1)	0.015(2)
C	0.006(5)	0.40(3)	0.004(5)
O	0.006(5)	0.11(8)	0.004(5)
H	0.006(5)	0.076(8)	0.004(5)

APPENDIX II

Selected bond distances (Å), angles (°) and torsion angles (°) in PEO₆:LiPF₆ and PEO₆:LiSbF₆

	PEO ₆ :LiPF ₆	PEO ₆ :LiSbF ₆		PEO ₆ :LiPF ₆	PEO ₆ :LiSbF ₆
Li-O1	2.17(3)	2.16(4)	C1-C2-O1	115(6)	108(6)
Li-O4	2.17(3)	2.14(4)	O1-C3-C4	105(6)	102(5)
Li-O2	2.17(3)	2.16(4)	C3-C4-O2	99(6)	107(6)
Li-O5	2.17(3)	2.19(4)	O2-C5-C6	122(6)	125(6)
Li-O3	2.18(3)	2.19(4)	C5-C6-O3	94(6)	113(7)
			O3-C7-C8	108(5)	117(7)
P(Sb)-F1	1.55(2)	1.82(1)	C7-C8-O4	100(5)	96(5)
P(Sb)-F2	1.55(2)	1.83(1)	O4-C9-C10	85(5)	98(5)
P(Sb)-F3	1.56(2)	1.83(1)	C9-C10-O5	115(5)	115(7)
P(Sb)-F4	1.56(2)	1.82(1)	O5-C11-C12	122(6)	155(11)
P(Sb)-F5	1.55(2)	1.81(1)	C11-C12-O6	102(6)	113(7)
P(Sb)-F6	1.55(2)	1.82(1)	O6-C1-C2	113(5)	137(7)
C1-C2	1.56(2)	1.55(1)	C2-O1-C3	109(5)	113(7)
C3-C4	1.55(2)	1.55(1)	C4-O2-C5	123(5)	126(7)
C5-C6	1.55(2)	1.55(1)	C6-O3-C7	128(6)	110(6)
C7-C8	1.56(2)	1.55(1)	C8-O4-C9	110(5)	109(6)
C9-C10	1.56(2)	1.54(1)	C10-O5-C11	119(5)	122(7)
C11-C12	1.56(2)	1.54(1)	C12-O6-C1	117(6)	119(7)
C2-O1	1.43(2)	1.42(1)	O6-C1-C2-O1	2.82	<i>c</i> -52.40 \bar{g}
O1-C3	1.42(2)	1.42(1)	C1-C2-O1-C3	161.01	<i>t</i> -65.63 \bar{g}
C4-O2	1.43(2)	1.42(1)	C2-O1-C3-C4	-107.32	\bar{g} -171.90 <i>t</i>
O2-C5	1.43(2)	1.42(1)	O1-C3-C4-O2	-109.87	\bar{g} -21.56 <i>c</i>
C6-O3	1.43(2)	1.42(1)	C3-C4-O2-C5	175.27	<i>t</i> -152.82 <i>t</i>
O3-C7	1.43(2)	1.43(1)	C4-O2-C5-C6	-158.74	<i>t</i> -165.46 <i>t</i>
C8-O4	1.43(2)	1.42(1)	O2-C5-C6-O3	-58.49	\bar{g} 28.97 <i>c</i>
O4-C9	1.43(2)	1.42(1)	C5-C6-O3-C7	19.31	<i>c</i> 39.32 <i>c</i>
C10-O5	1.43(2)	1.42(1)	C6-O3-C7-C8	169.64	<i>t</i> 157.55 <i>t</i>
O5-C11	1.43(2)	1.42(1)	O3-C7-C8-O4	89.51	<i>g</i> 45.39 <i>g</i>
C12-O6	1.43(2)	1.42(1)	C7-C8-O4-C9	-176.87	<i>t</i> 152.68 <i>t</i>

O6-C1	1.42(2)	1.42(1)	C8-O4-C9-C10	157.02	t	-178.41	t
			O4-C9-C10-O5	-80.30	\bar{g}	-42.77	c
			C9-C10-O5-C11	-130.20	\bar{g}	-124.04	\bar{g}
			C10-O5-C11-C12	129.98	g	114.71	g
			O5-C11-C12-O6	-91.21	\bar{g}	-49.33	\bar{g}
			C11-C12-O6-C1	3.22	c	-62.08	\bar{g}
			C12-O6-C1-C2	145.58	t	-151.27	t

APPENDIX III

Summary of ^7Li NMR data on the high molecular weight complexes $\text{PEO}_6:\text{LiXF}_6$ (X = As, Sb), MW = 100,000

Linewidth values for the complex $\text{PEO}_6:\text{LiAsF}_6$

T, °C	T, K	Static linewidth, Hz	MAS linewidth without proton decoupling, Hz	MAS linewidth with proton decoupling, Hz
22	295	5100	500	250
62	335	3500	400	250
84	357	1750	350	250
97	370	1400	300	250
110	383	1300	250	250
129	402	1100		
141	414	700		

Linewidth values for the complex $\text{PEO}_6:\text{LiSbF}_6$

T, °C	T, K	Static linewidth, Hz
22	295	5000
40	313	4800
58	331	4000
76	349	3200
98	371	1700

Comments:

Composite lines were observed at all temperatures. The lines could not be described by a single Gaussian, or deconvoluted unambiguously into two Gaussians. Composite lines were observed in both static and MAS experiments.

The dipolar Li – H interactions had significant contribution (~50%) to the ^7Li line at low temperatures. At higher temperatures the influence of the Li – H dipolar interactions was less pronounced. The data are consistent with averaging of the Li – H dipolar interactions at elevated temperatures which is related to increased mobility of the Li sites.

Due to the multi-component character of the ^7Li lines, the mechanisms responsible for the observed line narrowing cannot be reliably determined.

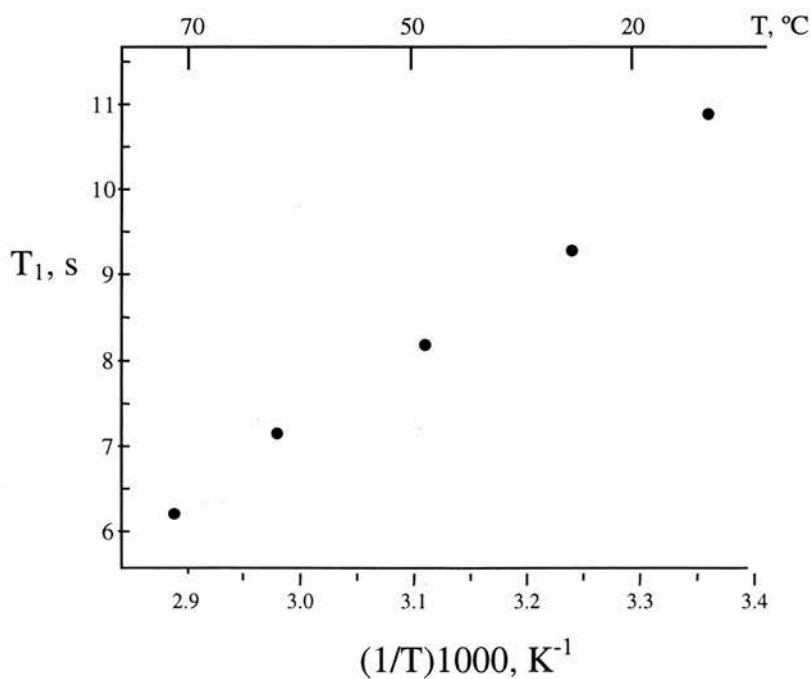
The spin-lattice relaxation could not be described by a single exponential. Attempts to fit the relaxation to a double exponential failed because of significant errors in the fitting results. The results suggest that there is a distribution of relaxation times similarly to the observations reported for other disordered solids or glasses (Ref.28 in Chapter 6).

APPENDIX IV

Summary of ^7Li NMR data on the crystalline complex $\text{PEG}_6\text{:LiSbF}_6$, MW = 2,000

^7Li linewidth values for the complex $\text{PEG}_6\text{:LiSbF}_6$

T, °C	T, K	Static linewidth, Hz	Static linewidth with proton decoupling, Hz
22	295	5200	2100
36	309	5100	2050
49	322	5000	2000
63	336	4800	2000
73	346	4400	1950
80	353	4100	1950



Variation of the spin-lattice relaxation time T_1 for the complex $\text{PEG}_6\text{:LiSbF}_6$

Comments:

In most cases, the lines could be fitted to a single Gaussian. The line narrowing suggests that there is a slight increase in the Li ion mobility as the temperature increases.

Spin-lattice relaxation could be described by a single exponential in most cases.

As a whole, the results are similar to the experimental results for the complexes of $MW = 1,000$. However, the existence of a second Li site is not so obvious in the case of the complex of $MW = 2,000$. This is in support of the view that the second Li site in the low-molecular weight complexes ($MW = 1,000$) is related to the "defect" Li sites coordinated to the polymer chain ends. The fraction of these "defect" Li sites is much smaller in the case of the complexes of $MW = 2,000$ and they may become unobservable since the NMR signal is dominated by the much bigger fraction of regular Li sites.